APPLICATION OF IONIC LIQUIDS ON MICROSCOPIC OBSERVATION OF HYDRATED MATERIALS

イオン液体を用いた含水試料の
電子顕微鏡観察手法の開発とその応用

DOCTOR OF PHILOSOPHY DISSERTATION

MARCH, 2013

CHISATO TAKAHASHI

NAGOYA INSTITUTE OF TECHNOLOGY
JAPAN

APPLICATION OF IONIC LIQUIDS ON MICROSCOPIC OBSERVATION OF HYDRATED MATERIALS

DOCTOR OF PHILOSOPHY DISSERTATION

MARCH, 2013

CHISATO TAKAHASHI

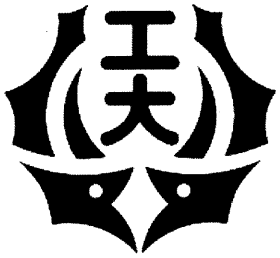

NAGOYA INSTITUTE OF TECHNOLOGY

JAPAN

CONTENTS

LIST OF FIGURES

CHAPTER 1

CHAPTER 2

CHAPTER 7

LIST OF TABLES

CHAPTER 2

CHAPTER 3

CHAPTER 1

INTRODUCTION

In materials research, many remarkable achievements have been reported for several decades. The characterization of structures and their physical properties on a micron or nano-order scale is important in order to understand the behavior of materials for various functional applications. In order to understand the behavior of a material, various scientific instruments such as an optical microscope, electron microscope, X-ray diffractometer, etc., have been developed. Among these characterization instruments, electron microscopes, which can characterize the surface as well as the bulk of a material on an atomic level, are widely used in advanced material research.

The electron microscope is not only used for observation, but also used as a reaction field which can be applied to catalytic reactions, field emission properties, solid-liquid reactions, etc. However, techniques for the characterization of hydrous materials (such as biological materials and water absorbed materials), which contain a liquid phase, using an electron microscope are still in the developmental stage because most of the electron microscopes require vacuum conditions. In general, it is well known that wet-type samples are not suitable for observation using an electron microscope. Also, it is essential to maintain the structure or morphology of the wet samples during the observations. However, it requires an investment of time and technique to prepare the sample for an electron microscope by a conventional method. In recent years, a low vacuum electron microscope

and environmental electron microscope are being used to observe the morphology of wet materials. Though these techniques are applied to biomaterials and agro materials research, there are some limitations, such as cost of the apparatus and sample preparation. Therefore, it requires an investment of time and technique to prepare the sample by the conventional method to observe it under an electron microscope.

Recently, ionic liquids (ILs), which are organic fused salts, have attracted significant attention as environment-friendly solvents and have unique properties such as electrical conductivities, negligible vapor pressure, non-flammable and high polarity. Thus, ILs can be used as an electrolyte, solvent or catalyst. They can exist without evaporation under vacuum conditions in the electron microscope due to these advantageous properties. Therefore, the IL can be considered as a sample preparation medium for hydrous materials. This is expected to save the time of sample preparation as well as helps to observe hydrous materials without any difficult technique. However, the detailed observation mechanism of hydrous materials using an IL has never been understood. Although many researchers focused on the molecular dynamics of ILs including the interaction of an IL and water molecules, it remains inconclusive. In addition, the fabrication of composite materials with the aid of various ILs has been paid attention with the aim of enhancing the conductivity of materials in various fields.

It can be considered that the characterization of hydrous materials with the aid of an IL by electron microscopy will make a significant contribution to further research in the field of science and technology. Moreover, studying the molecular dynamics of ILs and observation mechanism using an IL is very useful for understanding the physical and

chemical physics of a material. Composite materials with an IL have attractive potentials to develop a new commercial field. Thus, the fabrication of composite materials with the aid of various ILs has been focused on with the aim of enhancing the conductivity of materials in various fields.

1.1 History of electron microscope

Observation is essential action in scientific research that leads to new discoveries and new life. This strong motivation makes it important to observe materials on micron and nano-orders which is generally invisible to the human eye. Atoms can also be observed using an electron microscope. The electron microscope is an observation instrument using an electron beam which has a very short wavelength. Due to its electron beam, the fine structure of materials, which cannot be confirmed by an optical microscope, can be observed.

In 1934, Ruska in Germany has developed the transmission electron microscope (TEM) [1-5]. During the early stage of development of the electron microscope, many countries had attracted attention as the "electron microscope Japan" due to its high technology.

Moreover, in-situ observations and a high voltage TEM have been developed for increasing the range of functions (Figure 1. 1) [6,7]. At the end of the 20^{th} century, the technology of aberration correction was developed by a German, and resolution was drastically increased [8,9]. The development of aberration correction enabled the design of a specific holder for in-situ observations. The controlled environment atmosphere electron

microscope was designed for catalysis study under a gas atmosphere. Meanwhile, low voltage TEMs are used for the observation of various soft materials and biomaterials [10].

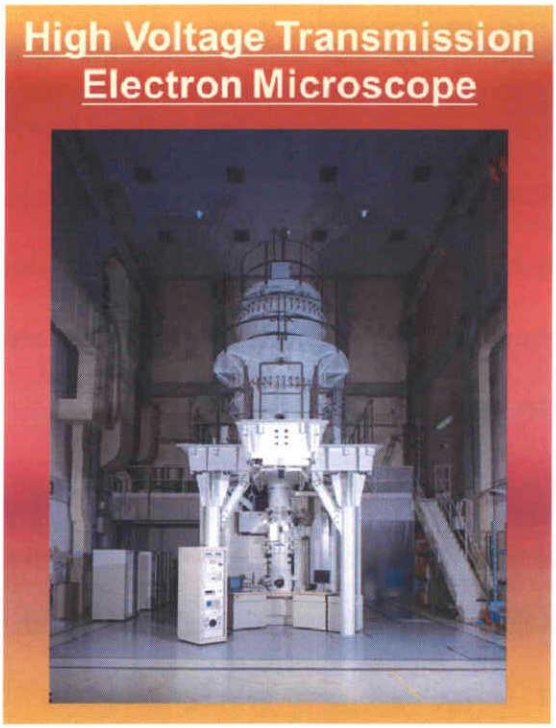

Figure. 1. 1. High voltage transmission electron microscopy (copyrighted by JEOL Co).

In addition, scanning transmission electron microscopy (STEM), Lorentz electron microscopy, electron beam holography and three-dimensional tomography have been developed and used for research in various fields (Figure 1. 2). Recently, observation of an electric field at an atomic level was achieved using a newly designed TEM [11]. Not only the microscope, but also the analysis equipment have been developed along with the microscope. Energy dispersive X-ray spectrometry (EDX), X-ray emission spectrometry (XES) and electron energy-loss spectroscopy (EELS) are useful to analyze various

functional materials. Especially, peripheral equipment used with the microscope has been the focus after the development of the aberration correction.

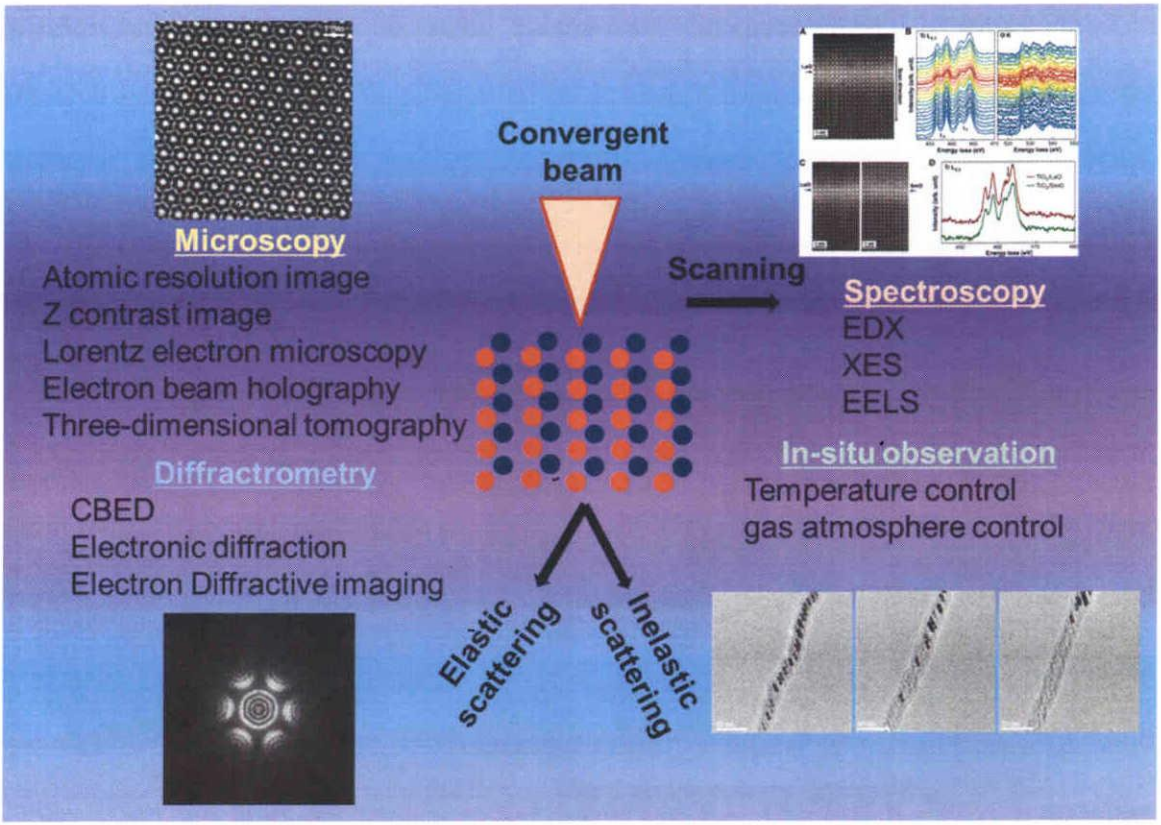

Figure. 1. 2. Diversification of electron microscope method.

On the other hand, the scanning electron microscope (SEM) was developed after the invention of the TEM by Ruska. In 1935, Knoll in Germany developed the original form of the SEM. In 1961, the SEM had undergone significant development by McMullan in England. It had an ET detector, observation method and application technique. Also, the field emission type SEM (FE-SEM) has been developed, and analytical functions such as electron backscatter diffraction (EBSD) and wavelength-dispersive X-ray spectrometer

(WDS) were established along with the FE-SEM [12,13]. In recent days, a low-vacuum SEM and environmental SEM (ESEM) have been developed. Normally, it is well known that samples containing a liquid, such as biological materials, cannot withstand vacuum conditions. These instruments now enable us to observe hydrated materials without changing their morphology.

Figure. 1. 3. Transmission electron microscope and field emission scanning electron microscope (copyrighted by JEOL Co).

It is considered that recent electron microscopes can realize comprehensive measurements, such as diffractometry, spectroscopy and microscopy, of the selected fine structure of a sample. These TEM and SEM observation techniques play an active role for not only advancements in research fields, such as physical chemistry, chemical physics, material science and life science field, but also in industrial fields such as catalysis,

batteries, cosmetics, semiconductor devices, molecular materials, bio-science and medical care (Figure 1. 3).

However, the hydrated sample must be frozen in order to observe it in a low-vacuum SEM, and the ESEM is still not a conventional instrument commonly used in research laboratories. Therefore, we tried to develop a new observation methodology for hydrous materials using conventional electron microscopes such as SEM, FE-SEM, TEM, FE-TEM, etc.

1.2. History of ionic liquids and their application.

Ionic liquids (ILs) are organic fused salts that consist of ions and remain fluid at room temperature (RT). Some ILs exist below 100 °C [14]. These compounds consist of an organic cation and an organic or inorganic anion. The cation, which is a large and asymmetric structure, prevents the formation of a crystal structure, such as NaCl, and hence remains as a liquid at RT. The interaction between the anion and cation of ILs and Coulomb forces affect the physico-chemical properties of the ILs. The first IL, ethyl ammonium nitrate $[EtNH_3][NO_3]$, which has a melting point of 12 °C was reported by Paul Walden in 1914 [15]. Moreover, 1-ethyl-3-methylimidazolium tetrafluoroborate, $[emim][BF_4]$, which was reported in 1992, has brought much attention to IL research in the scientific community [16].

Since then, the research involving ILs have attracted significant attention as an environment-friendly solvent, catalysis and lubricant [17-21], and a large number of references are already available in this field. ILs have unique physical properties, such as

negligible-vapor pressure (less than 5×10^{-9} Torr), non-flammable, chemical/ thermal stability, high ionic conductivity (less than 120 mS cm^{-1}) and wide electrochemical windows (less than 5.8 V). Most of the ILs are classified in seven families based on the structures of their cation and anion parts (Figure 1. 4). The different combinations of cations and anions significantly affect the IL properties, such as polarity, melting point, hydrophilicity, hydrophobicity, etc.

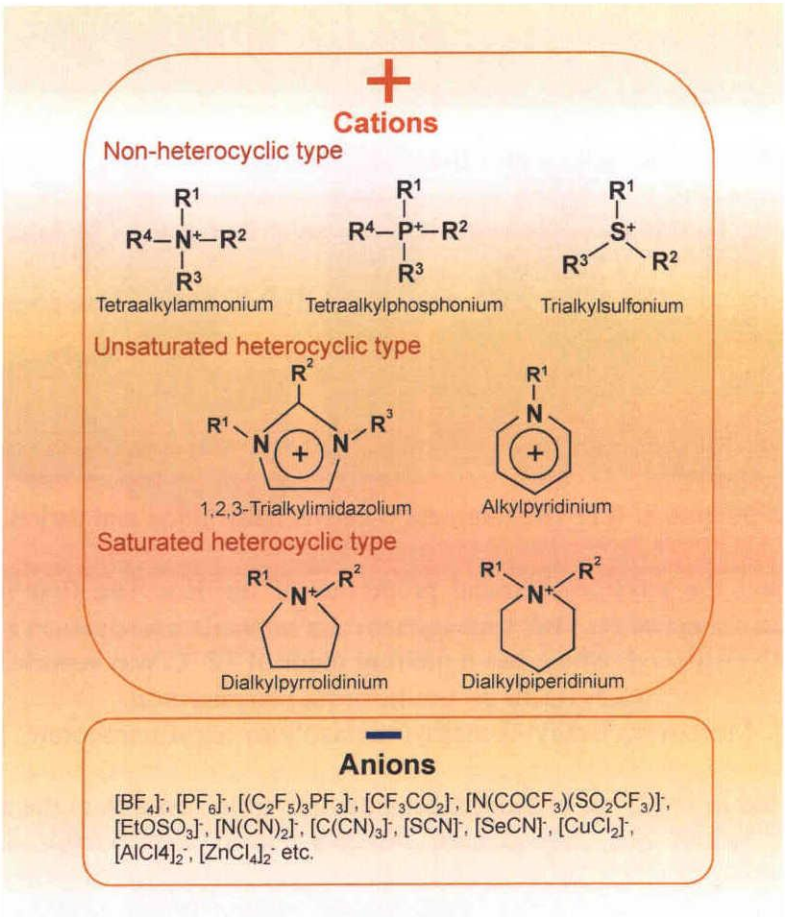

Figure. 1. 4. Types of cations and anions that constitute the ILs.

Due to their several unique properties, ILs are used as solvents, electrolytes and functional materials in various research fields. Typical applications of ILs are described in Figure 1. 5. Although some applications using ILs have been successful, however, many applications are still being studied.

ILs have been used as green solvents in various fields. Using ILs, organic and inorganic synthesizes can be successfully carried out and then the reaction and behavior observed [22,23]. Enzymatic reactions in ILs have been paid significant attention due to the invert reaction mechanism [24,25]. The dispersion and dissolution of various compounds, such as cellulose and starch, etc., have also been examined by some researchers [26,27].

As electrolytes, ILs are safety used for safety in lithium batteries and fuel cells due to their nonflammable property [28,29]. Although the charge transfer resistance that cause the power to decline has been pointed out, a high capacity electrode enables to fabricate a cell with a good performance. Using ceramic materials, solid electrolytes and electrodes are being fabricated with the aid of ILs [30-32].

ILs have significant applications as functional materials. By the combination of specific anions and cations, ILs with specific properties can be fabricated. These ILs can provide the required functions for targeting some materials fabricated as composites. There are many ILs which have certain properties such as magnetic properties [33], liquid crystalline properties [34]. Moreover, these are used as lubricants for base oils which can be applied for a variety of contacts and space technology. The ILs are used in biomaterials and agro materials due to their improved properties such as compatibility, thermal stability, etc

[35,36]. Furthermore, a composite gel mixed with an IL is used in drug delivery systems and the fabrication of contact lenses [37,38].

Based on these applications, it is considered that ILs can significantly contribute to creating and advancing the science and technologies in various research fields.

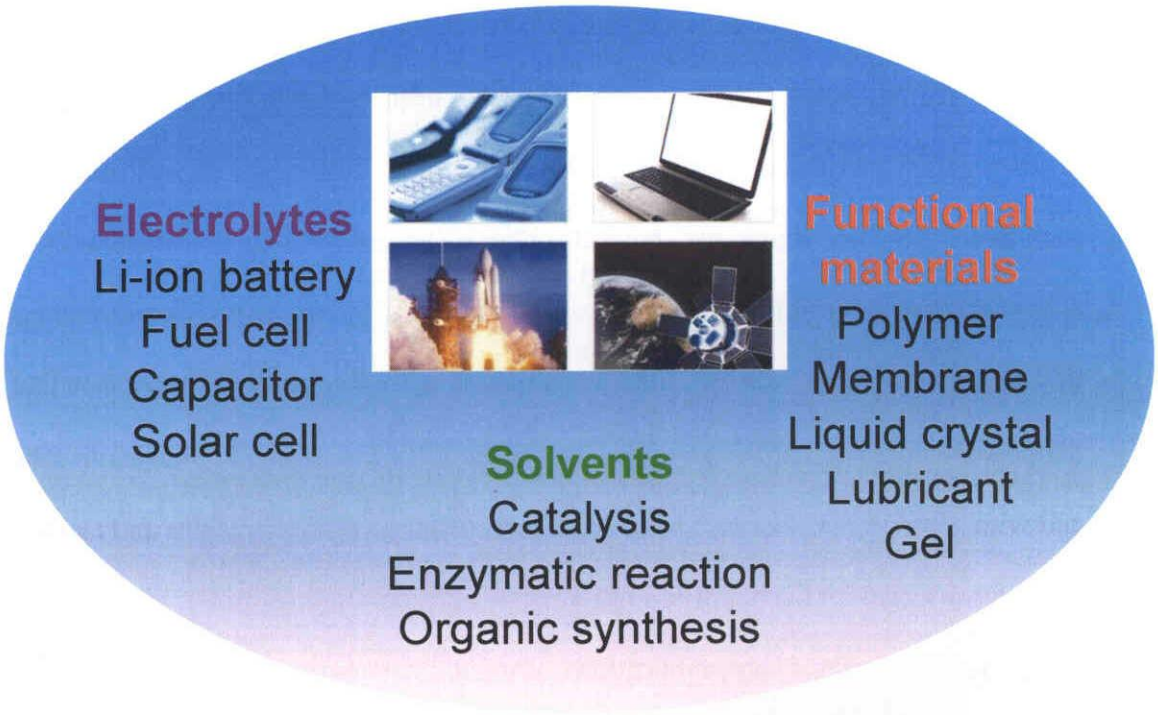

Figure. 1. 5. Typical applications of ILs.

1.3. Application of ionic liquids for electron microscope observations.

The unique properties of RTILs, such as conductivity and negligible vapor pressure, have opened up new scientific methodologies under vacuum conditions. In 2005, Scherson et al. reported that RTILs can be used under a high vacuum condition (less than 5×10^{-9} Torr) [39]. Subsequently, RTILs were the focus as solvents for vacuum technology. This

discovery is a breakthrough method in this scientific field, which defies the common wisdom that liquid evaporates under vacuum conditions.

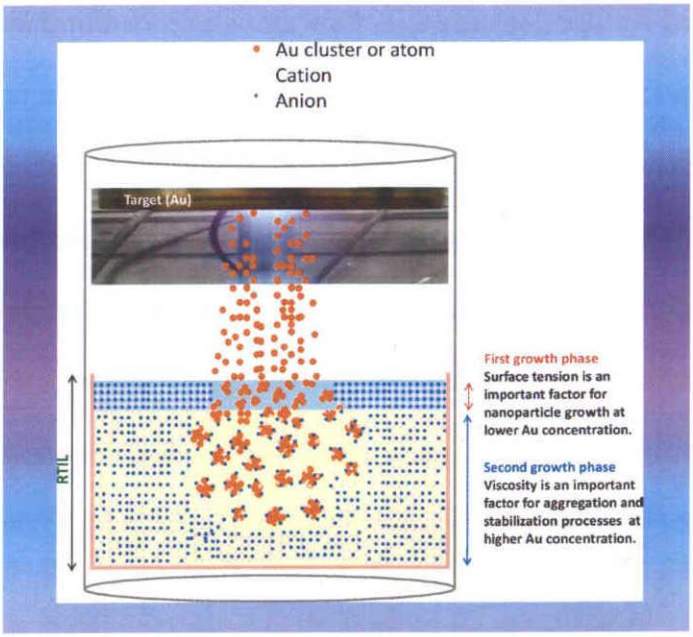

Figure. 1. 6. Schematic illustration of the Au nanoparticle formation mechanism during Au sputtering onto RTIL (Kuwabata et.al, *J. Phys. Chem. Lett.* 1 (2010) 3177-3188).

Generally, a wet sample including a liquid phase cannot be inserted in an instrument under vacuum conditions. However, many researchers need to characterize a wet sample using a vacuum apparatus. RTILs allow the sample to keep its liquid state without any treatment even under vacuum conditions.

Recently, magnetron sputtering onto the RTILs, a breakthrough method, improved the dispersion of metal nano-particles without any treatment and byproducts [40,41] (Figure 1. 6). This method has succeeded in the fabrication of various pure metal nanoparticle sizes

of less than 10 nm, such as Au, Ag and Pt. Furthermore, alloy nanoparticles were successfully fabricated using this method.

Due to the development a new spectro-electrochemical method, the Cu electrode reaction in an RTIL was observed under high vacuum conditions (less than 5×10^{-9} Torr). The metal nanoparticles were fabricated using RTILs by various reactions.

X-ray photospectroscopy (XPS) is useful for the characterization of the composition and chemical state of a material. Using ILs, the in-situ characterization of chemical reactions in RTILs could be carried out.

Interestingly, samples containing ILs can be observed using an electron microscope (SEM / TEM) under high vacuum conditions. Generally, the samples for electron microscopy need a coating of osmium, platinum or carbon. However, ILs provide conductive and negligible vapor pressure properties to samples though they are liquids. It is reported that electrons, which are injected into the ILs, are stable and move into the liquid phase of the ILs under a high accelerating voltage condition [42]. Based on this discovery, Kuwabata et al. developed the observation method of insulating samples using ILs [43-47]. The insulating star-like sand was observed using a hydrophobic IL, [EMI][TFSI], and abrasive paper was also observed using a hydrophobic IL, [BMI][TFSI] (Figure 1. 7). The TiO_2 nano-tube layers in a wet condition using droplets of ILs were characterized in order to study the wetting behavior [48]. Surprisingly, the possibility of microscopic observations of materials containing water was also suggested and many researchers reported the fine morphology and observation method of various insulating samples using ILs. The cellular ultrastructure of a cultured human cell was characterized using hydrophilic and

hydrophobic ILs [49-51]. It was revealed that hydrophilic ILs are useful for observing the morphology of wet materials compared to hydrophobic ILs. By using hydrophilic ILs, the fine structure of a chromosome was observed [52]. ILs were prepared such as pre-warmed, well-mixed, low concentration, mixed with platinum blue staining, etc., due to searching for the optimized conditions. It is considered that the ultrastructure of the basidiospore ornamentation is important in the delimitation of taxa for fungi. Hydrophilic ILs enabled the determination of the ultrastructure of the basidiospore ornamentation [53]. Moreover, using Choline-like ILs, which have a high penetration ability, the morphology of seaweed and food samples could be observed [54].

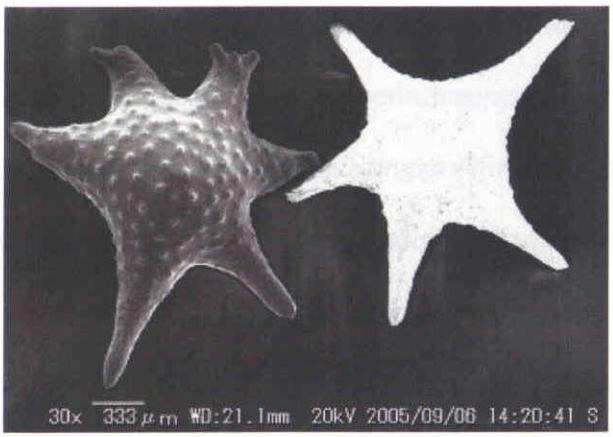

Figure. 1. 7. Observation of star-like sand using ILs (Kuwabata et.al, *Chem. Lett.* 35 (2006) 600-601).

However, in this process, one must take note of the hygroscopic properties of the hydrophilic IL wherein the absorption of some amount of water from the atmosphere occurs. Depending on the amount of absorbed water, the IL properties, such as viscosity, conductivity and polarity, can be drastically changed. Therefore, we need to consider the

existence of water during electron microscopic observations of water-containing materials using hydrophilic ILs.

1.4. Interaction between water and ionic liquids.

RTILs have been attracting significant attention in various fields as a solvent for chemical reactions and separations, and as electrolytes for fuel cells and capacitors as described in section 1.2. However, some researchers have started to point out the lack of understanding of the IL structure that affects its physical properties when using the ILs. Therefore, the possible presence of water in the RTILs that affects their solvent properties, such as electron conductivity, viscosity, polarity, etc., has been reported using a variety of experimental techniques and theoretical calculations [55,56]. ILs easily absorb water molecules due to their high hygroscopic property. In 2001, the stretching modes of water have been studied in order to understand the kind of hydrogen bonding between the water molecules in the liquid and solid phases [57]. Focused on the classification of hydrogen bonding, Welton et al. reported the interaction between the imidazolium cation-based ILs and water molecules using attenuated total reflectance (ATR) and transmission IR spectroscopies [58]. They assigned two kinds of hydrogen bondings, which were derived from the anion part of the IL and water molecules such as the symmetric and antisymmetric stretch normal-mode vibrations formed as A-...H-O-H...A- (where A- indicates the anion part of IL). Almost all ILs absorb water molecules from atmosphere by hydrogen bonding via both hydrogen atoms of water to two anions of the RTILs. In 2008, Jeon et al. reported the structural change in the hydrophilic IL [BMIM][BF_4] and water using ATR and Raman

microscopies [59]. They observed the spectra of a mixture of water and [BMIM][BF_4] and assigned the 10 CH peaks and 4 OH peaks in the range of 2800-3200 cm^{-1}. The water molecules in the mixture form global hydrogen bonding network around 35 mol % H_2O, and which cause a formation change in the cations and anions. This study has been accelerating the research of the molecular dynamics of a mixture of IL and water molecules.

For about 10 years, the theoretical calculations of the interaction between water molecules and ILs have been studied using molecular dynamics simulations of nano-structural organizations [60-65]. Using the molecular dynamics method, Moreno et al. reported that around 20 mol % water concentrations, the cation and anion parts of IL: [BMIM][BF_4] are selectively coordinated by individual water molecules, however, their ionic network is largely unperturbed [66]. At high water concentrations, the ionic network is somewhat disrupted or swollen in a nonspecific way by the water clusters. At around 20 mol % water concentrations, the transition of water monomers and dimers to larger aggregates increased.

The interaction between OH (derived from water) and IL (both cation and anion) under different conditions can be observed by FT-IR spectroscopy and Raman spectroscopy. Abe et al. investigated that a significant amount of a specific hydrogen bonding, such as BF_4-HOH-BF_4 in the mixture of IL: [DEME][BF_4] and water, can exist even at 77K [67,68]. It is considered that the collapse of the cation-anion electrostatic network was induced by the water. It is reported that the formation of a weak hydrogen bonding between water and IL: [BMIM][BF_4] was not completely dissociated even at 190℃, though the water molecules gradually dissociate during heating [69,70].

Focused on this specific interaction between the hydrophilic IL and water molecules, an optimization method of the microscopic observations of hydrous materials and the study of the observation mechanism using a hydrophilic IL have been proposed.

1.5. Thesis statement and thesis organization

The aim of this study is to establish the microscopic observation methodology of hydrated materials and their application. In order to cover the entire range of the inorganic and hydrous materials research fields, biological polymers, ceramics green bodies, clay with a layered structure and biological materials will be selected. Biological polymers, ceramics green bodies and biological materials were selected as the polymer materials, insulated inorganic materials and organic materials, respectively. In addition, clay was selected as a specific insulated inorganic material which has an intercalating ability.

The sample preparation method using hydrophilic IL has been developed during various material characterizations. It can be considered that the water concentration within the hydrous sample after the hydrophilic IL treatment is important for optimization of the observation method. The interaction of water molecules within hydrous sample and hydrophilic IL has occurred during the sample preparation. Therefore, we focused on the molecular dynamics and studied the observation mechanism of hydrous materials using hydrophilic IL. In addition, we studied the observation methodology for both biomaterials and various hydrous materials.

This thesis is expected to contribute a new methodology to the following areas:

1. Characterization of wet materials in the full range of inorganic and hydrous material research fields.

2. Study of observation mechanism of hydrous materials using IL and molecular dynamics of a mixture of IL and water molecules.

3. Fabrication of electrically conductive materials including transparent thin films, which presents a simple and direct process technique of introducing an electrically conductive IL phase into the interlayer of montmorillonite.

The thesis is organized as follows:

In Chapter 2, the morphology of an agar gel under different swelling conditions and water contents are observed by FE-SEM. The FE-SEM observation mechanism of the agar gel in the presence of IL is examined. The interaction mechanism is studied in terms of the hydrogen bond between the anionic part of the IL and water molecules (also water molecules within the agar gel) using Raman spectroscopy. Furthermore, agar gels treated with IL at different water concentrations were observed by FE-SEM. Also, the existence of the IL within the agar gel after displacement of the water inside the agar gel is examined using a differential scanning calorimeter (DSC). In addition, the shrinkage of the agar gel due to the IL and water interaction is measured. Based on the FE-SEM and DSC results, the interaction of water and hydrophilic IL and the observation mechanism of the agar gel treated with the IL are proposed.

In Chapter 3, we report the surface morphology of the porous hydroxyapatite (HAp) green body in a wet condition with the aid of the hydrophilic IL and compared the changes in the pore structure that occurred during the drying and after sintering.

In Chapter 4, we proposed a modified method to observe the exact morphology of seaweed using the hydrophilic IL, 1-butyl-3-methylimidazolium tetrafluoroborate, [BMIM)[BF_4]. The IL diluted by water was used as the solvent to maintain the osmotic pressure of the seaweed in the solution.

In chapter 5, the morphologies of the hydrous montmorillonite under different swelling conditions with the aid of the hydrophilic IL using FE-SEM and TEM are observed. The behavior of the IL and water within the hydrated montmorillonite was also studied by XRD to understand the observation mechanism of the hydrous montmorillonite. Additionally, the XRD results are compared to the TEM-SAED results in order to confirm the displacement of the IL and water molecules within the hydrous montmorillonite.

In chapter 6, a direct intercalation of IL into the montmorillonite (*M*) is attempted and the M_{IL} intercalated compounds are fabricated using four kinds of ILs. Thus the fabricated solid-liquid state M_{IL} intercalated compound is observed by TEM to understand the crystal swelling structure in the liquid state. In addition, the XRD results are compared to the TEM-SAED in order to confirm the structures of the M_{IL} intercalated compounds. Based on the cation exchange capacity, the arrangement of the cations in the interlayers of the montmorrilonite clay is proposed. In addition, the sheet resistivity of the M_{BMIMB} intercalated compound is examined in order to fabricate a conducting thin film using the IL and montmorillonite. The thermal stabilities of three kinds of M_{IL} intercalated compounds (M_{EMIO}, M_{TMPAT} and M_{DEMET}) are examined by TG-DTA.

Finally, in Chapter 7, the concluding remarks of the present study are stated and the future directions of this research study are recommended.

References

[1] P.B. Hirsch, A. Howie, R.B. Nicholson, D.W. Pashley, M.J. Whelan, Electron microscopy of thin crystals, Butterworths, London, 1965.

[2] M.H. Loretto, R.E. Smallman, Defect analysis in electron microscopy, Chapman and Hall, London, 1975.

[3] D.B. Williams, C.B. Carter, Transmission electron microscopy, Plenum Press, New York & London, 1975.

[4] H. Saka, Electron microscopy of crystal, Uchidarokakuho, Tokyo, 1997.

[5] B. Howe, J.M. Howe, Transmission electron microscopy and diffractiometry of materials, Springer, Berlin, 2001.

[6] H. Saka, T. Mima, Y. Takeuchi, T. Marukawa, S. Arai, K. Kuroda, K. Kishita, T. Kamino, Microsc. Microanal. 12 (2006) 764-765.

[7] H. Saka, T. Kamino, S. Arai, K. Sasaki, MRS. Bull. 33 (2008) 96-100.

[8] N. Tanaka, J. Yamasaki, K. Usuda, N. Ikarashi, J. Electron. Microsc. 52 (2003) 69-73.

[9] S. Inamoto, J. Yamasaki, E. Okunishi, K. Kakushima, H. Iwai, N. Tanaka, J. Appl. Phys. 107 (2010) 124510.

[10] K. Suenaga, Y. Sato, Z. Liu, H. Kataura, T. Okazaki, K. Kimoto, H. Sawada, T. Sasaki, K. Omoto, T. Tomita, T. Kaneyama, Y. Kondo, Nat. Chem. 1 (2009) 415-418.

[11] N. Shibata, S.D. Findlay, Y. Kohno, H. Sawada, Y. Kondo, Y. Ikuhara, Nat. Phys. 8 (2012) 611-615.

[12] R.A. Schwarzer, Micron 28 (1997) 249-265.

[13] F.J. Humphreys, J. Mater. Sci. 36 (2001) 3833-3854.

[14] C.L. Hussey, Adv. Molten. Salt. Chem. 5 (1983) 185-229.

[15] P. Waden, Bull. Acad. Imper. Sci. St. Petersburg (1914) 1800.

[16] S.G. Kazarian, Appl. Spectrosc. Rev. 32 (1997) 301-348.

[17] J.S. Wilkes, M. J. Zaworotko, J. Chem. Soc., Chem. Commun. 13 (1992) 965-967.

[18] CJ. Adams, M.J. Earle, G. Roberts, K.R. Seddon, Chem. Commun. (1998) 2097-2098.

[19] T. Welton, Chem. Rev. 99 (1999) 2071-2083.

[20] C.W. Lee, Tetrahedron. Lett. 40 (1999) 2461-2462.

[21] K.R. Seddon, Nat. Mater. 2 (2003) 363-365.

[22] R. Sheldon, Chem. Commun. (2001) 2399-2407.

[23] M. Antonietti, D. Kuang, B. Smarsly, Y. Zhou, Angew. Chem., Int. Ed. 43 (2004) 4988-4992.

[24] R. Mareria Lau, F. van Rantwijik, K.R. Seddon, R.A. Sheldon, Org. Lett. 2 (2000) 4189-4191.

[25] J.L. Kaar, A.M. Jesionowski, J.A. Berberich, R. Moulton, A.J. Russell, J. Am. Chem. Soc. 125 (2003) 4125-4131.

[26] D.G. Stevenson, A. Biswas, J. Jane, G.E. Inglett, Carbohyd. Polym. 67 (2007) 21-31.

[27] C. Tsioptsias, C. Panayioţou, Carbohyd. Polym. 74 (2008) 99-105.

[28] S.A. Mousavi Shaegh, N.T. Nguyen, S.H. Chan, Int. Nt. J. Hydrogen. Energ. 36 (2011) 5675-5694.

[29] T.E. Sutto, T.T. Duncan, Electrochim. Acta. 76 (2012) 179-184.

[30] P. Barpanda, J.N. Chotard, C. Delacourt, M. Reynaud, Y. Filinchuk, M. Armand, M. Deschamps, J.M. Tarascon, Angew. Chem. Int. Edit. 50 (2011) 2526-2531.

[31] E. Rozniecka, G. Shul, J.S. Plenet, L. Gaillon, M. Opallo, Electrochem. Commun. 7 (2005) 299-304.

[32] P. Barpanda, E. Rozniecka, G. Shul, J.S. Plenet, L. Gaillon, M. Opallo, J. Solid. State. Electr. 16 (2012) 1743-1751.

[33] S. Hayashi, H. Hamaguchi, Chem. Lett. 33 (2004) 1590-1591.

[34] K. Binnemans, Chem. Rev. 105 (2005) 4148-4204.

[35] K. Ilkka, X. Haibo, K. Alistair, G. Mari, H. Sami, S.A. Dimitris, J. Agric. Food. Chem. 55 (2007) 9142-9148.

[36] T.Q. Yuan, S.N. Sun, F. Xu, R.C. Sun, J. Agric. Food. Chem. 58 (2010) 11302-11310.

[37] J. Kadokawa, M. Murakami, A. Takegawa, Y. Kaneko, Carbohyd. Polym. 75 (2009) 180-183.

[38] O. Aaltonen, O. Jauhiainen, Carbohyd. Polym. 75 (2009) 125-129.

[39] M. Johnston, J.J. Lee, G.S. Chottiner, B. Miller, T. Tsuda, C.L. Hussey, D.A. Scherson, J. Phys. Chem. B 109 (2005) 11296-11300.

[40] T. Torimoto, K. Okazaki, T. Kiyama, K. Hirahara, N. Tanaka, S. Kuwabata, Appl. Phys. Lett. 89 (2006) 243117.

[41] K. Okazaki, T. Kiyama, K. Hirahara, N. Tanaka, S. Kuwabata, T. Torimoto, Chem. Commun. (2008) 691-693.

[42] J.F. Wishart, P. Neta, J. Phys. Chem. B 107 (2003) 7261-7267.

[43] S. Kuwabata, A. Kongkanand, D. Oyamatsu, T. Torimoto, Chem. Lett. 35 (2006) 600-601.

[44] T. Torimoto, K. Okazaki, T. Kiyama, K. Hirahara, N. Tanaka, S. Kuwabata, Appl. Phys. Lett. 89 (2006) 243117.

[45] S. Arimoto, M. Sugimura, H. Kageyama, T. Torimoto, S. Kuwabata, Electrochim. Acta. 53 (2008) 6228-6234.

[46] S. Kuwabata, T. Tsuda, T. Torimoto, J. Phys. Chem. Lett. 1 (2010) 3177-3188.

[47] T. Tsuda, N. Nemoto, K. Kawakami, E. Mochizuki, S. Kishida, T. Tajiri, T. Kushibiki, S. Kuwabata, Chem. Bio. Chem. 17 (2011) 2547-2550.

[48] P. Roy, T. Dey, P. Schmuki, Electrochem. Solid-State. Lett. 13 (2010) E11-E13.

[49] Y. Ishigaki, Y. Nakamura, T. Takehara, N. Nemoto, T. Kurihara, H. Koga, H. Nakagawa, T. Takegami, N. Tomosugi, S. Miyazawa, S. Kuwabata, Microsc. Res. Tech. 74 (2011) 415-420.

[50] Y. Ishigaki, Y. Nakamura, T. Takehara, T. Shimasaki, T. Tatsuno, F. Takano, Y. Ueda, Y. Motoo, T. Takegami, H. Nakagawa, S. Kuwabata, N. Nemoto, N. Tomosugi, S. Miyazawa, Microsc. Res. Tech. 74 (2011) 1024-1031.

[51] Y. Ishigaki, Y. Nakamura, T. Takehara, T. Kurihara, H. Koga, T. Takegami, H. Nakagawa, N. Nemoto, N. Tomosugi, S. Kuwabata, S. Miyazawa, Microsc. Res. Tech. 74 (2011) 1104-1108.

[52] A. Dwiranti, L. Lin, E. Mochizuki, S. Kuwabata, A. Takaoka, S. Uchiyama, K. Fukui, Microsc. Res. Tech. (2012) .

[53] K. Yanaga, N. Maekawa, N. Shimomura, Y. Ishigaki, Y. Nakamura, T. Takegami, N. Tomosugi, S. Miyazawa, S. Kuwabata, Micol. Progress. 11 (2011) 343-347.

[54] K. Kawai, K. Kaneko, H. Kawakami, T. Yonezawa, Langmuir. 27 (2011) 9671-9675.

[55] S.G. Kazarian, B.J. Briscoe, T. Welton, Chem. Commun. (2000) 2047-2048.

[56] S.N.V.K. Aki, J. Brennecke, A. Samanta, Chem. Commun. (2001) 413-414.

[57] L.F. Scatena, M.G. Brown, G.L. Richmond, Sicience 292 (2001) 908-912.

[58] L. Cammarata, S.G. Kazarian, P.A. Salter, T. Welton, Phys. Chem. Chem. Phys. 3 (2001) 5192-5200.

[59] Y. Jeon, J. Sung, D. Kim, C. Seo, H. Cheong, Y. Ouchi, R. Ozawa, H. Hamaguchi, J. Phys. Chem. B. 112 (2008) 923-928.

[60] K. Mizuno, S. Imafuji, T. Ochi, T. Ota, S. Maeda, J. Phys. Chem. B. 104 (2000) 11001-11005.

[61] C.G. Hanke, R.M. Lynden-Bell, J. Phys. Chem. B. 107 (2003) 10873-10878.

[62] H. Katayanagi, K. Nishikawa, H. Shimozaki, K. Miki, P. Westh, Y. Koga, J. Phys. Chem. B. 108 (2004) 19451-19457.

[63] X. Wu, Z. Liu, S. Huang, W. Wang, Phys. Chem. Chem. Phys. 7 (2005) 2771-2779.

[64] S. Saha, H. Hamaguchi, J. Phys. Chem. B. 110 (2006) 2777-2781.

[65] W. Jiang, Y. Wang, G.A. Voth, J. Phys. Chem. B. 111 (2007) 4812-4818.

[66] M. Moreno, F. Castiglione, A. Mele, J. Phys. Chem. B. 112 (2008) 7826-7836.

[67] H. Abe, Y. Yoshimura, Y. Imai, T. Goto, H. Matsumoto, J. Mol. Liquids. 150 (2009) 16-21.

[68] Y. Yoshimura, H. Kimura, C. Okamoto, T. Miyashita, Y. Imai, H. Abe, J. Chem. Thermodynamics. 43 (2011) 410-412.

[69] B. Sun, Q. Jin, L. Tan, P. Wu, and F. Yan, J. Phys. Chem. B. 112 (2008) 14251-14259.

[70] B. Sun, P. Wu, J. Phys. Chem. B. 114 (2010) 9209-9219.

CHAPTER 2

MICROSCOPIC OBSERVATION OF FINE MORPHOLOGY OF AGAR GEL IN VARIOUS SWELLING CONDITION USING HYDROPHILIC IONIC LIQUID

2.1 Introduction

Recent days electron microscopes are used as important material characterization tools due to advancement in technologies especially in high resolution performance images, high resolution analysis equipment and 3D observation abilities [1, 2]. Among various electron microscopy techniques, scanning electron microscopy (SEM) has been popularly used in the scientific community over 40 years due to its wide applications in metals, semiconductors, ceramics, medical and biological field. Compared to solid materials, sample preparation for biological or other wet materials to be observed by SEM is complicated, and, even difficult to maintain the morphology in vacuum condition. Therefore, to observe the exact morphologies of these wet samples, new methodologies are being searched.

Recently room-temperature (RT) ionic liquids (ILs) are used as solvents in various chemical reactions [3-7], or in dispersion of carbohydrate polymers such as cellulose and starch etc [8-10]. Furthermore, composite gel mixed with IL is used in drug delivery

systems and fabrication of contact lenses [11-13]. Besides these applications, ILs mixed with samples can be directly observed in electron microscope due to their negligible vapor pressure and high conductivity [14-17]. Although some reports suggest that wet materials (seaweed, chicken tissue etc) mixed with hydrophilic IL can be observed by SEM without any additional conducting coating [18, 19], still this technique needs to be further applied to other kind of wet materials.

It has been noticed that addition of small amount of water to ILs changed their properties due to the interaction with the water molecules [20-22]. The interaction of IL with water has been reported by various simulations and experimental methods [23-29]. Results showed that both cations and anions of IL played significant role for the formation of hydrogen bond with water molecule, although anions always participate dominantly [20, 30]. Also, the interaction between OH (derived from water) and IL (both anion and cation) in different circumstances are observed by FT-IR spectroscopy and Raman spectroscopy [31-36].

Among various materials, agar gel in its wet condition is popularly used in biology, medicine and food industries. Especially in biochemistry, the agar gel is widely used in culturing media of microbes and in cataphoresis. Furthermore, the agar gel is also used as a gelling agent for various ceramic forming processes due to less hazardous and non-toxicity as compared to acryl amides in traditional gel-casting method. In this method, the agar gel enables to make complex network along with well distributed ceramic particles [37-39]. However, morphology of such complex network structure in wet conditions is difficult to be observed accurately under an electron microscope in vacuum.

In the present study, we report the fine morphology of water-containing agar gel using typical imidazolium IL by FE-SEM under high vacuum. Also we examined the effect of water content in the agar gel and the presence of ethanol in agar gel using Raman spectroscopy. Furthermore the displacement rate of IL into the water-containing agar gel was also investigated in order to understand the displacement mechanism of IL.

However, the detail mechanism of electron microscope observation of such wet agar gel treated with IL has not been clearly understood. Therefore, the objective was to understand the mechanism of FE-SEM observation of agar gel using IL, interaction between water molecules at different concentration within agar gel and IL. The mechanism of interaction was studied in terms of hydrogen bond between anionic part of IL and water molecules (also water molecules within agar gel) using Raman spectroscopy. Furthermore, agar gel treated with IL at different water concentrations was observed by FE-SEM.

Though, existence of IL within agar gel after displacement of the water inside the agar gel is not still clearly understood. In addition, FE-SEM observation of different swelling conditions and water contents of agar gel is not reported before. Therefore, it is essential to investigate the mechanism of FE-SEM observation of agar gel in different hydrated conditions so that this methodology might be suitable for characterization of ceramics, biological materials and composite materials in their wet conditions. Thereby, the exact morphologies of agar gel in different swelling conditions and different water contents using hydrophilic IL are observed by FE-SEM and analyzed the line and area change while keeping in FE-SEM chamber under high vacuum. Also, existence of IL within agar gel after displacement of the water inside the agar gel is examined by differential scanning

calorimeter (DSC). Besides, shrinkage of agar gel due to IL and water interaction is measured. Based on the FE-SEM and DSC results, interaction of water and hydrophilic IL and observation mechanism of agar gel treated with IL is proposed.

2. 2. 1. Materials and methods

2. 2. 1. Materials

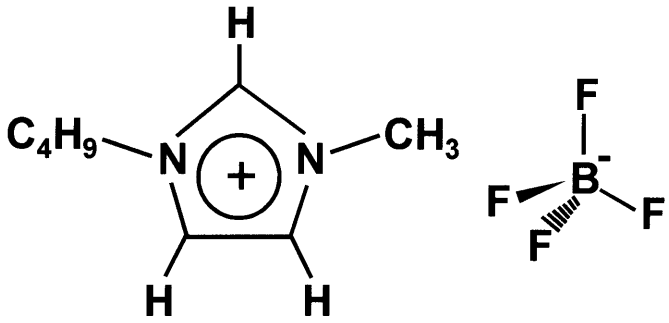

Figure. 2. 1. Chemical structure of ionic liquid used in the present study.

The IL; 1-butyl-3-methylimidazolium tetrafluoroborate ((BMIM)(BF_4)) shown in Figure 2. 1 was directly purchased from Kanto Chemical Co. Japan and dried in a vacuum desiccators at 60 °C for 1 day. In the present study, commercially available agar S-10 (Ina Food Industry Co., Japan) was used. The solidification and melting points were 30 °C and 90 °C, respectively. Ultrapure water (ADVANTEC Co, Japan) and agar were mixed and heated at 150 °C for 5 min. The water content of agar gel was determined by Karl-Fischer titrations. The ethanol was used after removal of the water molecules using molecular sieve (Wako Co., Japan).

2. 2. 2. 1. Methodology of morphological observations of agar gel by laser microscope and FE-SEM.

The morphology of agar gel was observed by a laser microscope (SHIMADZU, OLS 4000) and a JEOL JEM 7600F FE-SEM (operated at 5.0 kV). We used an agar gel with 81. 27 wt % water content and IL with 142 ppm (determined by Karl-Fischer titrations) (Kyoto Electronics Co., Japan. MKA-610). The untreated agar gel was placed on a Cu (3mm φ) mesh in a Petri dish (150 mm φ × 10 mm in height) and the morphology was observed using a laser microscope in air. After observation by laser microscope, the agar gel was cut (sample size: 2.5 × 2.5 × 2.0mm^3) and treated with IL diluted by ethanol which was already mixed in the ultrasonic bath for 30 minutes. It was set in à Petri dish for 2 h in the desiccator. The sample was picked up and mounted on the SEM mounting with a small amount of the IL solution. After vacuum drying over 24 h, the same region of agar gel was observed by FE-SEM. In order to obtain a thin coat of IL, the agar gel was treated with IL diluted by ethanol at several concentrations as trial experiments [18]. When concentration of IL was high, the surface of the agar gel coated with IL become chunky that caused the surface to be unidentifiable. At low IL concentration, a thin IL coating was produced and then dried sufficiently before putting into the vacuum dryer. The agar gel treated with various concentrations of the IL solution was observed by a FE-SEM (used the proportion of materials as 1 : 10 (IL : ethanol on weight basis).The agar gel was prepared using agar, water, IL and ethanol (amount weight ratio; 1: 10 : 293 : 2930) so that the sample contain 30 mol % H_2O. The agar gel without IL was prepared under the vacuum at 60 °C for over 24 h, and coated with osmium using sputter coater (Filgen Co., Japan. OPC 60 A) as a

reference. SEM images were taken in the same area for 1 h at 15-min intervals in high magnification to check the stability for long period. The IMAGE PRO-PLUS^{TM} analysis software was used for analyzing the morphology.

2. 2. 2. 2. Methodology of effect of water content in agar gel on displacement of IL.

The different water-containing agar gels were prepared by mixing agar and water in the weight ratio; 1 : 10 and 1 : 20 and abbreviated as A and B, respectively. The agar gels were prepared at the pyrex tubes of 5.0 mm φ, 0.8 mm wall thickness. (see the Supporting Information Figure 2. 2) Moreover, the total water content of the IL and the agar gel was kept 30 mol % in this study. Raman spectrum was measured at room temperature by a JASCO NRS-3100 laser Raman spectrophotometer equipped with a single monochromator and a CCD detector. The Raman spectrum of the IL + agar gel was taken at the agar side 2.0 mm away from the IL / agar gel interface and 1.0 mm depth from the pyrex surface from 0 to 40 minutes at 5 minutes interval in the range of 2800 to 3800 cm^{-1} using the pyrex tubes and averaged 5 times. The Raman spectrum was taken at 2.5 mW of the 514.5 nm line using an Ar ion laser as the excitation source.

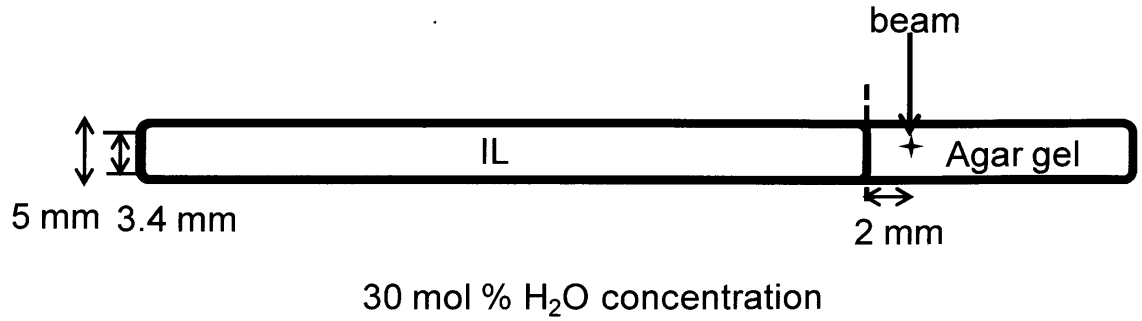

Figure 2. 2. The sample preparation for Raman analysis using Pyrex tubes.

2. 2. 2. 3. Methodology of effect of ethanol in agar gel on displacement of IL.

The agar gel was cut into 2.5 × 2.5 × 2.0 mm^3 in size and treated with IL + ethanol and kept in a desiccator from 0 to 60 minutes. The Raman spectrum was taken on the surface of the agar gel as described above in the range of 2800 to 3800 cm^{-1}.

The agar gel 2.5 × 2.5 × 4.0 mm^3 in size was treated with IL + ethanol for 2 h and kept in a desiccator. After keeping in vacuum for over 24 h (same as SEM sample preparation), the agar gel sample was cut (2.0 mm in height) using a razor blade. The Raman spectra were taken on the surface of agar gel at 0.0, 1.0 and 2.0 mm across the centre from one end to the other end.

2. 2. 2. 4. Methodology of interaction of water and IL using Raman spectroscopy.

Water content of IL was below 128 ppm. Agar was mixed with ultrapure water in the weight ratio 1 : 10 and the gel was prepared. Water content of agar gel was found to be 81.24 wt % as measured by Karl Fisher titrations. The agar gel was cut into 2.5 × 2.5 × 2.0 mm^3 in size and used for further studies.

Water concentrations i.e 15 to 95 mol % were added to IL to study the interaction of water molecules with IL under vacuum condition at 60 °C, 24 h by Raman spectroscopy. Interaction of water and IL mixture of similar concentrations were also measured at RT as reference. This IL and water mixture solution is designated as *[BMT_{Il}/W]* in subsequent discussions.

In another study, agar gel and IL + ethanol mixed solution were added in such a way that the total water concentration in the resultant sample (concentration of water and IL) was gradually varied from 15 to 95 mol %. Table 2. 1 shows the amount of agar, water, IL and ethanol in weight used for sample preparation. It should be noted that ethanol was used only as a solvent for sample preparation. Later, agar gel was removed from IL + ethanol mixed solution and then both agar gel and mixed solution were characterized separately. For clarity, a schematic representation of experiment is shown in Figure 2. Raman spectrum of this mixed solution ($[BMT_{IL}/EtOH\text{-}A_w]$) was measured with respect to water concentration after keeping in a desiccator for 3 h and after keeping in a desiccator for 3 h + vacuum at 60 °C, 24 h due to understand the interaction between IL and water during the FE-SEM sample preparation condition (see in Figure 2. 3).

Table 2. 1. Amount ratio of agar, water, IL and ethanol in weight for Raman spectroscopy and FE-SEM observation.

Material	Amount ratio					
	15	30	60	80	95	(mol % water)
Agar	1	1	1	1	1	
Water	10.0	10.0	10.0	10.0	10.0	
IL	711.5	293.0	83.7	31.4	6.6	
Ethanol	7115.4	2930.0	837.1	313.9	66.1	

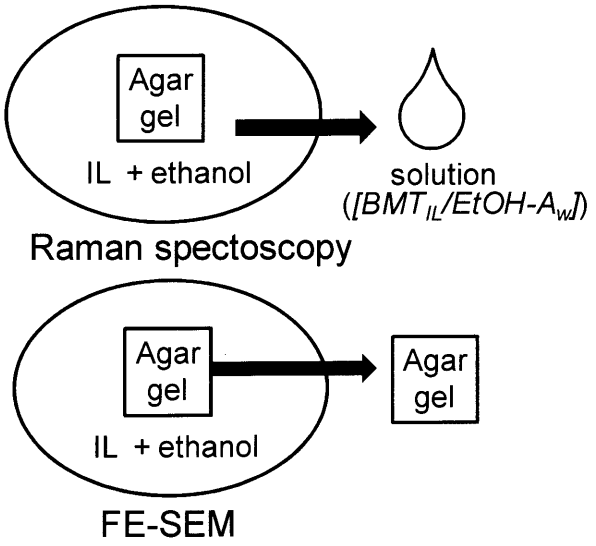

Figure. 2. 3. Sample preparation condition of agar gel treated with IL + ethanol for Raman spectroscopy or FE-SEM observation.

In Raman measurement, solutions were kept in a pyrex tube of 5.0 mm φ, 0.8 mm wall thickness. The Raman spectra were measured at room temperature by a JASCO NRS-3100 (Nihon bunko Co, Japan) laser Raman spectrophotometer equipped with a single monochromator and a CCD detector. The Raman spectrum was taken in the range of 2800 to 3800 cm^{-1} at the 1.0 mm depth from the pyrex surface and averaged 5 times. The Raman spectrum was taken by 2.5 mW of the 514.5 nm line of an Ar ion laser as the excitation source.

2. 2. 2. 5. Methodology of morphological observations of agar gel in different IL / water concentrations by optical microscope, laser microscope and FE-SEM.

The bottom of agar gel which was made from stainless steel case was used for observation. The agar gel removed from the agar gel + IL + ethanol mixture was observed using an optical microscope, laser microscope (SHIMADZU Co, Japan, OLS 4000) and field emission scanning electron microscope (JEOL Co, Japan, JEM 7600F) with accelerating voltage of 5.0 kV (see in Figure 2. 3). Agar gel containing 30 mol % water was observed in optical microscope and laser microscope. However, agar gels with 15 to 95 mol % water were used to optimize the water content in gel to be observed in FE-SEM condition.

2. 2. 2. 6. Methodology of size retention of the agar gel in different water concentrations after IL treatment.

Size retention of the agar gel with 15 to 95 mol % water was measured after keeping in a desiccator for 3 h and vacuum condition at 60 °C for 24 h (as FE-SEM sample preparation). Each agar gel was cut into 2.5 × 2.5 × 2.0 mm^3 in size and the measurement was carried out.

2. 2. 2. 7. Methodology of morphological observation of agar gel in different swelling condition by optical microscope, laser microscope and FE-SEM.

Water content of IL was below 128 ppm. Agar powder was mixed with ultrapure water in the weight ratio 1 : 10 and the gel was prepared. Two types of agar gel in different swelling condition were prepared. In first type, agar gel mixed with water was heated at 150 °C for 1 min and cooled to room temperature and is described as paste condition

(Water content: 89.67 wt % from Karl-Fisher titration). In second type, the agar gel mixed with water was heated at 150 °C for 3 min and cooled to room temperature and is described as soft solidification condition (Water content: 84.35 wt %). It is noted that almost agar powder is swelled by water in soft solidification condition as compared to paste condition, although water contents of agar gel in paste condition is high.

Agar gel was characterized using optical microscope (KEYENCE, VHX-200, Japan), laser microscope (SHIMADZU, OLS 4000, Japan) and field emission scanning electron microscope (FE-SEM, JEOL, JEM 7600F, Japan) with accelerating voltage of 5.0 kV. The natural morphology of agar gel without IL treatment was observed by optical and laser microscope by placing the sample on a Cu mesh (3mm φ) kept in a Petri dish (150 mm φ × 10 mm height). After that, Cu mesh with agar gel was picked up and treated with IL solution as per the method described as below. For FE-SEM observation, agar gel in paste and soft solidification conditions were prepared using agar, water, IL and ethanol in a amount ratio of 1 : 10 : 293 : 2930. The total water concentration in the resultant sample (concentration of water and IL) was adjusted to 30 mol %. It should be noted that ethanol was used only as a solvent for sample preparation. The FE-SEM photographs of agar gel with IL were compared with laser microscope. Besides, high magnification images of samples were taken using FE-SEM for 1 h in 15 min interval and all the images were analyzed using IMAGE PRO-PLUS^{TM} analysis software to confirm any morphological changes in the wet sample in vacuum condition.

2. 2. 2. 8. Existence of IL within agar gel.

Differential scanning calorimeter (DSC, RIGAKU, DSC8230, Japan) measurements of agar gel (paste and soft solidification conditions) and IL mixtures were performed in the range of -100 °C to 200 °C with a heating rate of 10 °C / min using liquid nitrogen to determine a glass transition endotherm of IL, and melting and volatilization endotherms of water in the mixtures. Three types of agar gel samples in different preparations i.e. without any treatment, with IL treatment and kept in desiccator for 2 h and with IL treatment and kept in desiccator for 2 h + under vacuum at 60 °C for 24 h are used. In each case, about 10 mg of sample was put into aluminum pan and the measurement was carried out.

Besides, DSC measurement of water and IL mixtures of different water concentrations were performed in the range of 30 to 200 °C with a heating rate of 10 °C / min to determine the volatilization endotherms of water in the mixtures. Four types of samples in different preparations i.e. 15, 30, 45 mol % water concentrations in IL after kept in desiccator for 2 h and 45 mol % water concentration after kept in desiccator for 2 h + under vacuum at 60 °C for 24 h are used.

2. 2. 2. 9. Volume shrinkage of agar gel after IL treatment.

Agar gel in soft solidification condition was used for measurement of volume change after IL treatment. Volume of IL displaced water within agar gel was calculated using density of IL and water mixture and the residual weight of sample. 10 mg of agar gel was used for this measurement.

2. 3. Results and discussions

2. 3. 1. Morphology of agar gel using laser microscope and FE-SEM.

Figure 2. 4a and b shows laser microscope and FE-SEM image of agar gel treated with IL + ethanol. For comparison, FE-SEM of agar gel without IL was observed and is shown in Figure 1c.

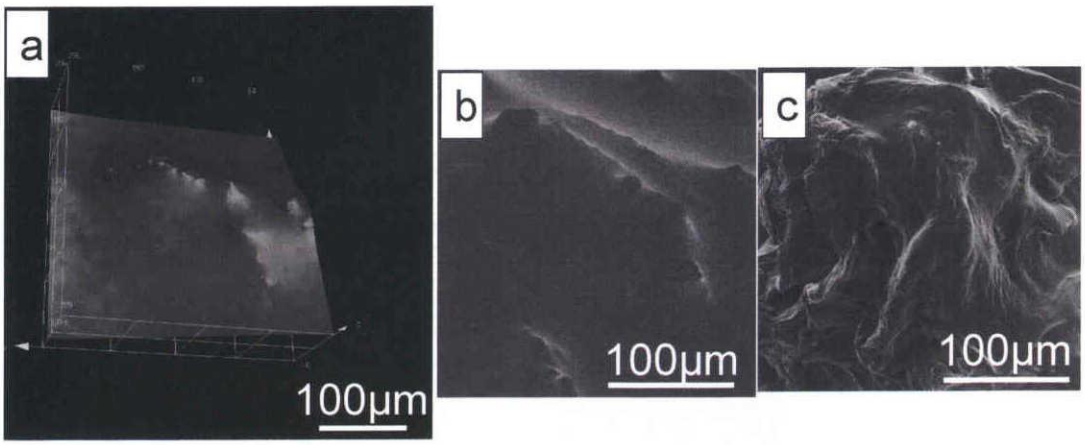

Figure. 2. 4. Comparison of (a) laser microscope image of agar gel, (b) FE-SEM image of an agar gel + IL diluted by ethanol and (c) FE-SEM image of an agar gel using osmium coating. The accelerating voltage for FE-SEM observation was 5.0 kV.

It can be seen from Figure 1a that most of the sample parts were flat with no asperities even on the surface. Although the agar gel with IL was exposed to the vacuum, the morphology of the agar gel could be clearly observed (as seen in Figure 2. 4b). The SEM image of the agar gel using osmium coating (Figure 2. 4c) showed the aggregates to be significantly different from that of Figure 1b. Though the surface of the agar gel treated with the IL was flat, the morphology of agar gel using this method was a layered structure with wrinkles. From this result, it can be concluded that the conventional method was not suitable to observe the accurate morphology of water-containing materials using FE-SEM

due to the vaporization of the water molecules from the agar gel inside the chamber. On the other hand, there was no difference in the morphology of agar gel using laser microscope or FE-SEM without IL or with IL, respectively. Then, morphology of the agar gel treated with IL (30 mol % H_2O) was remained stable and could be accurately observed without any charging at a low accelerating voltage. Furthermore, the agar gel and IL did not show any interaction. This result showed that the morphology of the agar gel was not drastically changed by the IL solution even if the IL was diluted by ethanol.

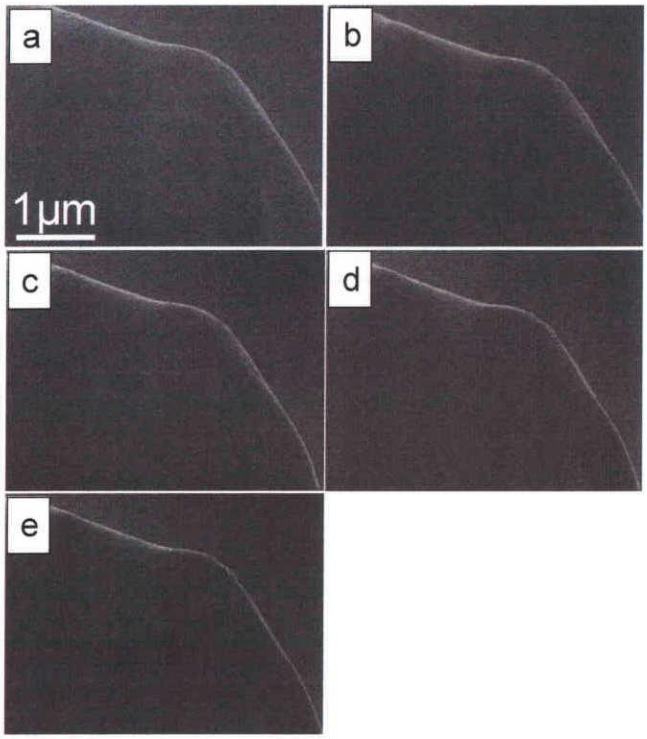

Figure. 2. 5. Magnified FE-SEM images (Accelerating voltage, 5.0 kV) of agar gel + IL diluted by ethanol at (a) 0, (b) 15, (c) 30, (d) 45 and (e) 60 min.

Figure 2. 5 shows FE-SEM images of the agar gel using IL at different time interval. For comparison, morphology of same region as that of Figure 2. 4b at a high magnification was chosen. Because the sample was observed using various magnifications at different time, there were some movements in comparison to the images with respect to the starting time. Results showed that the water-containing agar gel could be clearly observed at high magnification and the fine structure of the surface morphology remained unchanged.

There were no significant differences in the form of the individual images from the point of view of visibility, although the water and IL interact with each other [28]. The agar gel with IL was stable enough to be observed except for the cases when high accelerating voltage and high intensity beam was used. The morphology of the agar gel was clearly observed even at high magnification by this method (see in the Supporting Information Figures 2. 6, 2. 7 and Table 2. 2).

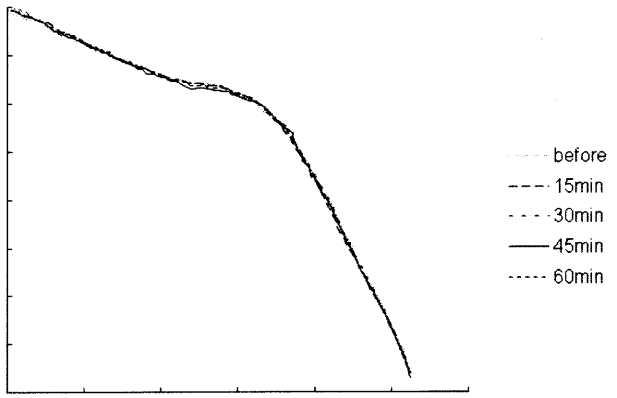

Figure. 2. 6. Comparison of outline of agar gel + IL diluted by ethanol. Plot outline at different time using analysis software.

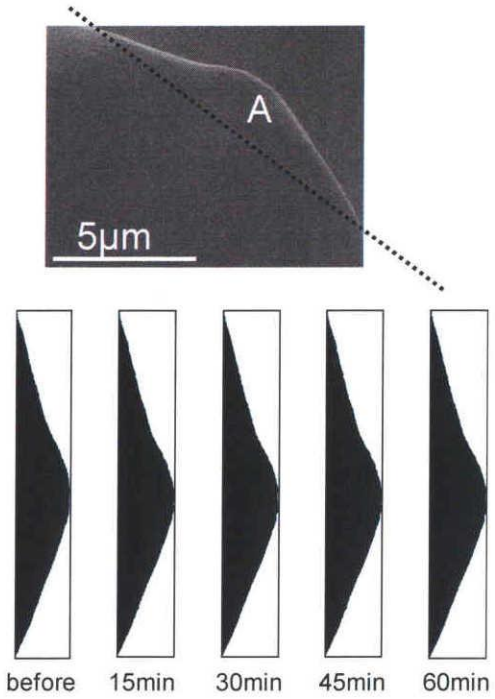

Figure. 2. 7. Comparison FE-SEM image of agar gel using analysis software at different time.

Table 2. 2. Differential ratio of line length and area at 15 to 60 min as compared with original.

Time (min)	Differential ratio (%)	
	outline	area
0	-	-
15	0.20	0.44
35	0.33	0.07
45	0.49	0.11
60	0.20	0.97

2. 3. 2. Effect of water content in agar gel on displacement of IL.

Figure 2. 8 shows the Raman spectra of IL + agar gel prepared with different water content at different time interval. In this study, we consider the CH and OH stretching vibration in the region of 2800 to 3800 cm^{-1} due to interaction between the water and IL from 0 to 40 min. The symmetric and asymmetric CH stretching mode of the $(BMIM)^+$ cation appeared in the region of 2800 to 3200 cm^{-1}. The broad peak in the range of 3000 to 3800 cm^{-1} of the bulk water (OH group) represents the non homogeneous environment of water molecules due to hydrogen bonding. The observed CH stretching vibrations region of 2800 to 3050 cm^{-1} was mainly attributed to the agar gel.

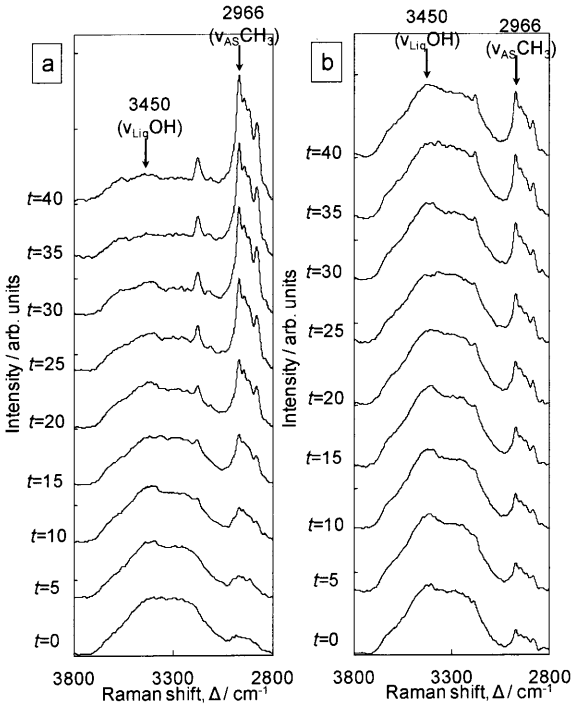

Figure. 2. 8. Raman spectra of IL + agar gel consist of 30 mol % H_2O in the region of 2800 to 3800 cm^{-1} at different time (t express in minute). The arrows show the strong peaks of the OH and CH stretching vibration region in the range of 2800 to 3700 cm^{-1}. (a) Water and agar in 10 : 1 ratio (b) Water and agar is in 20 : 1 ratio.

From Figure 2. 8a, it can be seen that, when IL was mixed with A mainly showed the OH spectrum of water molecule in the initial period. Interestingly, the intensity of CH vibration peak of the $(BMIM)^+$ cation gradually increased up to 40 minutes. On the other hand, the spectrum of Figure 2. 8b was mainly formed by the OH spectral range of water molecule even after 40 minutes, although a small intense CH peak appeared around 3163 cm^{-1} from the CH normal mode vibrations of hydrogen attached directly to the imidazolium ring. The hydrophilic IL is known as highly hygroscopic, and interacts even with a small amount of water. Previous studies reported the IL + water interaction [21, 24, 28] wherein hydrogen bonding had an important role in the interactions during the IL and water. Cammarata and co-workers obtained OH and CH peaks of the IL + water mixtures at various concentrations using Raman spectroscopy [21]. In the present study, the OH spectral range of the water molecule was much wider than the results published in the literature, even though we have used the same condition (30 mol % H_2O in the agar gel and IL) [33, 34]. Hence, the displacement of IL to the agar gel was confirmed to be occurred at a slow rate.

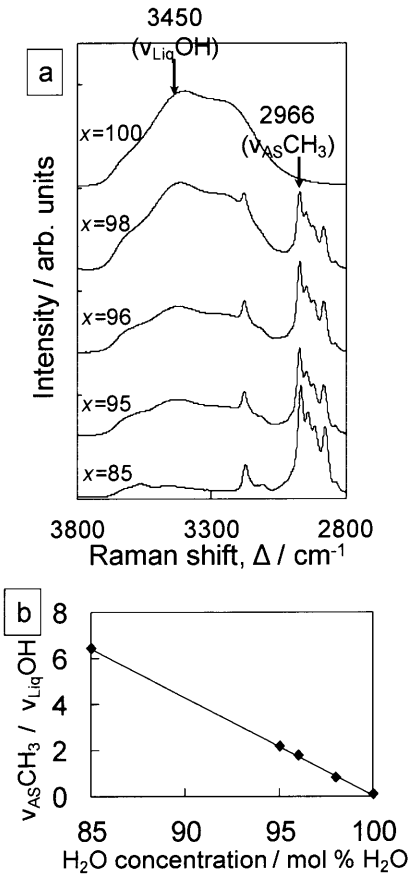

Figure 2. 9. (a) Raman spectra of IL with different H_2O concentrations (x express in mol % H_2O) in the region of 2800 to 3800 cm^{-1}. The arrows show the strong peaks of the OH and CH stretching vibration region in the range of 2800 to 3700 cm^{-1}. (b) Ratio of CH vibration peaks to OH vibration peaks in IL + water with increasing water concentration.

Figure 2. 9a shows the Raman spectra of IL + water with varying water content. In order to understand the displacement of the IL into the agar gel, the peak height ratio $\nu_{AS}CH_3$ to $\nu_{Liq}OH$ of IL + different water content as obtained from Raman spectroscopy (see

in Figure 2. 9b). Figure 2. 9a represents 2966 cm^{-1} as the IL peak and 3450 cm^{-1} as the water peak. The stretching mode peak at 2966 cm^{-1} was assigned to $\nu_{as}CH_3$ (as represents the antisymmetric stretch mode) of butyl chain from cation and stretching mode peak at 3450 cm^{-1} was assigned to $\nu_{Liq}OH$ (Liq represents liquidlike peak) of hydrogen bonding [20, 28-30]. The water concentration (IL concentration) can be obtained using the peak height ratio $\nu_{AS}CH_3$ to $\nu_{Liq}OH$ of spectra of the IL + water mixtures and is represented as

$$y = (42.647 - x) / 0.426 \qquad (1)$$

where, y is the water concentration; x is the peak height ratio $\nu_{AS}CH_3$ to $\nu_{Liq}OH$. Based on the equation (1), we can obtain the water concentration during the mixtures of agar gel + IL. After the CH stretch vibration regions of 2800 to 3050 cm^{-1} derives from the agar gel were completely removed, the peak height ratio $\nu_{AS}CH_3$ to $\nu_{Liq}OH$ of the spectra of agar gel + IL was calculated. (see in Figure 2. 10a) Using this results, the water concentration during the agar gel + IL was obtained from formula (1) (see Table 2. 3).

Table 2. 3. Water concentration during the mixtures of agar gel + IL obtained from formula (1).

	Time (min)	0	5	10	15	20	25	30	35	40
Condition A	Ratio ($\nu_{AS}CH_3$ / $\nu_{Liq}OH$)	0	0.07	0.29	0.64	1.06	1.89	2.58	3.42	3.74
	Concentration (mol % H_2O)	100	99.94	99.43	98.60	97.61	95.68	94.05	92.07	91.34
Condition B	Ratio ($\nu_{AS}CH_3$ / $\nu_{Liq}OH$)	0	0.36	0.43	0.48	0.56	0.71	0.72	0.82	0.86
	Concentration (mol % H_2O)	100	99.26	99.11	98.98	98.79	98.45	98.42	98.18	98.09

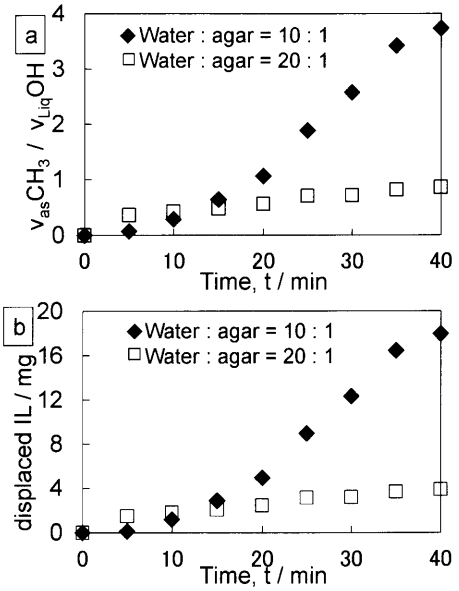

Figure. 2. 10. (a) Ratio of CH vibration peaks to OH vibration peaks in the IL + agar gel at different time. (b) Approximate graph of displacement rate of IL to agar gel.

Therefore, amounts of displaced IL can be calculated from the IL concentration and water content within agar gel. The approximate graph of the IL displacement rate is shown in Figure 2. 10b. The IL displacement rate of A (Figure 2. 8a) was 4.56×10^{-4} cm^3 / min, while the B (Figure 2. 8b) was 7.78×10^{-5} cm^3 / min. Up to 5 minutes, the displacement rate of IL to B was much faster compared to the agar swelled by A, however, after 15 minutes, the IL displacement rate was reversed. Based on the result of the in-situ Raman spectroscopy the IL displacement rate was quite slow and the displacement rate of agar gel using a large amount of water was slower than using small amount of water. We suggested that the IL first interacts with the water molecules on the surface of the agar gel, but the IL

started to interact with water molecules that were brought into the three dimensional network of the double helix structure after 15 minutes. Based on these results, the agar gel using small amount of water easily interacts with IL by the water molecules that produced the three dimensional network of the double helix structure.

2. 3. 3. Behavior of ethanol in IL diluted by ethanol + agar gel.

The Raman spectra in the CH-stretch region of IL diluted by ethanol + agar gel at different time interval in air are shown in Figure 2. 11. The agar gel was prepared with agar and water in the amount ratio of 1 : 10, and treated with IL diluted by ethanol. In order to understand the behavior of ethanol used in the SEM observation, the Raman spectra were measured during treatment with the IL solution. The surface of the agar gel (which directly contacts the IL solution) was selected for the Raman analysis due to not paying attention to the displacement of the IL.

In this study, we considered the region of 2800 to 3200 cm^{-1} derived from the CH stretch vibration region of agar, ethanol and IL. At the beginning of the IL treatment (0 to 10 minutes), the ethanol peaks appeared in the CH stretch vibration region and after 20 minutes, the IL peak appeared clearly. As observed, the peak at 3163 cm^{-1} from the CH normal mode vibrations of hydrogen attached directly to the imidazolium ring starts to significantly increase and the peak at 0 minute shows OH stretching vibrations derived from the water in the agar gel. The spectrum of ethanol was not observed beyond 30 minutes. Contrary to expectations, it appeared that ethanol into the agar gel volatilized during the 2-h treatment of the IL solution without vacuum condition.

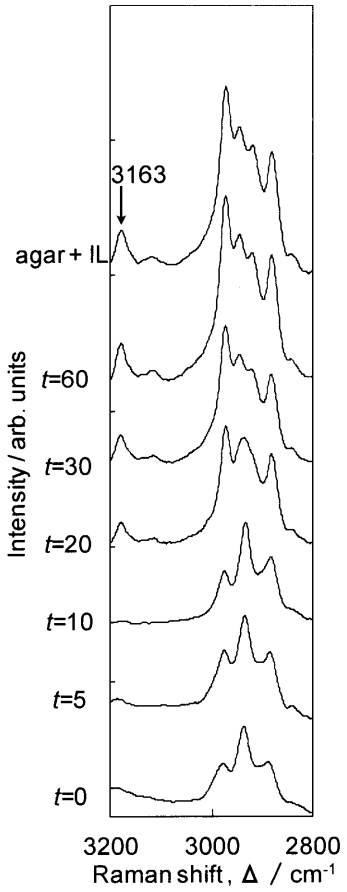

Figure. 2. 11. Raman spectra of IL diluted by ethanol + agar gel consist of 30 mol % H_2O at different time (t express in minute). The topmost line represents spectrum of agar + IL.

Figure 2. 12 compares the Raman spectra of IL diluted by ethanol + agar gel and IL + agar gel (both containing 30 mol % H_2O) kept in vacuum for over 24 h. The observation of the agar gel in both condition showed similar spectra at three different positions defined

as 0, 1.0, and 2.0 mm. As observed, the behavior of ethanol and water into the agar gel explains the existence of ethanol and water in the SEM observations.

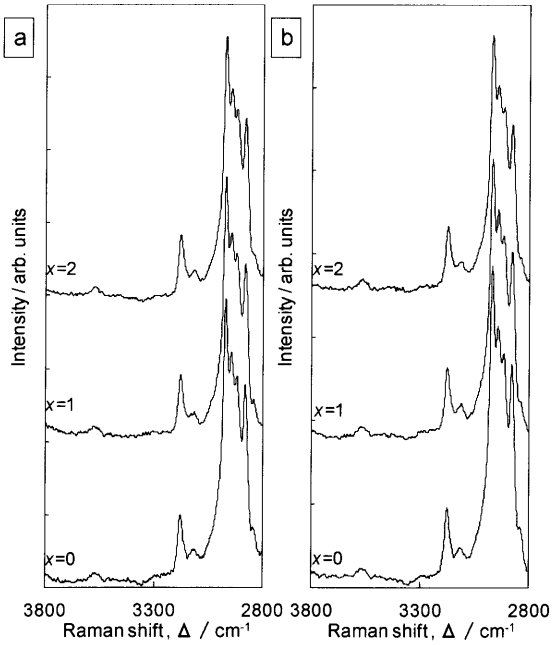

Figure. 2. 12. Raman spectra of (a) IL diluted by ethanol + agar gel, (b) IL + agar gel consist of 30 mol % H_2O at different positions (x express in mm) after keeping in vacuum for over 24 h.

In the spectrum of the CH stretch vibration regions, 2800 to 3200 cm^{-1}, the $(BMIM)^+$ cation showed a similar peak both in Figure 2. 12a and b at different positions. Although the agar-derived spectrum was included in the CH peak, the peak intensity from the $(BMIM)^+$ cation was too strong to confirm the agar peak. The spectrum of the OH stretch vibration region, 3000 to 3800 cm^{-1}, derived from the water and agar gel had a similar peak at each position. From this result, it was revealed that ethanol had no effect on changing the OH stretch vibration region derived from water and agar. The displacement of the IL clearly

occurred at the 2.0 mm depth of the agar gel, because the CH peaks of the $(BMIM)^+$ cation could be mainly observed. Still theresults of the OH stretch vibration region spectra were not appreciably accurate, because it can be assumed that some of the water in the agar gel vaporized during the vacuum treatment and contained an OH peak derived from the agar. The state of the water and the displacement rate of IL inside the agar gel cannot be totally confirmed by the present study.

2. 3. 4. Interaction of water and IL at various conditions as observed by Raman spectroscopy.

Figure 2. 13a and b shows the Raman spectra of *[BMT_{IL}/W]* solution at different water concentrations in the range of 2800 to 3800 cm^{-1} in RT and in vacuum at 60 °C for 24 h, respectively. The CH and OH stretch vibrations region in the range of 2800 to 3800 cm^{-1} were chosen in order to examine the interaction between water, $(BMIM)^+$ and $(BF_4)^-$. We examined the interaction of IL and water after keeping in vacuum condition in order to confirm the existence of water molecules in IL while observation of agar gel samples under FE-SEM. Raman result as shown in Figure 2. 13a of *[BMT_{IL}/W]* in RT (reference) is similar to the Cammarata et al. study [21]. They reported that the water molecules dissolved in IL; (BMIM)(BF_4) are free water molecules, interacting via hydrogen bond with the anion i.e $BF_4^- \cdots$H-O-H$\cdots BF_4^-$. In Figure 2. 13a, we observed the blueshift of the OH peaks on addition IL (abbreviated as OH_A, four νOH vibrations). This blueshift indicates that the addition of water to IL disrupt the hydrogen bonding network of water molecule. Thus, the strength of hydrogen bonding was indicated by the peak position. Additionally, the peak

shifts of ν_{AS} CH_3 at 2876 cm^{-1} and ν_{SS} CH_3 at 2966 cm^{-1} (derives from the butyl chain of the cation) was also observed. We abbreviate both CH peaks (ν_{AS} CH_3 and ν_{SS} CH_3) as CH_B. The peak shift was ascribed to the CH···O interaction due to electronic repulsion and dispersion interaction between the electron of the hydrogen atom of CH and the oxygen atom of water molecule [40]. When water concentration was below 60 mol %, the OH peak at 3560 cm^{-1} was clearly observed similar to previous report (see in Figure 2. 14a) [32].

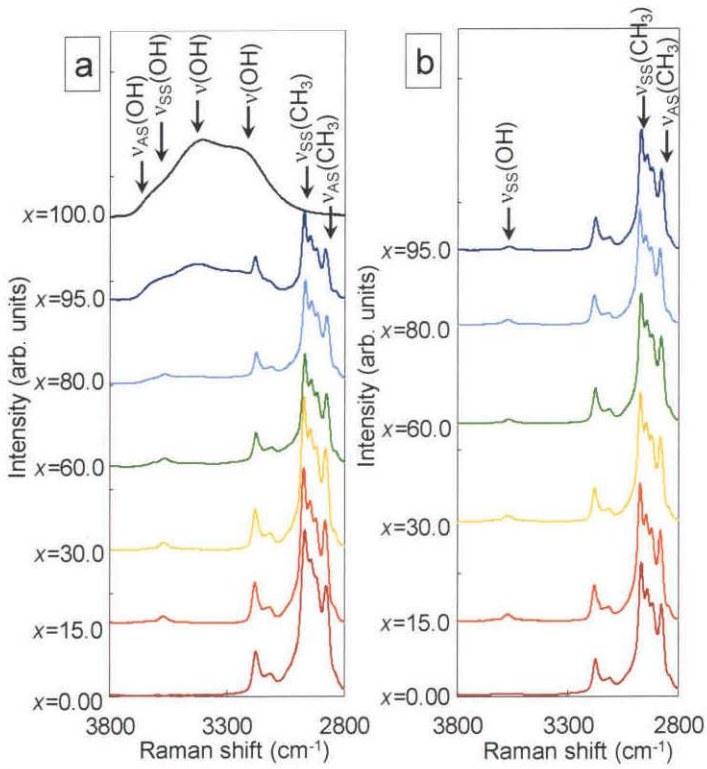

Figure. 2. 13. Raman spectra of *[BMT_{IL}/W]* solution at different water concentrations (x; unit of water in mol %) in the range of 2800 to 3800 cm^{-1} (a) at room temperature, (b) after keeping in vacuum at 60 °C for 24 h. The arrows show the peaks of the OH and CH [$\nu_{SS}(CH_3)$ and $\nu_{AS}(CH_3)$] stretching vibrations.

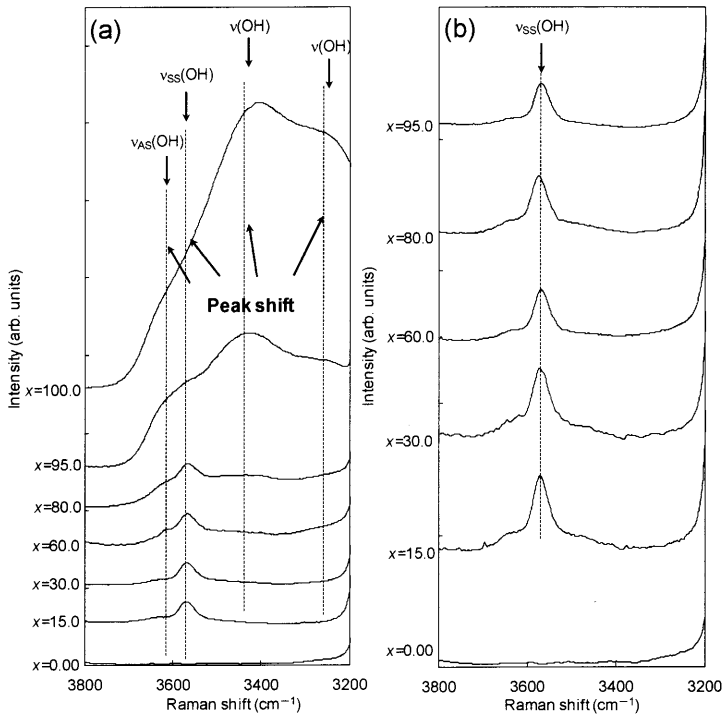

Figure. 2. 14. Raman spectra of *[BMT$_{II}$/W]* solution at different water concentration (x; unit of water in mol %) in a close region (3200 to 3800 cm^{-1}) (a) at RT, (b) after keeping in vacuum at 60 °C, 24 h.

Figure 2. 13b shows Raman spectra of *[BMT$_{II}$/W]* at various water concentrations after keeping the samples under vacuum condition at 60 °C for 24 h. Results showed that, when the mixtures were exposed to the vacuum for 24 h, only the weak hydrogen bond peak around 3560 cm^{-1} was observed in each spectrum of *[BMT$_{II}$/W]* irrespective of water concentration. This peak is attributed to the $BF_4^-\cdots HOH\cdots BF_4^-$ formation even under a vacuum condition at 60 °C for 24 h (see in Figure 2. 14b). It should be noted that the peak for pure water (100 mol %) could not be observed because of evaporation of all water under vacuum condition. Thus, present result is in good agreement with Wu et.al where they

reported that hydrogen bond between water and (BMIM)(BF_4) cannot be completely broken even at 190 °C in 15 mol % water concentration [27]. This weak OH stretching vibration peak (3560 cm^{-1}) could also be observed for 15 mol % water concentration even in vacuum condition as noticed in the present study.

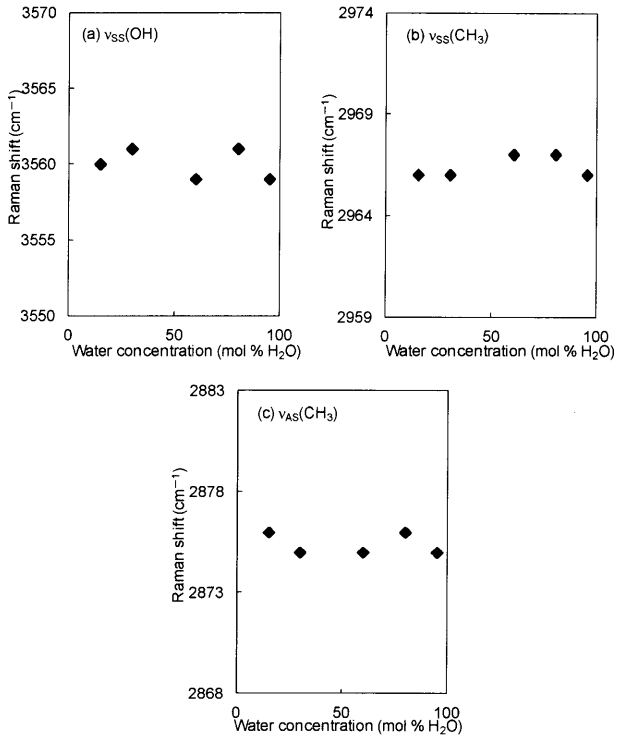

Figure. 2. 15. Raman peak shift of (a) ν_{SS}(OH), (b) ν_{SS}(CH_3) and (c) ν_{AS}(CH_3) with different water concentrations of *[BMT_{IL}/W]* solution after keeping in vacuum at 60 °C, 24 h.

Interestingly, the peaks from OH_A and CH_B did not show any shift from their positions irrespective of water concentrations under vacuum condition as compared to RT condition (see in Figure 2. 15). It can be seen that the extent of hydrogen bond formed in

each mixture are of similar strength under the vacuum condition (Figure 2. 13b) as compared to the samples kept in RT (Figure 2. 13a) at different water concentration.

This indicates that the *[BMT_{IL}/W]* mixture can maintain stable water state even in vacuum condition due to the formation of weak hydrogen bond. Excess amount of water are easily evaporated in vacuum at 60 °C.

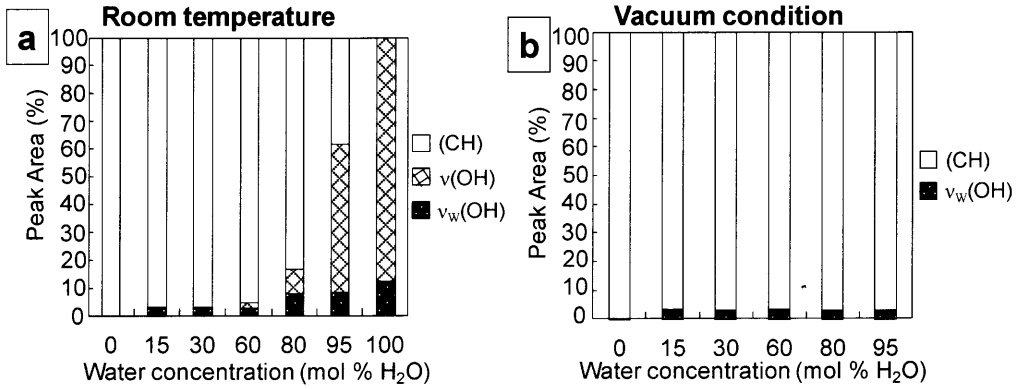

Figure. 2. 16. The OH and CH peak areas of *[BMT_{IL}/W]* in the region of 2800 to 3800 cm^{-1} (a) in RT and (b) after keeping in vacuum at 60 °C for 24 h. ν(OH) shows hydrogen bonding and ν_W(OH) shows weak hydrogen bonding.

Figure 2. 16a and b shows the quantitative analysis of OH and CH content from the peak area of the OH and CH stretching vibration regions as observed from Figure 3a and b, respectively. The 0 mol % water represents pure IL without any water, and 100 mol % water represents pure water as reference. The peak area is indicated by percentage against CH and OH peaks in the range of 2800 to 3800 cm^{-1}. On addition of water at RT, the OH peak area increased remarkably (Figure 2. 16a) and the trend showed significant for 15 to

30 mol % water concentrations. It can be considered that characteristics interaction between water and $(BF_4)^-$ occurred around these concentrations at RT (see in Figure 2. 14a).

Figure 2. 16b shows the change of peak area of IL at different water concentrations after keeping in vacuum at 60 °C for 24 h. Small OH peak area was observed with several % at each *[BMT_{IL}/W]* condition. The important implications of these findings is that a small amount of weak hydrogen bond always exist in (BMIM)(BF_4) without complete evaporation of water molecules (even in the vacuum dryer), and similar amount of weak hydrogen bond exist in IL regardless of water concentrations. Here, pure water (100 mol % water) was not indicated because of complete evaporation in vacuum condition.

2. 3. 5. Interaction of IL in presence of ethanol and water in agar gel.

The Raman spectra of *[BMT_{IL}/EtOH-A_w]* solution with respect to water concentration after keeping them in desiccator for 3 h and keeping in a desiccator for 3 h + under vacuum condition at 60 °C for 24 h are shown in Figure 2. 17. Figure 2. 17a shows the Raman spectra of *[BMT_{IL}/EtOH-A_w]* in various water concentrations keeping for 3 h in the desiccator. This condition was selected for Raman analysis because agar gel was kept in the same condition prior to FE-SEM observation. Mixture of IL diluted by ethanol and agar gel is put in desiccator in order to displace IL into the agar gel. In this study, we measured such a sample condition owing to understand the existence of water within agar gel during sample preparation for FE-SEM observation. The symmetric $BF_4^- \cdots HOH \cdots BF_4^-$ stretching mode (ν_1) peak was observed at 3560 cm^{-1} and the OH peak position did not change with respect to water concentration. In this study, we have not considered OH peak derived from

agar due to quite small OH peak and hence no significant interaction with BF_4 anion is expected. The blueshift of CH_B peaks position was also not observed (see in Figure 2. 18a and 2. 19).

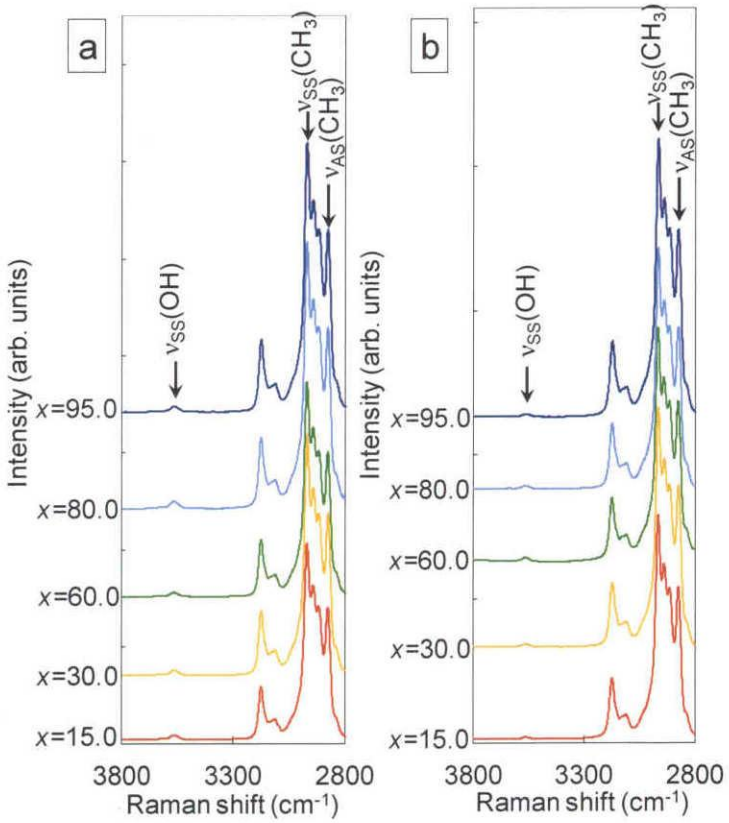

Figure. 2. 17. The Raman spectra of *[BMT_{IL}/EtOH-A_w]* solution treated with different water concentrations (x: unit of water in mol %) as per the condition in Table 1. (a) Keeping in a desiccator for 3 h, (b) keeping in a desiccator for 3 h + under vacuum condition at 60 °C for 24 h. The arrows show the peak of the $\nu_{SS}(OH)$, $\nu_{SS}(CH_3)$ and $\nu_{AS}(CH_3)$ stretching vibration region.

Nevertheless each mixture was prepared with different water concentrations, the small area of weak hydrogen bond was only observed after evaporation of ethanol. From these results, it is considered that only fixed amount of water from the agar gel moved to IL solution during 3 h keeping in the desiccator. Therefore it could be understood that different amount of water exists within agar gel depending on water concentration of *[BMT_{Il}/EtOH-A_w]*.

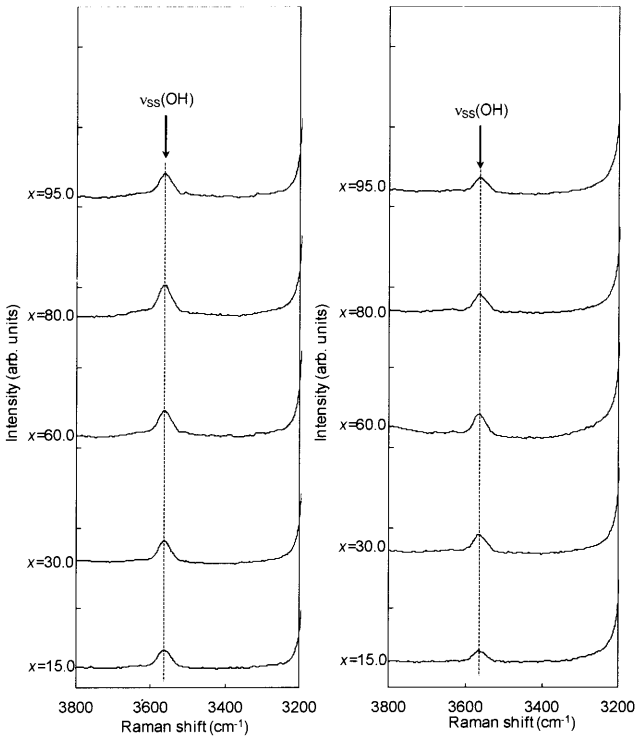

Figure. 2. 18. Raman spectra of *[BMT_{Il}/EtOH-A_w]* solution at different water concentration (x; unit of water in mol %) in a close region (3200 to 3800 cm^{-1}) (a) after keeping in a desiccator for 3 h and (b) after keeping in a desiccator for 3 h + vacuum at 60 °C, 24 h.

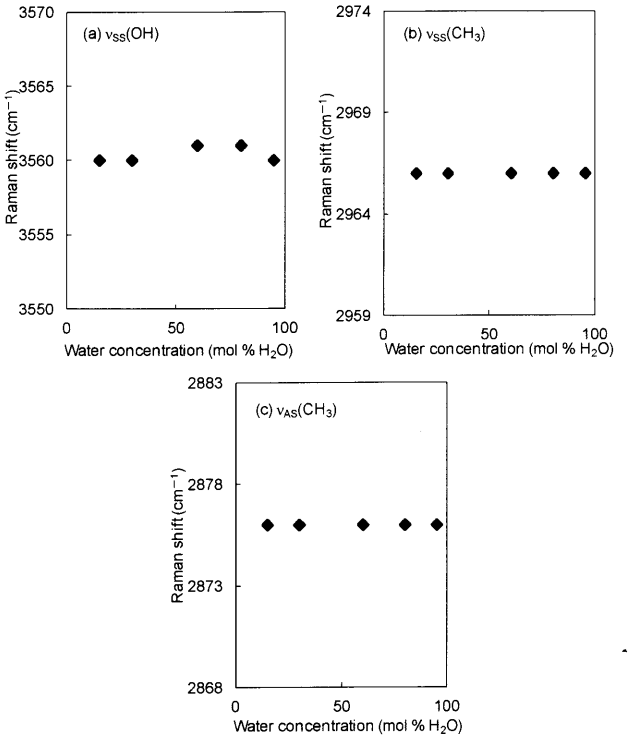

Figure. 2. 19. Raman peak shift of (a) ν_{SS}(OH), (b) ν_{SS}(CH_3) and (c) ν_{AS}(CH_3) with different water concentrations of *[BMT_{Il}/EtOH-A_w]* solution after keeping in a desiccator for 3 h.

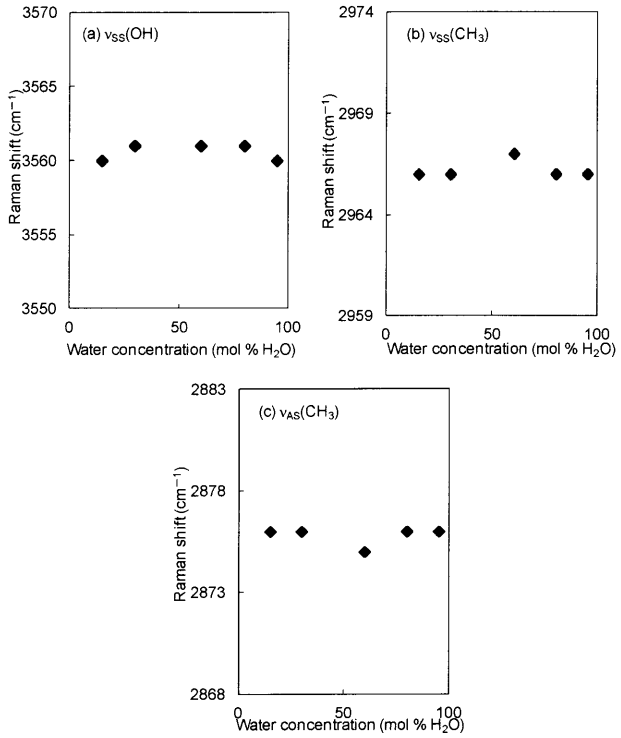

Figure. 2. 20. Raman peak shift of (a) ν_{SS}(OH), (b) ν_{SS}(CH_3) and (c) ν_{AS}(CH_3) with different water concentrations of *[BMT_{IL}/EtOH-A_w]* solution after keeping in a desiccator for 3 h + vacuum at 60 °C, 24 h.

Figure 2. 17b shows the Raman spectra of *[BMT_{IL}/EtOH-A_w]* solution after keeping in a desiccator for 3 h + under vacuum condition at 60 °C for 24 h. The small OH peak at 3560 cm^{-1} was also observed in each spectrum irrespective of water concentration without complete evaporation, and the peak did not change its position with the addition of water. As expected, the blueshift of CH_B peaks position was also not observed. (see in Figure 2. 18b and 2. 20,) Though the area of symmetric stretch mode of weakly bonded OH decreases due to the evaporation of some water during vacuuming, the formation of weak hydrogen

bond such as $BF_4^-\cdots HOH\cdots BF_4^-$ did not disappear completely. Hence, it can be interpreted that IL binding ability to the water molecules is quite high. Moreover, from these results, it is clear that water amount within agar gel is different for 15 to 95 mol % water containing samples. Therefore, we need to confirm the agar gel morphology in different water concentrations using optical microscope, laser microscope and FE-SEM.

2. 3. 6. Optical microscope observation of agar gel treated with IL.

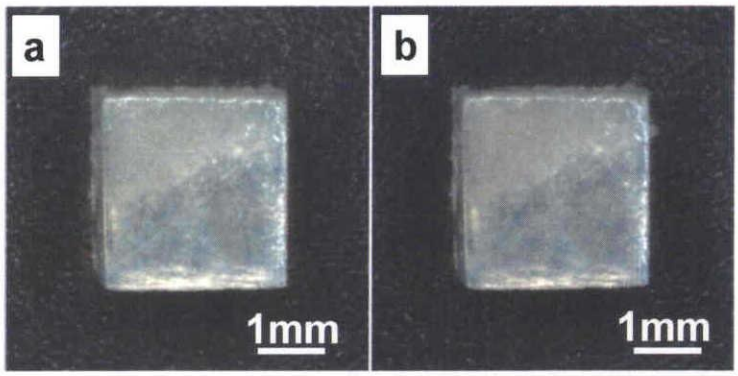

Figure. 2. 21. Comparison of optical microscope images of (a) as-prepared agar gel and (b) as-prepared agar gel subsequently treated with IL after adjusting water concentration to 30 mol %.

In order to understand the mechanism of FE-SEM observation using IL, agar gel was observed by optical microscope at RT. Figure 2. 21a and b shows optical microscope image of as-prepared agar gel and agar gel treated with IL adjusting the water concentration to 30 mol %, respectively. Results showed that agar gel morphology was not changed even after immersion in IL. From IL displacement rate of our previous study, it is considered that

IL penetrated completely into agar gel size 2.5 × 2.5 × 2.0 mm^3, while maintaining the same shape [15].

2. 3. 7. Laser microscope and FE-SEM observation of agar gel treated with IL.

Figure 2. 22a and b shows the comparison of laser microscope images of the as-prepared agar gel and agar gel that was kept in a desiccator for 3 h, respectively. It is clear from these figures that the morphology of agar gel was remarkably changed with time when kept in the desiccator. Figure 2. 22c and d shows the laser microscope and FE-SEM image of agar gel treated with IL keeping in a desiccator for 3 h and kept in vacuum at 60 °C for 24 h subjected to immersion in IL adjusting water concentration to 30 mol %, respectively.

Results showed that the surface morphology of agar gel was not changed (Figure 2. 22c), when it was kept in vacuum condition after subjected to IL treatment as compared to agar gel only keeping in desiccators for 3 h (Figure 2. 22b). More interesting was the surface morphology could be clearly observed under FE-SEM (Figure 2. 22d) at 5 kV accelerating voltage when the agar gel was treated with IL. Thus we could notice that surface morphology of agar gel remained intact using IL when the water concentration was adjusted to 30 mol %. Therefore, in the next step it is interesting to examine the maximum water concentration upto which the agar gel morphology can be maintained in FE-SEM chamber.

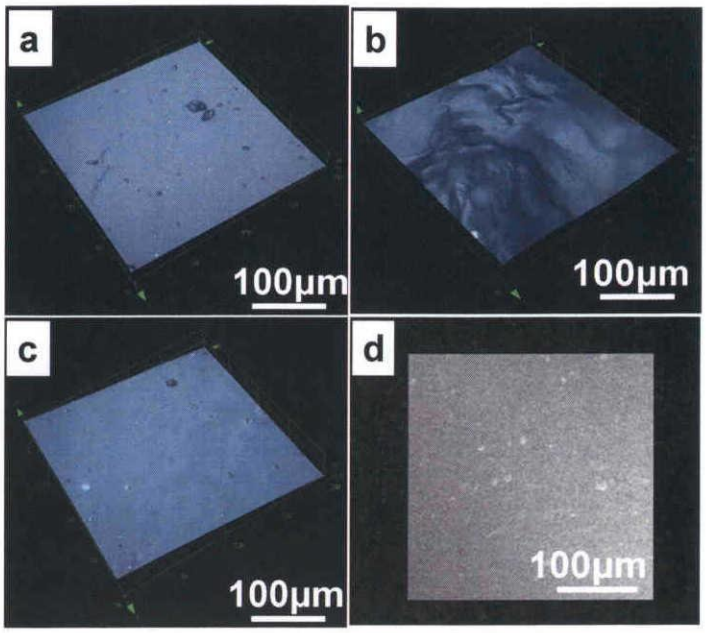

Figure. 2. 22. Laser microscope images of agar gel (a) as-prepared, (b) after keeping in desiccator for 3 h, (c) treated with IL and kept in a desiccator for 3 h + under vacuum at 60 °C for 24 h, and, (d) FE-SEM image of agar gel treated with IL and kept in a desiccator for 3 h + under vacuum at 60 °C for 24 h. The accelerating voltage for FE-SEM observation was 5.0 kV.

2. 3. 8. FE-SEM observation of agar gel in different IL / water concentrations.

Figure 2. 23 shows comparison of FE-SEM images of agar gel in IL with water concentrations gradually changed from 15 to 95 mol %. It can be seen from Figure 2. 23 that the exact morphology of agar gel could be observed for 15, 30 and 60 mol % water concentrations of agar gel with IL (see in Figure 2. 23a-c). Surprisingly, above 80 mol % water concentrations, the morphology of agar gel was changed (see in Figure 2. 23d and e). For 80 mol % water concentration sample, though there was no wrinkle caused by

removing of water within agar gel, large grains were observed. For 95 mol % water concentration sample, the surface of agar gel was dried up completely similar to Figure 2. 22b that was kept in desiccator for 3 h. From these findings it can be concluded that the morphology of agar gel could not be maintained above 80 mol % water concentrations.

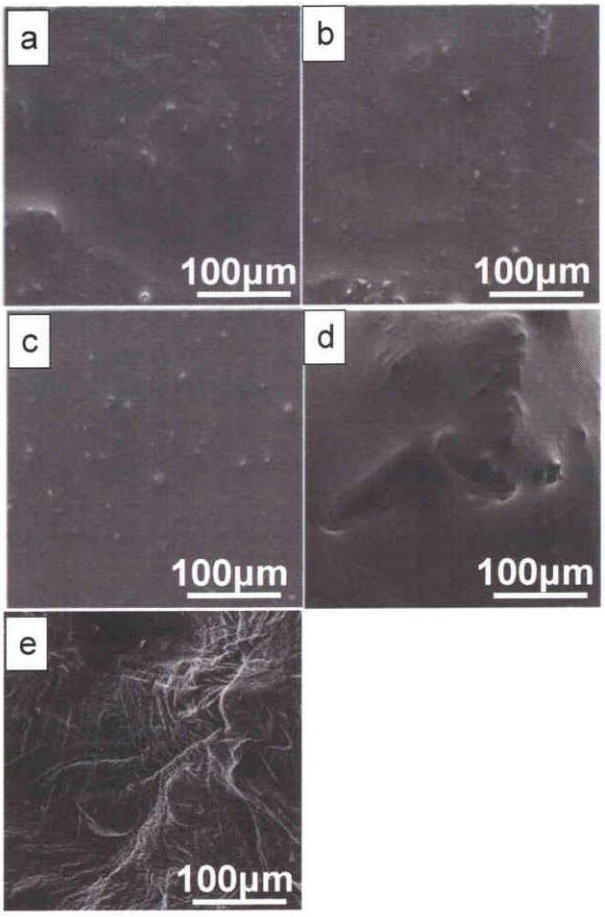

Figure. 2. 23. Comparison of FE-SEM images of agar gel in IL with (a) 15, (b) 30, (c) 60, (d) 80 and (e) 95 mol % water concentration. The accelerating voltage for FE-SEM observation was 5.0 kV.

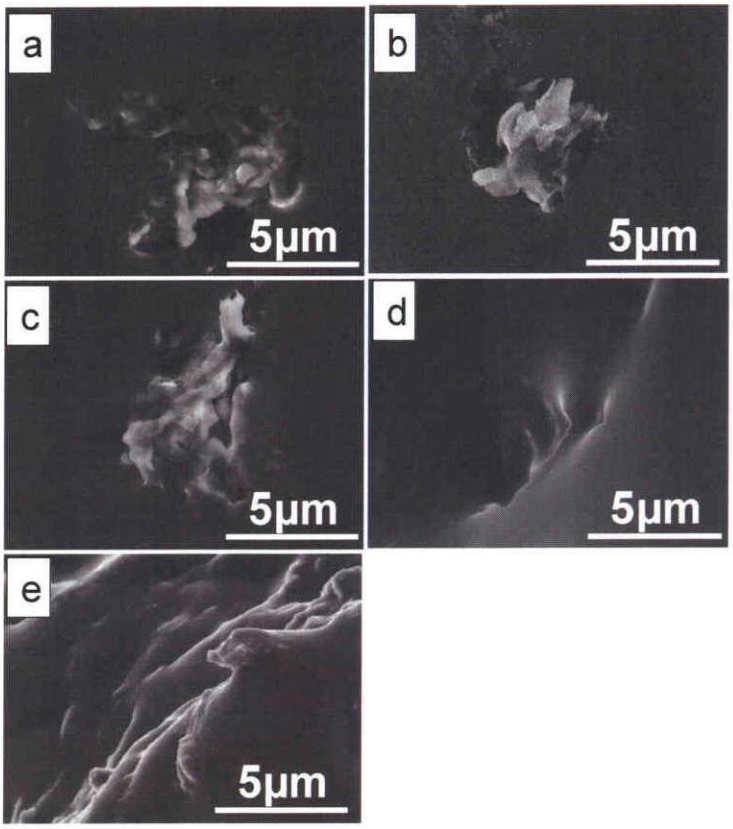

Figure. 2. 24. High magnification FE-SEM images of agar gel in IL with (a) 15, (b) 30, (c) 60, (d) 80 and (e) 95 mol % water concentration. The accelerating voltage for FE-SEM observation was 5.0 kV.

Figure 2. 24 shows high magnification images of fine morphology of agar gel in different IL concentrations. Each image was magnified in the projected part of agar gel. Up to 60 mol % water concentrations, clear images of agar gel particles were observed. On the other hand, above 80 mol % water concentrations, altogether different morphology of agar gel was observed as compared to Figure 2. 24a-c.

Table 2. 4 shows an examination of size retention of agar gel subjected to IL such that water concentration gradually changed from 15 to 95 mol % (Figure 2. 25). Results showed that upto 30 mol %, agar gel retained its size above 98 %. For 60 mol % water concentration, size retention was 89.2 %. Therefore, it is considered that morphology of inside of agar gel was partially changed though surface morphology of agar gel was maintained. Above 80 % water concentration, there was significant change in agar gel morphology as well as size as shown in Table 2. 4 and Figure 2. 24d and e.

Table 2. 4. Size retention of the agar gel in different water concentration keeping in a desiccator for 3 h + under vacuum condition at 60 °C for 24 h.

Concentration (mol % water)	Size retention (%)
15	98.9
30	98.6
60	89.2
80	57.9
95	30.9

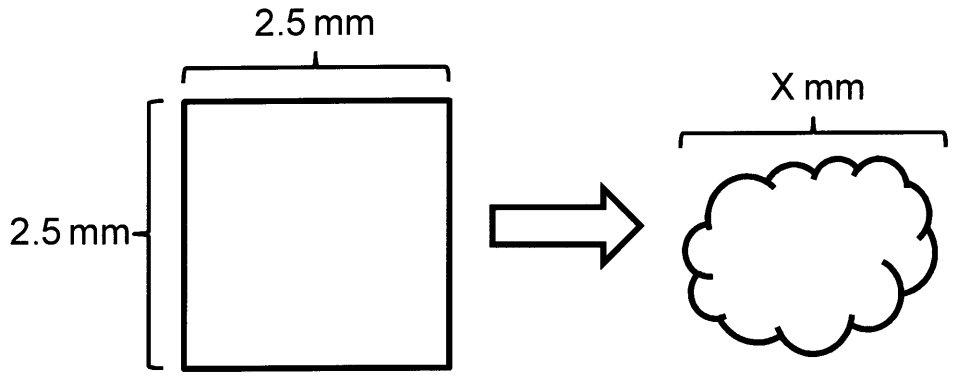

Figure. 2. 25. Size measurement of the agar gel after keeping in a desiccator for 3 h + under a vacuum at 60 °C for 24 h.

From Figure 2. 17, it is considered that IL take water molecules within agar gel due to its binding ability to form $BF_4^- \cdots HOH \cdots BF_4^-$ [21]. For 15 and 30 mol % water concentrations, it is considered that IL had enough water molecules to bind within agar gel. It has been reported that IL displace the water molecules within wet materials [18]. Then, after removal of the water molecules within agar gel by IL, it is considered that IL displaced the water molecules within agar gel. However, for 80 and 95 mol % water concentrations, amount of IL was not enough to bind the water molecules within agar gel. Hence, the residual water molecules within agar gel easily evaporate under vacuum condition leading to size contraction (see in Table 2. 4). Furthermore, for 60 mol % water concentrations, it is considered that IL could not bind with all the water molecules within agar gel, however water molecules within outer part of agar gel were taken up by IL. Then, small amount of water was evaporated under vacuum and size of agar gel was little changed. From the above results, it is considered that IL can have enough water molecules to bind within agar gel and

displace the position of water molecules within agar gel when only weak hydrogen bond exist in mixture of IL and water at RT such as 15 and 30 mol % water concentrations. Present study gave an idea on optimum condition for wet agar gel or any gel materials to be observed under electron microscope in vacuum condition. This unique behavior of water molecules in IL under sample preparation for FE-SEM observation can have important implications on the observation of the agar gel or any other material under wet condition using various electron microscopes in vacuum condition.

2. 3. 9. Morphological observation of agar gel in paste condition.

Figure 2. 26a-d shows optical microscope, laser microscope and FE-SEM image of agar gel in paste condition. Figure 2. 26a and b shows optical microscope image of as-prepared agar gel in paste condition before and after IL treatment, respectively.

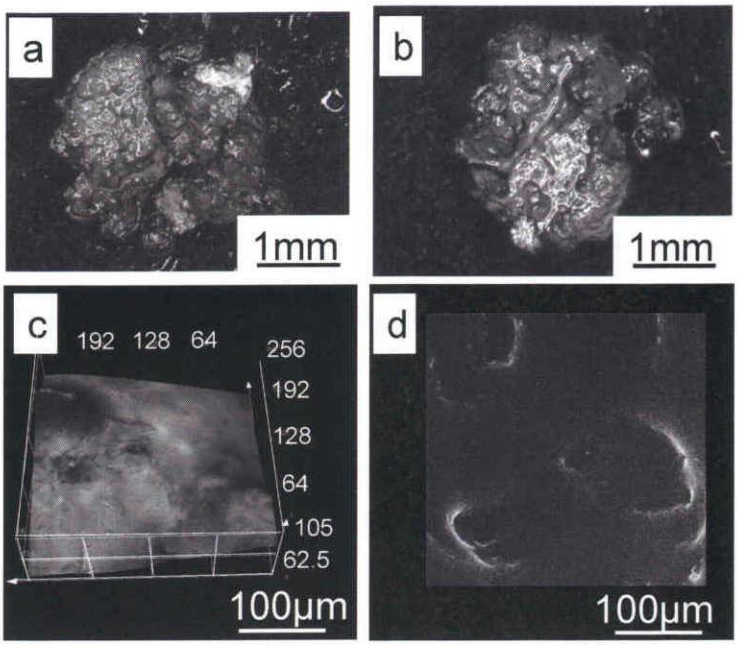

Figure. 2. 26. Optical microscope image of agar gel in paste condition (Water content in agar gel: 89.67 wt %) (a) before and (b) after IL treatment. Comparison of agar gel in paste condition using (c) laser microscope before IL treatment and (d) FE-SEM after IL treatment. The accelerating voltage for FE-SEM observation was 5.0 kV.

For low magnification image of agar gel, the morphology could be maintained despite treated with IL. It should be noted here that agar gel in paste condition was liquid-like therefore it was difficult to observe the same region. Figure 2. 26c and d shows laser microscope image of agar gel before IL treatment and FE-SEM image after IL treatment, respectively. Results showed that the morphology of agar gel in paste condition was stable under FE-SEM condition even if large amount of water was present (Figure 2. 26d). We could observe below 200 μm size agar powders which were not completely swelled by water in the water and agar mixture. The morphology of Figure 2. 26c and d are similar

though some of agar powders displaced their positions due to liquid-like condition. Although sample was exposed to high vacuum in FE-SEM chamber, the morphology of agar gel in paste condition was observed without drying of liquid phase. The sample did not show any charging and remained stable at an accelerating voltage of 5.0 kV. These results showed that IL behaved as a conducting coating to the wet agar gel even if the sample contains large amount of water.

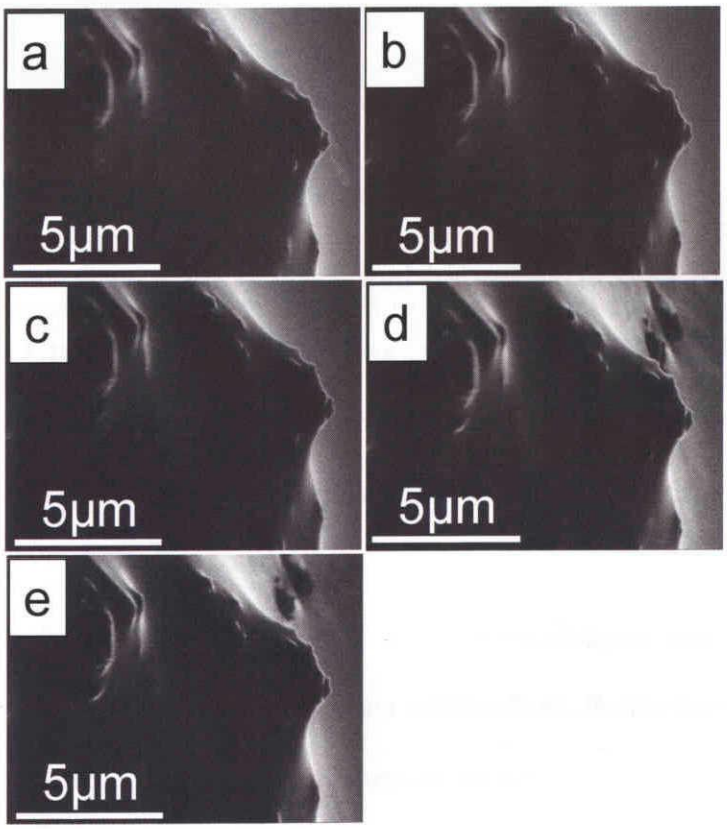

Figure. 2. 27. FE-SEM images of agar gel in paste condition after treatment with IL diluted by ethanol (a) just after sample preparation, (b)15, (c) 30, (d) 45 and (e) 60 min. (Accelerating voltage, 5.0 kV).

For better understanding of the observation mechanism under FE-SEM, a fine structure of the same sample in high magnification (prominent point of right area of Figure 2. 26d) with respect to different time is shown in Figure 2. 27. We choose this prominent area in order to easily understand the change in the morphology.

From Figure 2. 27a-e we can see that, there were no significant differences among the images during 1 h in vacuum condition, and the fine structure of agar gel could be observed clearly below 5 μm in magnification.

2. 3. 10. Morphological observation of agar gel in soft solidification condition.

Figure 2. 28 shows optical microscope, laser microscope and FE-SEM image of agar gel in soft solidification condition. Figure 2. 28a and b shows optical microscope image of agar gel before and after IL treatment, respectively. Results showed that the morphology of agar gel in soft solidification condition could be maintained (at low magnification) despite treated with IL solution. Figure 2. 28c shows laser microscope image of agar gel that was taken in normal atmospheric condition. Sample preparation for laser microscope was same as that of Figure 2. 26c.

Figure 2. 28d shows the FE-SEM image of agar gel taken at an accelerating voltage of 5.0 kV. Similar to paste condition, morphology of agar gel in soft solidification condition did not show any significant difference in FE-SEM and laser microscope. The rising particles of micron-scale ordered structure were clearly observed at surface of agar powders which were swelled by water. Moreover, it was observed that agar powders in soft

solidification condition were more swelled than paste condition as seen from the FE-SEM images (Figure 2. 26d and 2. 28d).

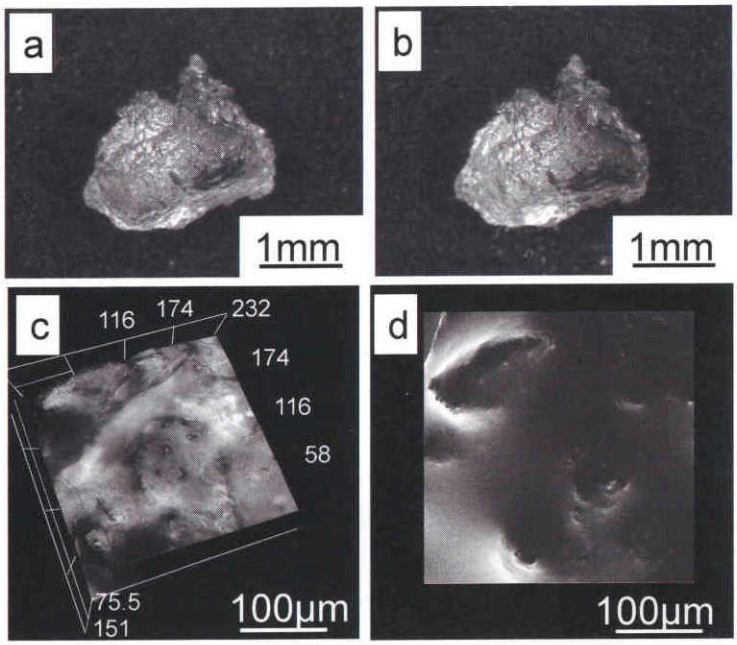

Figure. 2. 28. Optical microscope image of agar gel in soft solidification condition (Water content in agar gel: 84.35 wt %) (a) before and (b) after IL treatment. Comparison of agar gel in soft solidification condition using (c) laser microscope before IL treatment and (d) FE-SEM after IL treatment. The accelerating voltage for SEM observation was 5.0 kV.

In order to understand any change in the morphology, high magnification images (prominent point of left upper area of Figure 2. 28d) were taken at different time intervals and are shown in Figure 2. 29. Morphology of large swelling was observed for most of the swelled parts of agar powders. In comparison with paste condition, there was large number of grains below 1 μm in size. From Figure 2. 29a-e, we could see that there were no

significant changes among the morphologies for different time duration and the observation was similar to that of paste condition as described in section 2. 3. 9. Thus from the FE-SEM image taken for 60 min duration in vacuum chamber as shown in Figure 2. 27 and Figure 2. 29 indicate that the morphology of agar gel remained intact for different swelling conditions (different water content agar gel) when they are treated with hydrophilic ionic liquid. This indicates that samples were not dried during the FE-SEM observation.

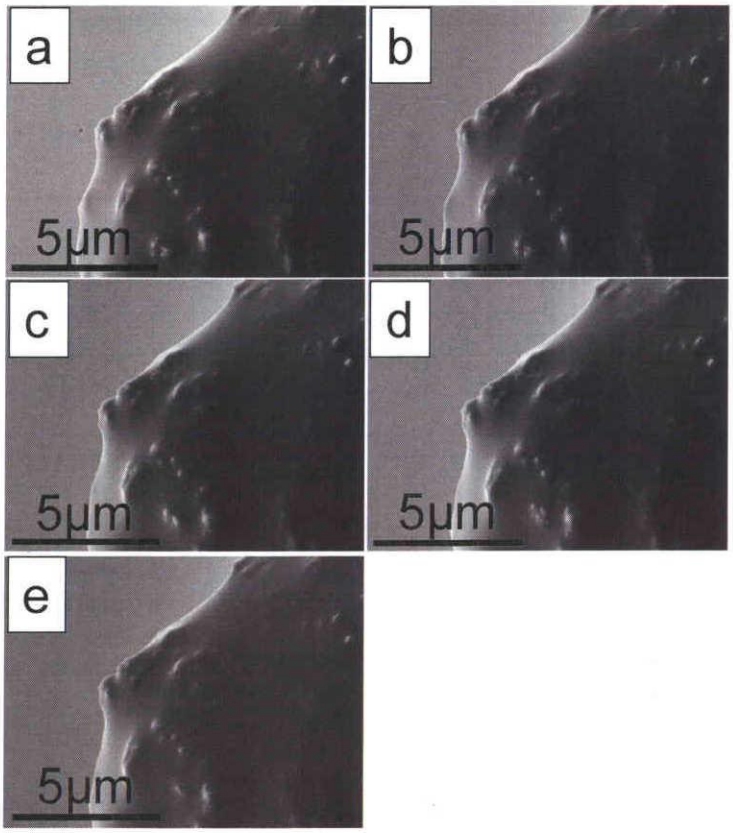

Figure. 2. 29. FE-SEM images of agar gel in soft solidification condition after treatment with IL diluted by ethanol (a) just after sample preparation, (b)15, (c) 30, (d) 45 and (e) 60 min (Accelerating voltage, 5.0 kV).

2. 3. 11. Line and area analysis from FE-SEM images of agar gel in paste condition.

Paste condition of agar gel was chosen for line and area analysis of FE-SEM images because the sample can easily change the morphology and its swelling condition due to more water content. In an effort to clarify the changes in morphology under FE-SEM chamber, magnification images were analyzed by using analysis software similar to below studies.

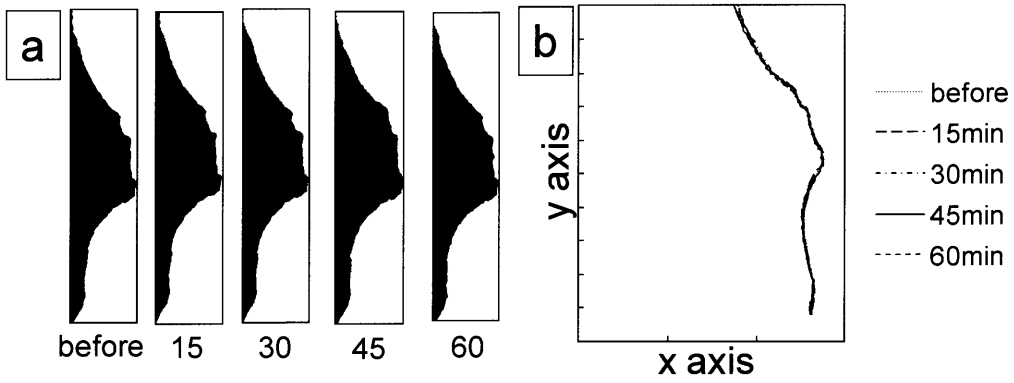

Figure. 2. 30. Comparison of (a) area of FE-SEM image and (b) its outline image of agar gel in paste condition treated with IL diluted by ethanol with respect to time interval as analyzed by the software. X and Y axis are derived from image binarization using analysis software.

Figure 2. 30a and b shows FE-SEM image and its outline image of agar gel in paste condition treated with IL diluted by ethanol at different time intervals, respectively. Differential ratio of images for outline and area for 15 to 60 min to that of original image taken just after sample preparation was calculated and is shown in Table 2. 5. We can see from Table 1 that outline aspect, and area did not show any significant change. Thus from

Figure 2. 30 and Table 2. 5, it can be concluded that there was no significant difference in the morphology of agar gel up to 1 h in vacuum chamber (different ratio: less than 1 %). Therefore it can be concluded that exact morphology of agar gel are able to be observed regardless of swelled conditions.

Table 2. 5. Differential ratio of outline and area for 15 to 60 min as compared to that of original image taken just after sample preparation.

Time (min)	Differential ratio (%)	
	Outline	Area
0	-	-
15	0.91	0.02
35	0.88	0.18
45	0.06	0.04
60	0.30	0.70

2. 3. 12. Behavior of water within agar gel in paste condition.

In order to understand the FE-SEM observation mechanism of agar gel using IL, the behavior of water within agar gel was measured by DSC. Figure 2. 31a shows melting and volatilization endotherms of agar gel in paste condition without any treatment. Endothermic melting and volatilization peaks around 20 and 110 °C of water could be observed, respectively. DSC curve of agar gel treated with IL and kept in desiccator for 2 h is shown in Figure 2. 31b. The glass transition endotherm of IL was observed around at -80 to -70 °C and the result is similar to previous report [36,41]. Although the glass transition of IL was

observed at a fixed temperature, surprisingly, the endothermic melting and volatilization peaks of water could not be clearly observed as compared to Figure 2. 31a. This indicates that the endothermic melting and volatilization peaks of water were disappeared when agar gel was treated by IL and kept in a desiccator for 2 h. Figure 2. 31c shows DSC curve of agar gel treated with IL and kept in desiccator for 2 h + under vacuum at 60 °C for 24 h. The endothermic melting peak of IL was observed similar to that of Figure 2. 31b and there was no endothermic melting and volatilization peaks of water. Generally, it is considered that water is vaporized during the vacuum. However, it is interesting to note that endothermic peak of water was disappeared even after keeping in desiccator for 2 h (Figure 2. 31b).

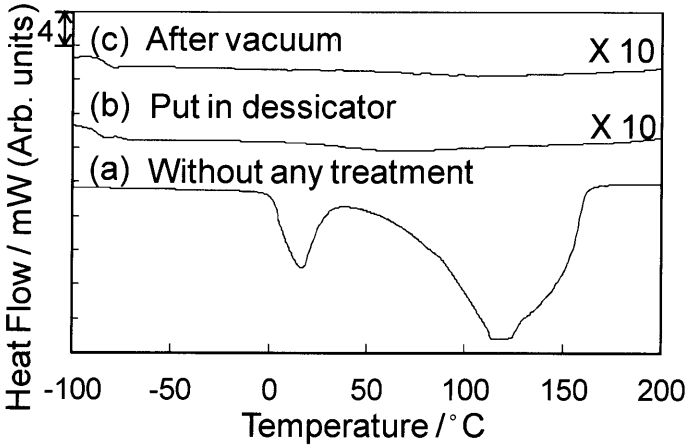

Figure. 2. 31. DSC curves of agar gel in paste condition (a) as prepared (b) treated with IL and kept in desiccator for 2 h and (c) treated with IL and kept in desiccator for 2 h + under vacuum at 60 °C for 24 h.

2. 3. 13. Behavior of water within agar gel in soft solidification condition.

Figure 2. 32a shows melting and volatilization endotherms of agar gel in soft solidification condition without any treatment as observed in DSC. The endothermic melting and volatilization peaks of water could be clearly observed around 10 and 100 °C, respectively. DSC curve of agar gel with IL treatment and kept in desiccator for 2 h is shown in Figure 2. 32b. The small glass transition of IL was also observed around -80 to -70 °C. Figure 2. 32c shows DSC curve of agar gel treated with IL and kept in desiccator for 2 h + under vacuum at 60 °C for 24 h. The glass transition endotherm of IL was observed similar to that of Figure 2. 31b. There was almost no difference in the melting and volatilization endotherms for both types of agar gel (Figure 2. 31c and 2. 32c).

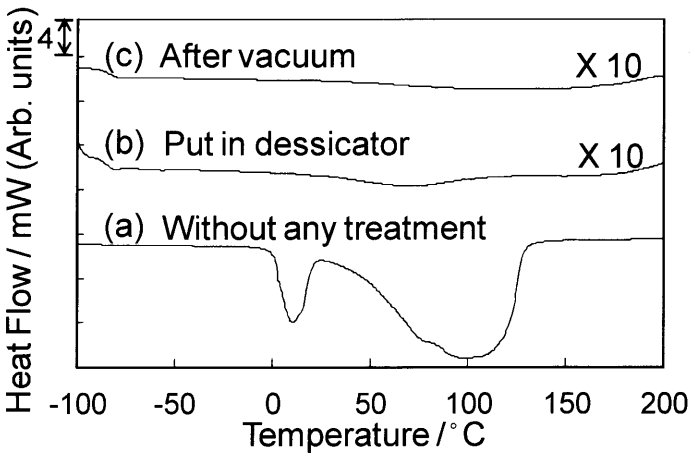

Figure. 2. 32. DSC curves of agar gel in soft solidification condition (a) as prepared (b) treated with IL and kept in desiccator for 2 h and (c) treated with IL and kept in desiccator for 2 h + under vacuum at 60 °C for 24 h.

From DSC results, as explained in section 2. 3. 12 and 2. 3. 13, we noticed that water seems to be no existing within agar gel after IL treatment and keeping in desiccator

for 2 h. However, in this study, the agar gel treated with IL was adjusted to the total water concentration to 30 mol %. For 30 mol % water concentration of the mixture of IL and water, the weak hydrogen bond [BF_4^- ··· H-O-H ··· BF_4^-] was observed by Raman spectroscopy at room temperature as below (see in chapter 2. 3. 4). Furthermore, it is reported that the formation of weak hydrogen bond between water and IL was not completely dissociated even at 190 °C, though water molecule gradually dissociate during heating [35]. From our results, it was clarified that water molecule within agar gel is completely taken by IL when water concentration of mixture is 15 and 30 mol % (see in chapter 2. 3. 5). Therefore, from the above discussion it can be expected that water molecule within agar gel was also taken up completely by IL at 30 mol % water concentration during IL treatment and keeping in desiccator for 2 h due to IL binding ability with water molecules. This helps agar gel to maintain its morphology by displacement of IL and water molecule. In order to understand why volatilization endotherms peak of water after keeping in the desiccator disappeared, behavior of water during the mixture of IL and water needs to be examined.

2. 3. 14. Behavior of water in the mixture of IL and water.

Figure 2. 33a-c shows melting and volatilization endotherms of water and IL mixture (15-45 mol %) in different water concentrations and kept in desiccator for 2 h. For 15 and 30 mol % water concentration of IL and water mixtures after keeping in desiccator for 2 h, the volatilization endotherms of water were not clearly observed though small broad peaks were obtained, respectively (Figure 2. 33a and b). Thus, the volatilization endotherms

peak of water was disappeared similar to agar gel treated with IL and kept in desiccator for 2h (Figure 2. 31b and 2. 32b). Surprisingly, for 45 mol % water concentration sample after keeping in desiccator for 2 h, the volatilization endotherms of water was clearly observed around 80 °C. However, this volatilization endotherm of water disappeared when the sample was subsequently kept in vacuum condition at 60 °C, 24 h (Figure 2. 33d). After vacuum at 60 °C for 24 h, the small volatilization endotherm peak of water was observed in the range of 30 to 200 °C similar to 15 and 30 mol % water concentrations after keeping in desiccator for 2 h. From our results, it is clear that both weak hydrogen bond and normal hydrogen bond exists for 45 mol % water concentration at RT as observed by Raman spectroscopy (see in chapter 2. 3. 4).

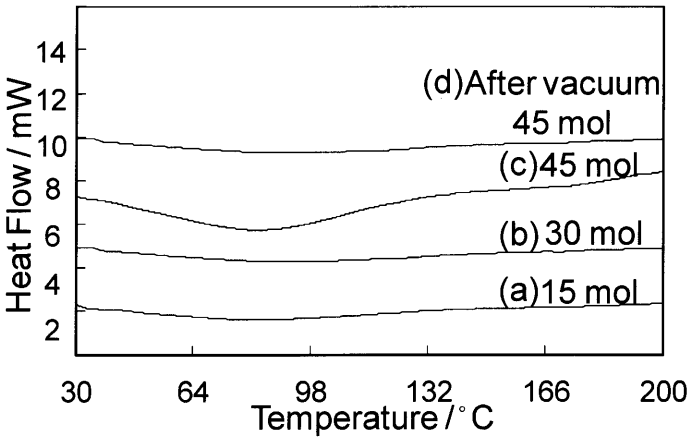

Figure. 2. 33. DSC curves of water and IL mixture in (a) 15, (b) 30, (c) 45 mol % water concentrations after keeping in desiccator for 2 h and (d) 45 mol % water concentrations after keeping in desiccator for 2 h + under vacuum at 60 °C for 24 h.

Furthermore, the small amount of weak hydrogen bond exist in water and IL mixture for 15 to 95 mol % water concentrations even after keeping in vacuum for 24 h.

Therefore, it is consider that the normal hydrogen bond was completely evaporated under vacuum at 60 °C for 24 h, and only weak hydrogen bond exists without evaporation due to IL binding ability. Hence, for 45 mol % water concentration after vacuum, only weak hydrogen bond exist in IL and water mixtures.

Moreno et al reported that around 20 mol % water concentrations, the cation and anion parts of IL are selectively coordinated by individual water molecules, however their ionic network is largely unperturbed. At high water concentrations, the ionic network is somewhat disrupted or swollen in a nonspecific way by the water clusters [28]. At around 20 mol % water concentrations, the transition of water monomers and dimers to larger aggregates increased. From the present experimental study, it is speculated that large water clusters grew over 30 mol % water concentrations.

From above results, it is considered that IL exists with water molecule such as BF_4^- $\cdots$H-O-H$\cdots$$BF_4^-$ formation within agar gel due to IL binding ability when IL displace with water within agar gel. In order to understand the existence of IL which displaced with water within agar gel, we need to measure the volume change of agar gel after IL treatment.

2. 3. 15. Volume change of agar gel after IL treatment.

Table 2. 6 shows comparative study of shrinkage volume of agar gel in soft solidification condition before and after IL treatment. Agar gel in paste condition could not be measured due to high liquid content. Volume of water occupied within agar gel without any treatment was calculated by subtracting from the residual weight of agar gel after vacuum dryer. On the other hand, volume of displaced IL (including water molecule bonded

with IL) was calculated using residual weight of agar gel after subtracting from the residual weight of agar gel after vacuum. In this study, total water concentration of IL and water within agar gel was adjusted to 30 mol % water concentration, and hence IL and water exits in agar gel contain 30 mol % water concentrations. Thus, volume of water and IL was calculated using density of aqueous IL in 30 mol % water concentration [42].

Table 2. 6. Volume shrinkage of agar gel in soft solidification condition treated with IL and without any treatment.

	a. volume of water within agar gel[1] (ml)	b. residual weight after vacuum[2] (mg)	c. volume of water and IL within agar gel[3] (ml)	d. volume shrinkage of agar gel[4] (%)	e. linear shrinkage of agar gel[5] (%)
IL treatment	8.43×10^{-3}	11.13	8.31×10^{-3}	1.54	0.52
Without any treatment	8.43×10^{-3}	1.57	0	0	0

1) $a = (10 - 1.57) / 10^{3}$ (weight of agar gel without any treatment: 10 mg)

2) Average of residual weight after vacuum at 5 times (Table 2. 7)

3) $c = (b - 1.57) / 1.15$* (*: density of aqueous IL in 30 mol % water concentration (g / ml). Value taken from Q. G. Zhang, F. Xue, J. Tong, W. Guan, and B. Wang, Journal of Solution Chemistry, 2005, 35, 297-309.

4) $d = (1 - c / a) \times 100$

5) $e = d^{1/3}$

Thus, volume shrinkage of agar gel after IL treatment was found to be 1.54 %. Moreover, coefficient of linear contraction of agar gel was only 0.52 %. This indicates that

the fine morphology of agar gel can be observed within 1.0 % difference. From these results, it is considered that anion part of IL and water molecule form a specific bond such as BF_4^- ···H-O-H···BF_4^- and exist within agar gel by replacing the water within it.

Table 2. 7. Average of residual weight of agar gel after vacuum condition.

Condition	Residual weight (mg)
IL treatment	11.12
	11.15
	11.13
	11.11
	11.14
Without any treatment	1.56
	1.58
	1.56
	1.57
	1.58

2. 4. Conclusions

1. The fine morphology of an agar gel (polymer gel) could be successfully observed using a typical IL by FE-SEM and there was no interaction between the agar, IL and ethanol. Based on the result of the in-situ Raman spectroscopy, the displacement rate of agar gel using a large amount of water was slower than using a small amount of water. It is expected that Raman observations of agar gel will provide information for observing samples

containing water. From the results, it is concluded that the exact morphology of agar gel can be observed when IL penetrate into agar gel completely. We consider that the interaction of the IL and water-containing gel was more complicated and the interaction of IL with water must be taken into consideration when observed under the SEM. Furthermore, it was found that the ethanol had no effect on the interaction of the IL, water and agar by Raman spectra and from the point of view of the SEM observations compared to the laser microscope. This observation is useful in order to realize the interaction of the water-containing sample, IL and ethanol.

2. The mechanism of FE-SEM observation of agar gel in presence of IL was examined. Results showed that water molecules within agar gel were taken by IL when samples were kept in a desiccator for 3 h as a sample preparation condition for FE-SEM observation. IL and water exist as BF_4^- ...HOH...BF_4^- via weak hydrogen bond even in vacuum condition due to its strong bonding ability. It is suggested that the water molecules within agar gel were displaced by IL owing to the similar weak hydrogen bond formation. However, when there is not enough IL, water molecules are not completely taken up by IL. Therefore, it could be understand that morphology of agar gel was changed due to easy evaporation of residual water within agar gel. From these results, it was found that the exact morphology of agar gel or any gel materials could be obtained by adjusting water concentrations in the range of 15-30 mol % in the samples.

3. The morphology of water containing agar gel in different swelling conditions and water contents could be observed by FE-SEM. Exact morphology of swelled agar gel could be clearly observed with less than 1 % difference even in a paste condition with large

amounts of liquid phase. Surface morphology was not changed even if the sample was kept under vacuum at 60 °C for 24 h and in FE-SEM chamber. From DSC and volume measurement of agar gel, it was found that IL and water exist in agar gel when total water concentration of IL and agar gel mixture was 30 mol %. In such case, anion part of IL and water form weak hydrogen bond such as $BF_4^-\cdots H\text{-}O\text{-}H\cdots BF_4^-$ and this bonding is reported to be exists even at 200 °C. At first, IL takes water molecule within agar gel due to its binding ability with water is quite strong (15 and 30 mol % water concentrations). Then, bonded IL and water molecule exist in agar gel instead of free water within agar gel, and maintain the wet gel morphology.

These electron microscope observation will be very important in understanding the exact morphology of water-containing materials. Thus, the agar gel or any other material under wet condition can be observed without drying using electron microscopy based on this anomalous mechanism. In addition, the approach on microscopic observation of wet agar gel in different swelling condition opened up a new methodology to observe hydrated samples in FE-SEM.

References

[1] K. Kishita, H. Sakai, H. Tanaka, H. Saka, K. Kuroda, M. Sakamoto, A. Watabe, T. Kamino, J. Electron. Microsc. 58 (2009) 331-339.

[2] K. Yoshida, M. Makihara, N. Tanaka, S. Aoyagi, E. Nishibori, M. Sakata, E.D. Boyes, P.L. Gai, Microsc. Microanal. 15 (2010) 596-597.

[3] P. Wasserscheid, C.M. Gordon, C. Hilgers, M.J. Muldoon, I.R. Dunkin, Chem. Commun. 111 (2001)1186-1187.

[4] J.F. Wishart, E.W. Castner, J. Phys. Chem. B. 111 (2007) 4639-4640.

[5] S. Seki, Y. Ohno, Y. Kobayashi et al, J. Electrochem. Soc. 154 (2007) A173-A177.

[6] F. Golgovici, A. Cojocaru, L. Anicai, T. Visan, Mater. Chem. Phys. 126 (2011) 700-706.

[7] J. Yang, Y. Sang, F. Chen, M. Zhong, Mater. Chem. Phys. 128 (2011) 19-23.

[8] K. Huang, J. Xia, M. Li, J. Lian, X. Yang, G. Lin, Carbohyd. Polym. 83 (2011) 1631-1635.

[9] D.G. Stevenson, A. Biswas, J. Jane, G.E. Inglett, Carbohyd. Polym. 67 (2007) 21-31.

[10] C. Tsioptsias, C. Panayiotou, Carbohyd. Polym. 74 (2008) 99-105.

[11] J. Kadokawa, M. Murakami, A. Takegawa, Y. Kaneko, Carbohyd. Polym. 75 (2009) 180-183.

[12] O. Aaltonen, O. Jauhiainen, Carbohyd. Polym. 75 (2009) 125-129.

[13] X. Hu, K. Hu, L. Zeng, M. Zhao, H. Huang, Carbohyd. Polym. 82 (2010) 62-68.

[14] S. Kuwabata, A. Kongkanand, D. Oyamatsu, T. Torimoto, Chem. Lett. 35 (2006) 600-601.

[15] T. Torimoto, K. Okazaki, T. Kiyama, K. Hirahara, N. Tanaka, S. Kuwabata, Appl. Phys. Lett. 89 (2006) 243117.

[16] P. Roy, T. Dey, P. Schmuki, Electrochem. Solid-State. Lett. 13 (2010) E11-E13.

[17] S. Kuwabata, T. Tsuda, T. Torimoto, J. Phys. Chem. Lett. 1 (2010) 3177-3188.

[18] S. Arimoto, M. Sugimura, H. Kageyama, T. Torimoto, S. Kuwabata, Electrochim. Acta. 53 (2008) 6228-6234.

[19] K. Kawai, K. Kaneko, H. Kawakami, T. Yonezawa, Langmuir. 27 (2011) 9671-9675.

[20] S.G. Kazarian, B.J. Briscoe, T. Welton, Chem. Commun. (2000) 2047-2048.

[21] L. Cammarata, S.G. Kazarian, P.A. Salter, T. Welton, Phys. Chem. Chem. Phys. 3 (2001) 5192-5200.

[22] S.N.V.K. Aki, J. Brennecke, A. Samanta, Chem. Commun. (2001) 413-414.

[23] C.G. Hanke, R.M. Lynden-Bell, J. Phys. Chem. B. 107 (2003) 10873-10878.

[24] H. Katayanagi, K. Nishikawa, H. Shimozaki, K. Miki, P. Westh, Y. Koga, J. Phys. Chem. B. 108 (2004) 19451-19457.

[25] X. Wu, Z. Liu, S. Huang, W. Wang, Phys. Chem. Chem. Phys. 7 (2005) 2771-2779.

[26] S. Saha, H. Hamaguchi, J. Phys. Chem. B. 110 (2006) 2777-2781.

[27] W. Jiang, Y. Wang, G.A. Voth, J. Phys. Chem. B. 111 (2007) 4812-4818.

[28] M. Moreno, F. Castiglione, A. Mele, J. Phys. Chem. B. 112 (2008) 7826-7836.

[29] N.M. Vaghela, N.V. Sastry, V.K. Aswal, Colloid. Polym. Sci. 289 (2011) 309-322.

[30] C. Schröder, T. Rudas, G. Neumayr, S. Benkner, O. Steinhauser, J. Chem. Phys. 127 (2007) 234503.

[31] H.C. Chang, J.C. Jiang, Y.C. Liou, C.H. Hung, T.Y. Lai, S.H. Lin, J. Chem. Phys. 129 (2008) 044506.

[32] B. Sun, Q. Jin, L. Tan, P. Wu, and F. Yan, J. Phys. Chem. B. 112 (2008) 14251-14259.

[33] Y. Jeon, J. Sung, D. Kim, C. Seo, H. Cheong, Y. Ouchi, R. Ozawa, H. Hamaguchi, J. Phys. Chem. B. 112 (2008) 923-928.

[34] H. Abe, Y. Yoshimura, Y. Imai, T. Goto, H. Matsumoto, J. Mol. Liquids. 150 (2009) 16-21.

[35] B. Sun, P. Wu, J. Phys. Chem. B. 114 (2010) 9209-9219.

[36] Y. Yoshimura, H. Kimura, C. Okamoto, T. Miyashita, Y. Imai, H. Abe, J. Chem. Thermodynamics. 43 (2011) 410-412.

[37] S. Shirai, T. Kato, Y. Endo, H. Watanabe, M. Fuji, M. Takahashi, Trans. Mater. Res. Soc. Japan. 34 (2009) 117-120.

[38] Y. Han, S. Kim, H. Kim, J. Park, J. Am. Ceram. Soc. 94 (2011) 2742-2745.

[39] C.D. Munro, K.P. Plucknett, Int. J. Appl. Ceram. Technol. 8 (2011) 597-609.

[40] K. Mizuno, S. Imafuji, T. Ochi, T. Ota, S. Maeda, J. Phys. Chem. B. 104 (2000) 11001-11005.

[41] W. Xu, L.M. Wang, R.A. Nieman, A. Angell, J. Phys. Chem. B 107 (2003) 11749-11756.

[42] Q. Z. Zhang, F. Xue, J. Tong, W. Guan, B. Wang, J. Solution. Chem. 35 (2006) 297-309.

CHAPTER 3

A SIMPLE APPROACH TO OBSERVE NON-CONDUCTIVE HYDRATED MATERIALS WITH FE-SEM: CASE STUDY ON POROUS HYDROXYAPATITE GREEN BODIES

3.1. Introduction

Among the various types of calcium phosphate ceramics, hydroxyapatite [$Ca_{10}(PO_4)_6(OH)_2$, HAp] is a well-known biocompatible material and is naturally found as one of the major components of bone and tooth [1-4]. As-synthesised HAp ceramics show both osteoconductivity and osteoinductivity and directly bonds to living bone through the native apatite phase [5, 6]. However, for enhanced bone integration and mechanical interlocking between implanted devices and the newly grown bone tissues, particular attention must be paid to the processing of the porous HAp body [7].

A variety of methods for fabricating porous HAp bodies have been described in the literature; these include the impregnation of polymeric sponges, gelcasting of foam, extrusion and other automated manufacturing methods [8-11]. Among these methods, gelcasting, which was developed by Janney and co-workers, can be used to fabricate allows obtaining samples with complex shapes and high mechanical strength [12, 13]. This method also has been successfully applied to other ceramics, such as alumina [14-16], silicon

nitride [17], rutile [18], silicon carbide [19, 20], and alumina–zirconia composites [21, 22]. Additionally, following the solidification step, when this method is further combined with foamed suspensions by in situ polymerization, it can be used to form an internally cross-linked network, which that transforms the foam into a gelled body with the ability to bear load [23-26]. The gelled body is then sintered to create the final material, which can be used in various functional applications. Although several researchers have used scanning electron microscope (SEM) to describe the surface morphology and the microstructure of gelcast porous ceramics in either the dried or sintered conditions, there have been no reports that which describes the microstructure of the green body in its hydrated condition immediately following fabrication. This is because the water-containing ceramic materials present certain limitations for SEM observations, which necessitate the use of vacuum conditions in the microscope chamber. However, to establish enhanced processing conditions for ceramics, it is necessary to understand the complex structure of the green body. Thus, it is essential to develop new techniques for microscopic observations of ceramic bodies in the hydrated form.

Recently, room-temperature (RT) ionic liquids (ILs) have attracted significant attention as novel, eco-friendly materials that can be used as solvents in inorganic chemistry, electrochemistry, catalysis, etc [27-29]. These ILs are composed of cations and anions, which exist in a liquid state at RT. Due to their negligible vapour pressure and high conductivity, various studies have also revealed that combinations of ILs with samples can be directly observed in the electron microscope without the addition of a conductive coating [30-32]. Some reports have further suggested that hydrated materials, such as seaweed and

chicken tissue are observable by SEM when mixed with hydrophilic ILs [33, 34]. The author of this study has previously reported that hydrated agar gel can be successfully observed using the hydrophilic IL; additionally, a mechanism was proposed for the field emission scanning electron microscope (FE-SEM) observation of gel-type materials that have not been dried in a vacuum chamber [35-37].

In the present study, with the aid of hydrophilic ionic liquid, we observed the surface morphology of the porous HAp green body in its wet condition and compared the changes in pore structure that occur during drying and after sintering with the aid of hydrophilic ionic liquid. The interaction of water molecules and the IL is studied by Raman spectroscopy. Finally, we propose a general principle for the morphological observation of wet ceramic materials.

3. 2. Materials and methods

A hydroxyapatite (HAp) powder, a dispersant, a monomer and various initiators were used for the gelcasting process. The HAp powder was supplied by Taihei Chem. Co., Japan, with a particle size less than 5 μm. A commercial ammonium salt of polycarboxylate (Seruna D-305) supplied by CHUKYO YUSHI Co., LTD, Japan was used as the dispersant. The organic components (i.e., the epoxy and the hardener) were supplied by CHUKYO YUSHI Co., LTD, Japan, and TETA (Kanto Chemical Co., Japan) was used as the catalyst.

The ionic liquid of choice for analyses was 1-butyl-3-methylimidazolium tetrafluoroborate ((BMIM)(BF_4)) (Kanto Chem. Co., Japan); in all instances, this chemical was dried in a vacuum desiccators at 60 °C for 3 days before use. The chemical structure of

the IL is shown in Figure 3. 1. The water content of the IL was below 128 ppm, as measured by the Karl Fischer titration method.

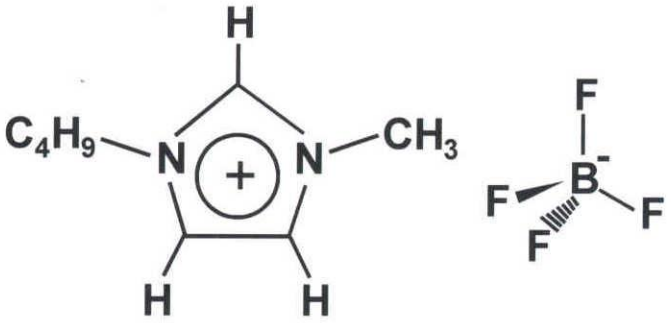

Figure. 3. 1. Chemical structure of the IL used in the present study.

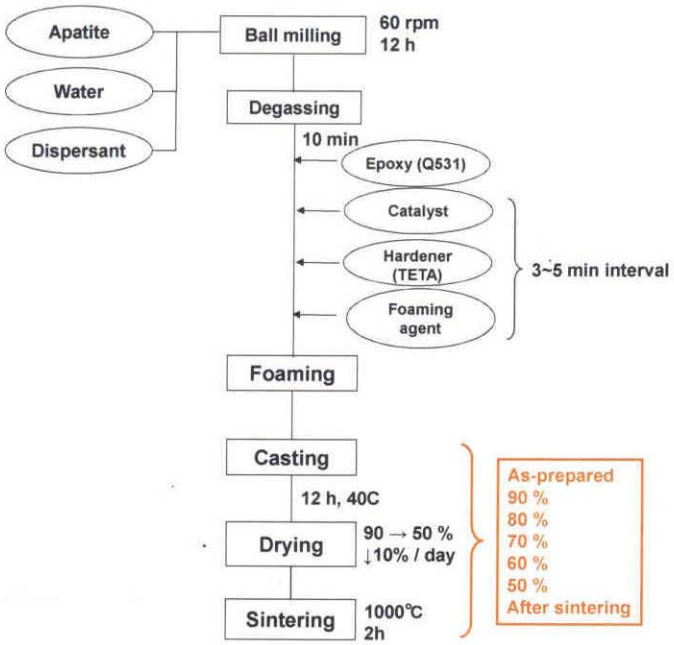

Figure. 3. 2. Schematic representation of the gelcasting process used in the present study.

Figure 3. 2 shows a schematic representation of the gelcasting process used in this investigation. In the first step, a 40-vol.-% slurry was prepared from the HAp powder, water and dispersant by ball milling inside a polyethylene container with zirconia balls for approximately 24 h. The slurry was screen-filtered to remove the zirconia balls and was then degassed for 10 min to remove any trapped air bubbles. The degassed slurry was combined with the epoxy resin, the initiator and the catalyst to initiate the polymerisation process. To incorporate pores into the microstructure, 0.3 g of surfactant (per 100 mL of slurry) were added and mixed with a hand mixer. Finally, the resulting slurry mixture was poured into a rectangular shape mould and was allowed to gel overnight at 40 °C in air. The mould was removed from the freshly gelled body; the specimen was then cut to a size of 5.0 × 5.0 × 5.0 mm^3 around the central region of the rectangular sample. The trimmed specimens were kept in a humidity-controlled drying chamber at 25 °C for 5 days in such a way that the humidity was reduced from 90 to 50 % at a rate of 10% per day.

The water contents of both the as-prepared porous HAp green body and the specimens that had been stored in the humid chamber were measured by Karl Fischer titration. All porous bodies were cut into the same 5.0 × 5.0 × 5.0 mm^3 in size for this measurement.

The as-prepared samples and the samples stored in the humid chamber were both treated with the IL. The IL was prepared by adjusting its water content to 30 mol % (weight amount ratio; water : IL = 1 : 29.3) and was stored in a desiccator for 2 h. All these samples were subsequently maintained in a vacuum dryer for 24 h before being centrifugated for 5 min at 10,000 rpm to remove any excess IL. The microstructures of the IL-treated samples

were observed using field emission scanning electron microscopy (FE-SEM, JEOL Co., Japan) performed at 5 kV. Additionally, the porous HAp bodies were sintered at 1000 °C for 2 h and were then coated with either conventional osmium metal or the IL solution; the surface morphologies of both cases were compared under FE-SEM. The sintering of the porous bodies was carried out at 1000 °C for 2 h in an atmospheric furnace and the rate of heating was maintained at 1 °C/min to avoid thermal cracking.

The X-ray diffraction (XRD) pattern (Ultima 5, Rigaku Co., Japan) of the hydroxyapatite powder was recorded in the 2θ range from 10 to 60° with a scan rate of 1° / min using Cu Kα radiation (λ = 0.1542 nm, 40 kV, 40 mA). Micro-focused X-ray CT analysis (SMX-90CT, Shimadzu Co., Japan) of the porous HAp green bodies was performed to examine the pore morphology with respect to the drying procedure, and the results were compared to the FE-SEM images, which were collected under similar conditions. Each porous HAp green body was cut into a size of $2.0 \times 2.0 \times 0.5$ cm^3 for this measurement.

The size retention of the as-prepared porous HAp green bodies, the samples that were treated in the humid chamber as it was reduced from 80 to 50% relative humidity, and those that were sintered at 1000 °C for 2 h were all measured both before and after the IL treatment. The dimensions of the samples were measured using a ruler as shown in Figure 3. 3. The size retention ratios were calculated ($X \times Y \times Z / 125 \times 100$).

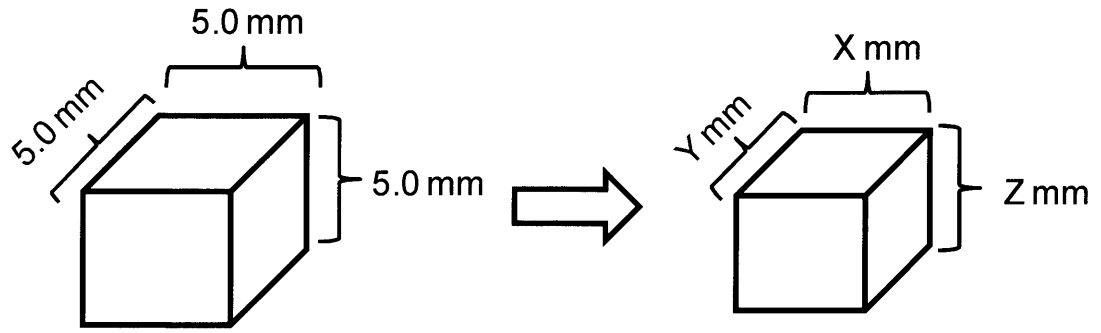

Figure. 3. 3. Size retention measurement of porous green bodies just after removal from the mold and those kept in humidity chamber 80, 50 % and porous body after sintered at 1000 °C for 2 h.

The pore diameters of the green HAp bodies just following removal from the mould and of those maintained in the humid chamber as it was reduced from 90 to 50 % relative humidity were determined from the FE-SEM images. The measurements were taken from an area of 3.0 × 3.0 mm^2 which was imaged with FE-SEM images and the average pore diameters were calculated from the micrographs of these regions. The diameter of each pore was measured according to by X + Y / 2 (Figure 3. 4). For the pore size distribution measurement, aread of 3.0 × 3.0 mm^2 were recorded both by micro-focused X-ray CT and by FE-SEM imaging; the pore diameters were measured for pores in the range of 50 to 700 μm.

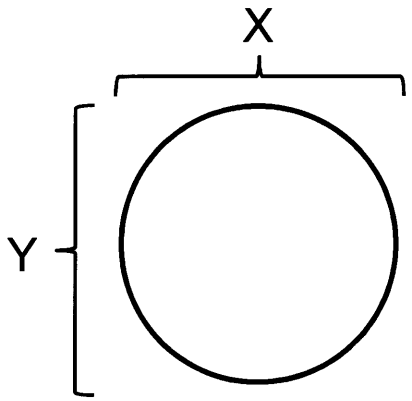

Figure. 3. 4. Pore diameter measurement of porous green bodies just after removal from the mold and those kept in humidity chamber from 90 to 50 %. The pore diameter of porous green body was measured as Figure S2. The pore diameter was calculated (X + Y / 2).

The collected IL solution was characterized by Raman microscopy in order to examine the interaction of IL and hydrated green body [36]. This solution is designated as *[HAp$_{IL}$]* in subsequent discussions. For comparison, raw IL and HAp sample sintered at 1000 °C were also measured. For the Raman measurements, collected IL solution was introduced into a pyrex tube of 5.0 mm φ, 0.8 mm wall thickness, while dried sample was measured directly. The Raman spectra were taken at room temperature by a JASCO NRS-3100 (Nihon bunko Co, Japan) laser Raman spectrophotometer equipped with a single monochromator and a CCD detector in the range of 2800 to 3800 cm^{-1} at the 1.0 mm depth from the pyrex surface and averaged 5 times. The Raman spectrum was taken by 2.5 mW of the 514.5 nm line of an Ar ion laser as the excitation source.

3. 3. Results and discussions

3. 3. 1. Characterization of the as-received HAp powder.

Figures 3. 5a and b show the FE-SEM images and XRD spectrum of the as-received HAp powder, respectively. Agglomerated spherical HAp particles of approximately 5-10 μm in diameter can be seen in Figure 3. 5a; additionally, it can be seen that these grains are composed of approximately 200-400-nm sub-grains (inset Figure 3. 5a). Further inspection of the XRD pattern indicates that the powder contains a pure HAp phase, identified by the corresponding 2θ theta values, as shown in Figure 3. 5b. The HAp powder was subsequently used for the gelcasting process, which was employed to fabricate the porous HAp green body samples.

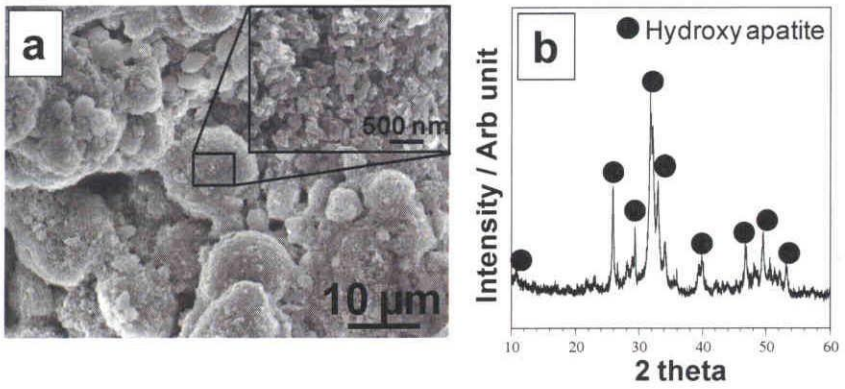

Figure. 3. 5. (a) FE-SEM images of the as-received hydroxyapatite powder, in which the inset shows a high-magnification image, and (b) the corresponding XRD spectrum. All XRD peaks correspond to the structure of hydroxyapatite.

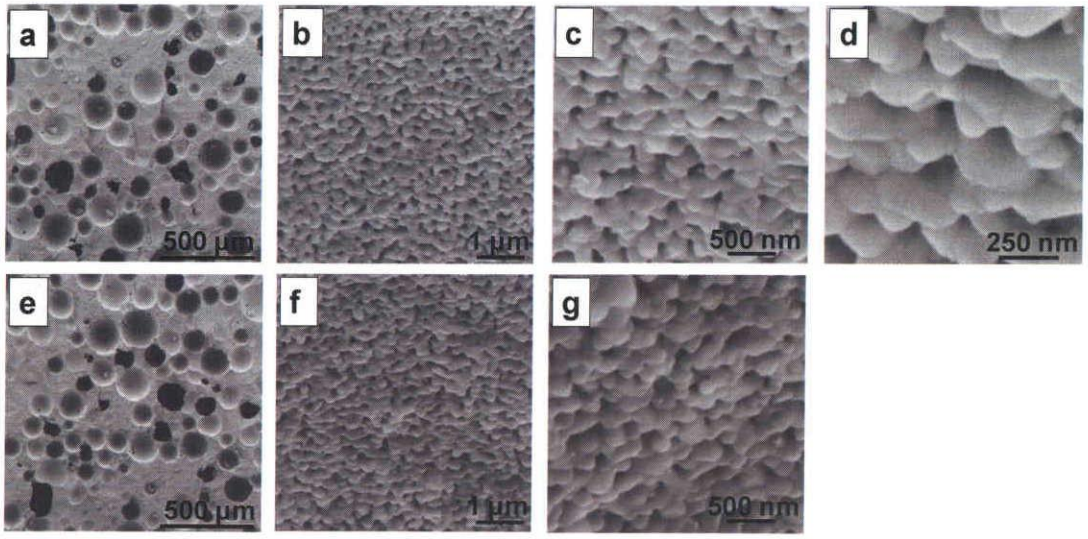

Figure. 3. 6. Comparison of the FE-SEM images of the porous HAp body sintered at 1000°C for 2h, following (a)-(d) osmium coating and (e)-(g) the IL treatment. The surface morphologies appeared to be similar for both the osmium-coated and the IL-treated samples.

3. 3. 2. Observational limitation using IL of sintered porous HAp body.

Figure 3. 6 shows a comparison of the FE-SEM images of the sintered porous HAp body following either an osmium coating treatment (Figure 3. 6a-d) or a separate subjection of the porous HAp body to the IL treatment (Figure 3. 6e-g). It can be seen in the low-magnification image that the sintered sample consists of pores in the range of approximately 100-300 µm in diameter (Figure 3. 6a). The high-magnification image demonstrates that the porous body consists of HAp particles; the particles have bonded to each other creating nanoporosity between them (Figure 3. 6b-d). This result indicates the

presence of neck formation and of partial sintering among the HAp particles, which were treated at 1000 °C. Additionally, there were no identifiable differences between the FE-SEM images of the samples coated with the osmium metal (Figure 3. 6a-d), which is a conventional conductive coating used for ceramics versus the samples treated with the IL solution (Figure 3. 6e-g); in both cases no surface-charging was observed despite the high-vacuum conditions within the microscope chamber. This finding indicates that the hydrophilic IL used in this study served a similar purpose as that of the conductive osmium coating; additionally, the IL treatment did not change the surface morphology of the specimen. It has been previously reported that metals or ceramics in dehydrated conditions can be observed using IL solutions [30, 32, 37]. The present results are in strong agreement with these earlier reports. However, it was not possible to observe the porous HAp body treated with the IL at a very high magnification, which was otherwise achieved for the samples with the osmium coatings, as shown in Figure 3. 6d. At very high magnifications, the electron beam locally irradiates the porous HAp body and the IL; thus, the IL within the porous body was identified on the sample surface. From this observation, it was determined that the structure of the porous HAp body had significantly changed. From the above results, it was possible to identify the observational limitation associated with the IL treatment.

Although the surface morphology of the dried porous HAp body was clearly identifiable for the samples that were treated with the hydrophilic IL, nonetheless, it is interesting to examine the hydrated green body following the same treatment.

3. 3. 3. Characterization of wet HAp porous green body.

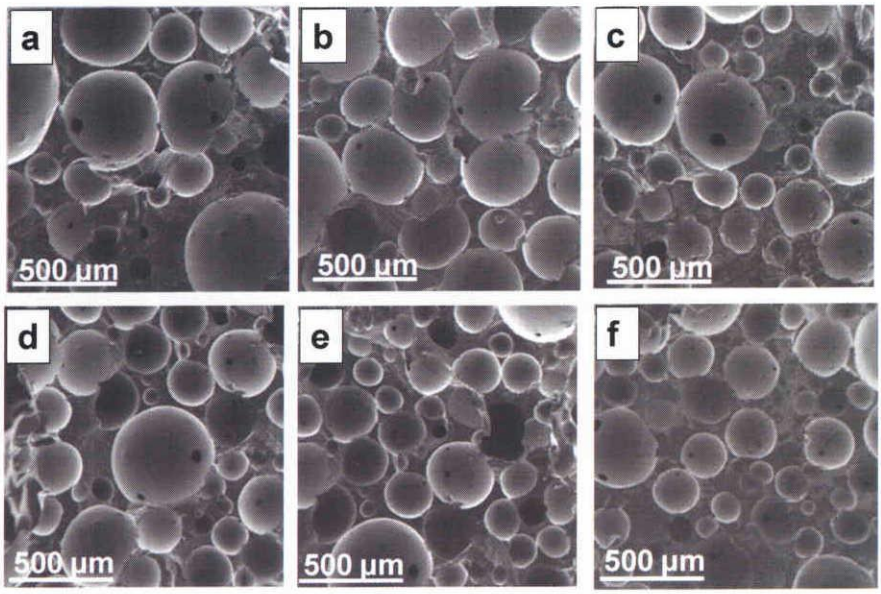

Figure. 3. 7. FE-SEM images of (a) the as-prepared porous HAp green body just after removal from the mould and of the specimens treated in the humid chamber at (b) 90, (c) 80, (d) 70, (e) 60 and (f) 50 % relative humidity.

Figure 3. 7a-f shows FE-SEM images of the as-prepared porous HAp green bodies and of the samples that were treated in the humid chamber as it was gradually reduced from 90 to 50 % relative humidity by 10 % per day; the IL treatment followed this treatment. Figure 6 shows the high-magnification FE-SEM images of both sample types, the as-prepared and the dehumidified, in similar conditions. It can be seen from Figures 3. 7 and 3. 8 that the as-prepared porous HAp green body consisted of large pores approximately 300-

600 μm in diameter and that, during the course of drying in the humid chamber, the pore size gradually decreased to approximately 200-400 μm.

Table 3. 1. Comparison of the water contents of the porous HAp green bodies just after removal from the mould and of the samples maintained in the humid chamber as it was reduced from 90 to 50 % relative humidity.

Condition	As-prepared	90 %	80 %	70 %	60 %	50 %
Water content (Wt %)	31.51	25.39	21.25	18.58	15.08	11.06

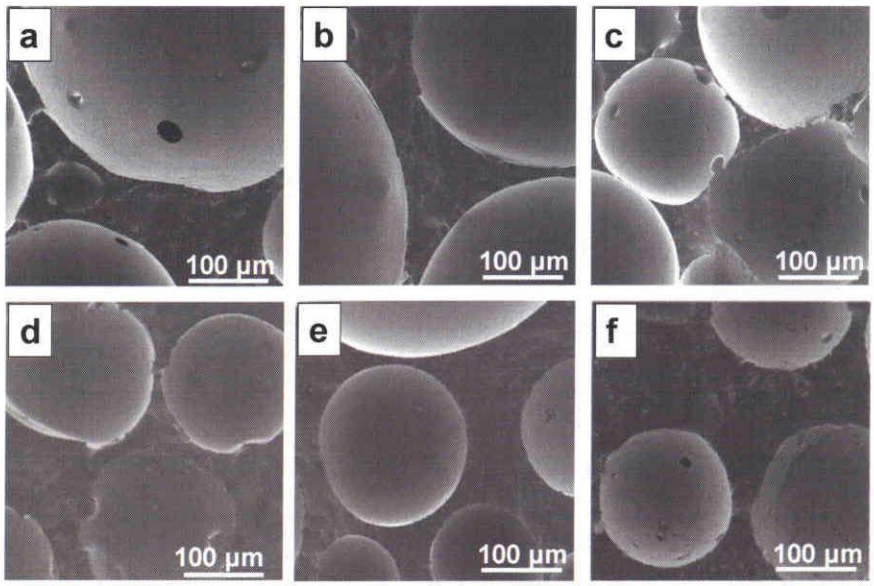

Figure. 3. 8. High-magnification FE-SEM images of (a) the as-prepared porous HAp green body just after removal from the mould and of the specimens treated in the humid chamber at (b) 90, (c) 80, (d) 70, (e) 60 and (f) 50% relative humidity.

Table 3. 1 shows the water content both of the porous HAp green bodies immediately following their removal from the mould and of those maintained in the humid chamber as it reduced from 90 to 50 % relative humidity. It can be seen in Table 3. 1 that the water content of the as-prepared porous HAp green body was 31.51 wt %; this value gradually decreased as the samples were maintained in the humid chamber. The water content of the samples dried at 50 % relative humidity was 11.06 wt %, which indicates that the sample still contained some water. This water was likely trapped in the pores as well as within the network structure, which was formed by the polymer and the HAp ceramic. As the trapped water inside the as-prepared green HAp body gradually evaporates inside the humid chamber, a gradual shrinking of the pores and the HAp particles in the polymer network is expected; this phenomenon was observed in Figures 3. 7 and 3. 8. Further, it can be seen that the green body dried at 50 % relative humidity had larger pore sizes than the sample sintered at 1000 °C for 2 h (Figures 3. 6e and 3. 7f). This result indicates that the remaining trapped water inside the pores and in the networks was evaporated above 100 °C in the electric furnace.

Additionally, sintering of the HAp particles at 1000 °C initiated a significant contraction of the pore sizes as the water was evaporated and the polymer was burned out (above 500 °C). Hence, in a comparison of FE-SEM images in Figures 3. 6 to 3. 8, the morphologies of both the green and the sintered porous HAp bodies are readily observed, even when the samples were subjected to the hydrophilic IL solution without the addition of a conventional conductive coating such as Au, Os, Pt / Pd or carbon. Furthermore, the green body which contains a large amount of water, was readily observed in the FE-SEM chamber

under high-vacuum conditions without any drying of samples. The possible reasons for this observation will be discussed later in this section.

Table 3. 2. Comparison of the change in pore diameter of the porous HAp green bodies just after removal from the mould and of the samples maintained in the humid chamber as it was reduced from 90 to 50 % relative humidity.

Condition	As-prepared hydrated green body	90 %	80 %	70 %	60 %	50 %	After sintering, 1000 °C for 2 h
Average Pore diameter (μm)	342	324	299	279	265	252	196

Table 3. 2 shows the average pore diameter as measured from the FE-SEM images of the samples with respect to drying and subsequent sintering at 1000 °C for 2 h. From Table 3. 2, it can be seen that the as-prepared porous HAp green body contains pores with an average pore diameter of 342 μm. These pores were gradually reduced in size to approximately 252 μm when the samples were kept in the humid chamber at 50 % relative humidity. There is also a possibility that any pores below 100 μm in size might have disappeared during the drying and subsequent sintering processing steps. The porous bodies sintered at 1000 °C for 2 h showed pores with an average diameter of 196 μm.

Figure 3. 9a-f shows the micro-focused X-ray CT images of both the as-prepared green HAp porous body and the samples treated in the humid chamber at different humidity values. It can be seen that the as-prepared sample had large pores measuring approximately 300-600 μm (Figure 3. 9a) and that during the course of drying in the humid chamber, there

was a gradual reduction in the pore sizes to approximately 200-400 μm (Figure 3. 9f). Thus, the observed changes in the pore sizes with respect to the drying condition based on the micro-focused X-ray CT images (Figure 3. 9) have strong agreement with the FE-SEM images (Figure 3. 7). In general, the micro-focused X-ray CT technique is useful for generating real images without structural disorder. However, it is difficult to obtain high-magnification or high-resolution images using this method.

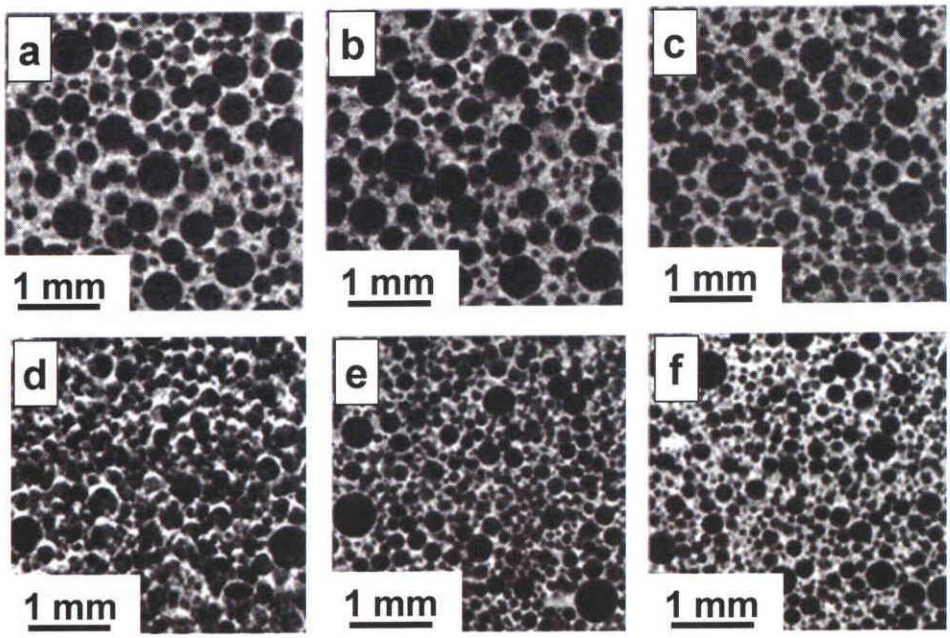

Figure. 3. 9. Micro-focused X-ray CT images of (a) the as-prepared porous HAp green body just after removal from the mould and of the specimens treated in the humid chamber at (b) 90, (c) 80, (d) 70, (e) 60 and (f) 50 % relative humidity.

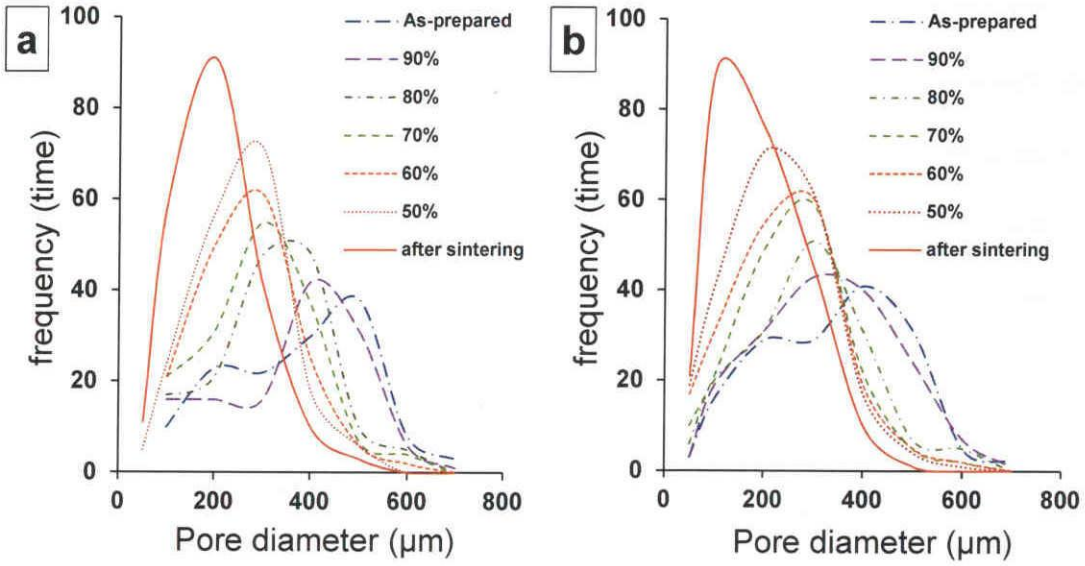

Figure. 3. 10. Comparative study of the distribution of the pore diameters of the porous HAp green body and of the specimens maintained in the humid chamber as it was reduced from 90 to 50 % relative humidity; the pore diameter values were measured from (a) the micro-focused X-ray CT and (b) the FE-SEM images.

Figures 3. 10a and b show a comparative study of the distribution of the pore diameters of the porous HAp green body and the samples maintained in the humid chamber, as measured from the micro-focused X-ray CT and FE-SEM images, respectively. Figure 3. 10a shows that each distribution was shifted during the drying treatment. However, using the micro-focused X-ray CT, any pore sizes below 100µm could not be observed in either the as-prepared porous body or in the specimens maintained in the humid chamber. Hence, observations of the pore structure using the micro-focused X-ray CT technique were likely

limited due to the water contents of the samples. However, it was possible to observe the fine pore structure (below 100 μm in size) with the FE-SEM, and in so doing, a similar trend in the peak shift with respect to the drying condition was noticed (Figure 3. 10b). Figure 3. 11 shows the distribution of the average of pore diameters as measured from the micro-focused X-ray CT and FE-SEM images. In particular, the pore diameter of the as-prepared HAp porous green bodies, which possessed a large amount of water, and of the samples maintained in the 90 % relative humidity condition were different, according to the results of the micro-focused X-ray CT and FE-SEM images. It is likely that small pores cannot be detected with the micro-focused X-ray CT technique. Therefore, there is the possibility of error in any pore size measurements that are based on this approach.

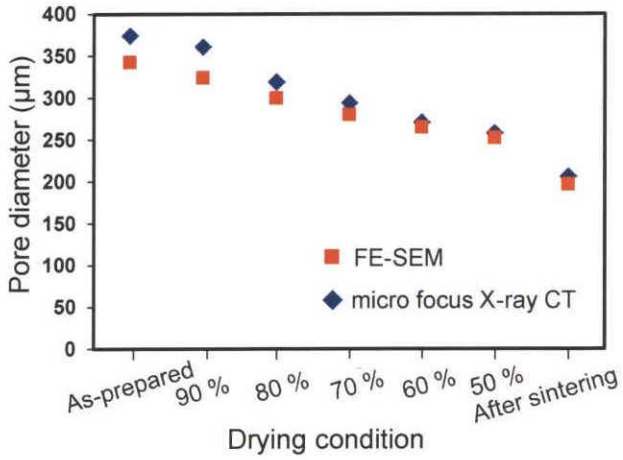

Figure. 3. 11. Distribution of the pore diameters of the HAp green porous body and of the samples maintained in the humid chamber as it was reduced from 90 to 50 % relative humidity, as measured from the micro-focused X-ray CT and the FE-SEM images.

Table 3. 3. Dimensional changes of the porous HAp green bodies just after removal from the mould and of the samples treated in the humid chamber at 80, 50 % relative humidity and of the porous body sintered at 1000°C for 2h and examination of the size retention of the green bodies fabricated at a similar condition and subjected to the IL treatment.

Condition	As-prepared wet green body	80 %	50 %	After sintering, 1000 °C, 2 h
Size retention until sintering (%)	100.0	93.4	78.6	52.7
Size retention after IL treatment (%)	99.0	99.0	99.6	99.8

Table 3. 3 shows the dimensional changes in the as-prepared porous HAp green bodies and in the samples that were maintained in the humid chamber at 80 and 50 % relative humidity, both of which were followed by sintering at 1000 °C for 2 h before and after the IL treatment. In Table 3. 3, we can see that the porous HAp green body showed significant dimensional changes, i.e., the porosity was 78.6% during drying and 52.7 % after sintering at 1000 °C for 2 h. However, when treated under similar conditions and followed by the IL treatment, exhibited only 0.02 % shrinkage, which is significantly less. This result indicates that when the porous bodies in different hydrated conditions were subjected to the hydrophilic IL treatment, they further retained their structures without any changes in morphology and with only negligible changes in dimensions. Table 3. 3 shows

that approximately 20 % volume shrinkage occurs during the course of drying the green HAp porous bodies. In comparing Tables 3. 1 and 3. 3, it can be seen that there was an insignificant difference between the reduction in water content and the volume shrinkage of the HAp porous green body as a result of drying. Therefore, it can be assumed that only the water contained within the porous body could have evaporated when the samples were maintained in the humid chamber. Thus, a 20 % loss of the water from within the porous body during the drying process might further correspond to the 20 % shrinkage in sample size, which was observed in Table 3. 3. In Table 3. 2, it can be seen that there is an approximately 20-30 % shrinkage in the pore diameter during the course of drying the green HAp porous bodies; additionally, approximately 20 % of the observed reduction in the pore diameter occurred during sintering at 1000 °C for 2h. Thus, the reduction in the pore volume can be calculated using the average of pore diameter. During the course of drying the green HAp porous bodies, there is an approximately 40 % shrinkage in the pore volume; furthermore, an approximately 40 % shrinkage in the pore volume occurred during sintering at 1000 °C for 2h. From these results, it is expected that the reduction in the wall space surrounding the pores is lower than that of the pore space. In this study, the sample size was fixed at 5.0 × 5.0 × 5.0 mm^3 to accommodate the IL treatment. It is possible that a reduction in pore size in addition to a reduction in the sample size may occur due to the small size of the sample.

In Table 3. 3, it can be seen that, following the IL treatment, the porous HAp body did not show any significant shrinkage even though the porous bodies contained a large amount of water. Therefore, it can be inferred that the hydrophilic IL used in this

investigation interacted with the remaining water molecules and that the IL replaced the water within the porous body [36, 37]. In our previous study, we reported that the water within the agar gel binds with the IL to form a weak hydrogen bond, thereby preventing the agar gel from dehydrating in the FE-SEM chamber while under vacuum. When the water concentration of the sample following the IL treatment is 30 mol %, the IL and the water molecules have a tendency to form weak hydrogen bonds, such as HOH...BF_4...HOH, in the hydrated porous HAp body. These weak bonds prevent the porous HAp green body from dehydrating in a similar manner to that of the agar gel, which allows the collection of high-magnification images by FE-SEM. The IL in the present study not only bonds with the water molecules inside the network structures but also acts as a conductive coating, which prevents surface charging of the ceramic bodies like the HAp body investigated in work. To examine the behavior of the water and the polymer (epoxy resin) used in gelcastings during the drying process, further high-magnification images were collected.

Figure 3. 12a-f shows the high-magnification FE-SEM images of the as-prepared green HAp porous body and those that were subsequently maintained in the humid chamber. In this study, we focused on the pores of the porous body; due to the wall space, the hydrated specimens proved difficult to cut while maintaining correct morphology. It can be seen that a swollen morphology was observed both in the as-prepared porous body as well as in the sample maintained in the humid chamber at 90 % relative humidity for 1 day (Figure 3. 12a and b). However, when the relative humidity was decreased from 90 to 50 %, due to the gradual loss of the water content, the particles appeared to separate as shown in Figure 3. 12c-f. The porous bodies maintained in the humid chamber at 50 % relative humidity and

treated with the IL revealed the presence of fine particles, which were similar in appearance to that of the HAp porous body after sintering (Figure 3. 12f). Thus, in these FE-SEM images, a fine morphology with sub-micron-sized particles was clearly observed for the specimens treated with the hydrophilic IL or simply maintained in the hydrated conditions.

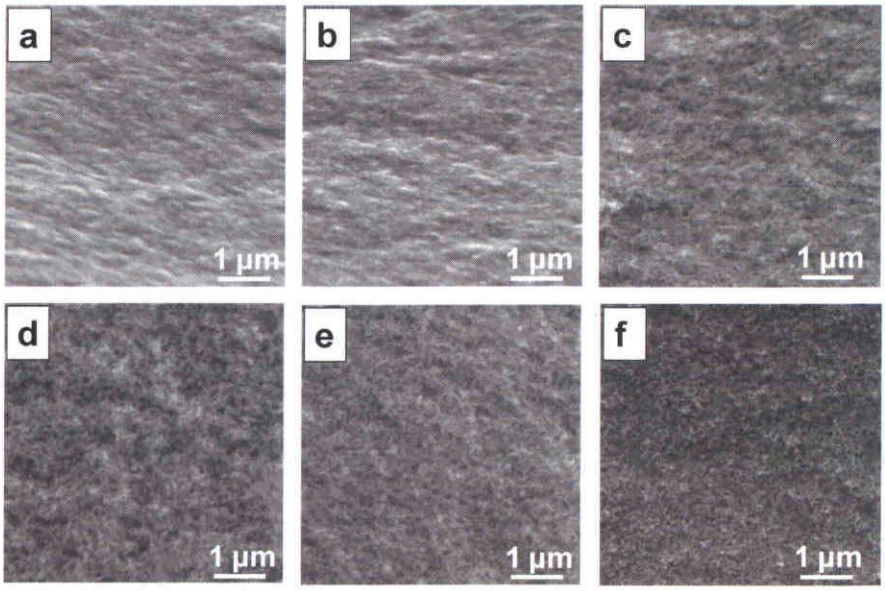

Figure. 3. 12. High-magnification FE-SEM images of (a) the as-prepared porous HAp green body just after removal from the mould and of the samples treated in the humid chamber at (b) 90, (c) 80, (d) 70, (e) 60 and (f) 50 % relative humidity.

3. 3. 4. Behavior of water within HAp porous green body during IL treatment.

Figure 3. 13 shows the Raman spectra of collected IL solution *[HAp_{IL}]* with respect to drying condition in humid chamber in the range of 2800 to 3800 cm^{-1} after keeping them in desiccator for 2 h + under vacuum condition at 60 °C for 24 h. For comparison, Raman

spectra of raw IL and sintered porous HAp body without the IL treatment were also measured. The CH and OH stretch vibrations region in the range of 2800 to 3800 cm^{-1} were selected in order to examine the interaction between water, cationic $(BMIM)^+$ and anionic $(BF_4)^-$ part of IL [38,39]. These *[HAp_{IL}]* solutions were used for Raman analysis because HAp porous green body was kept in the same condition prior to FE-SEM observation. From Raman spectra we can see that the raw IL had no OH peak although CH peak derived from cation part of IL was observed. Porous HAp body without IL did not show any significant peak in the 2800 to 3800 cm^{-1} region due to complete evaporation of water. On the other hand, as-prepared porous HAp green body and the samples kept in the humid chamber at 80 and 50 % relative humidity showed both CH and small OH peak. This weak OH stretching vibration peak (3560 cm^{-1}) is ascribed to symmetric $BF_4^- \cdots HOH \cdots BF_4^-$ stretching mode and the OH peak position did not change with respect to HAp drying conditions. The blueshift of peak position was also not observed. In this study, we measured porous HAp body for different drying condition after adjusting total water concentration in the resultant sample (concentration of water and IL) to 30 mol %. Though each mixture was prepared with different HAp drying condition, the small area of weak hydrogen bond was only observed. Based on our previous result, we considered 30 mol % water concentrations to be an optimum condition for porous HAp body and IL to be observed under FE-SEM [36]. The IL can bind with water molecules within porous HAp body in about 30 mol % water concentration even different drying condition. Therefore, it can be explained that the hydrophilic IL used in the present study interact with the remaining water molecules within

porous HAp body, and the IL could be replaced with water within porous HAp body by specific interaction.

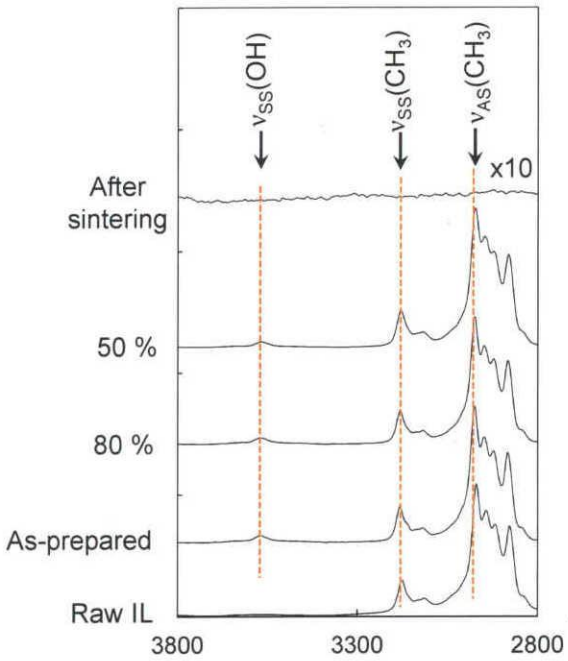

Figure. 3. 13. Raman analysis results showing the hydrogen bond formed between IL and wet HAp ceramics. The arrows show the peak of the ν_{SS}(OH), ν_{SS}(CH$_3$) and ν_{AS}(CH$_3$) stretching vibration region.

It was earlier reported that water within agar gel bind with IL forming weak hydrogen bond as $BF_4^-\cdots HOH\cdots BF_4^-$ and hence prevent the drying of agar gel in FE-SEM chamber under vacuum [36]. When water concentration of sample after IL treatment is 30 mol %, IL and water molecules form weak hydrogen bond such as BF_4...HOH...BF_4 in the porous HAp body in its hydrated condition. This weak hydrogen bonding prevents porous HAp green body from its drying in vacuum and hence high magnification images could be

clearly observed in FE-SEM. This IL in the present study not only form bonding with water molecules inside the network structures but also acts as a conducting coating which prevents from charging of HAp ceramics body.

Thus, present result showed that the surface morphology of porous HAp body in its hydrated condition can be observed by FE-SEM when the samples were subjected to the hydrophilic IL treatment. This simple method of observation can also be applied to a wide range of nonconductive ceramic materials during their wet processing.

3. 4. Conclusions

A simple and convenient method for observing the microstructure of the hydrated porous HAp green body using a hydrophilic ionic liquid is reported. The FE-SEM observations showed that the as-prepared porous green body had a pore diameter of approximately 300-600 μm, which gradually decreased to approximately 200-400 μm during drying in a humid chamber from 90 to 50 % relative humidity. Wet HAp sample when added into ionic liquid, it bonds with water molecules within the HAp-polymer network structure, thereby forming a weak hydrogen bond entangling with the HAp particles surrounding the porous body. This bonding resulted in the formation of an IL-water-HAp-polymer complex, in which the IL acted as a conducting media; additionally, the formation of weak hydrogen bonds between the IL and the water further prevented the porous HAp body from dehydrating in the FE-SEM chamber while under vacuum. Further, the limitations of observing the hydrated porous HAp green body by micro-focused X-ray CT were revealed. It can be concluded from this investigation that it is possible to

observe interaction of wet ceramic gels with cultured cell and microorganism using hydrophilic ionic liquid.

References

[1] L.L. Hench, J. Wilson, An Introduction to Bioceramics, World Scientific, Singapore, 1993.

[2] K.de. Groot, Clinical applications of calcium phosphate biomaterials: A Review, Ceram. Int. 19 (1993) 363-366.

[3] L.L. Hench, J. Am. Ceram. Soc. 74 (1991) 1487-1510.

[4] D.K. Pattanayak, B.T. Rao, T.R. Rama Mohan, J. Sol-gel. Sci. Techn. 59 (2011) 432-447.

[5] B.S. Chang, C.K. Lee, K.S. Hong, H.J. Youn, H.S. Ryu, S.S. Chung, K.W. Park, Biomaterials 21 (2000) 1291-1298.

[6] H. Yuan, K. Kurashina, J.D.de. Bruijn, Y. Li, K.de. Groot, X. Zhang, Biomaterials 20 (1999) 1799-1806.

[7] I. Sopyan, M. Mel, S. Ramesh, K.A. Khalid, Sci. and Technol. of Adv. Mater. 8 (2007) 116-123.

[8] I. Sopyan, J. Kaur, Ceram. Int. 35 (2009) 3161-3168.

[9] S. Padilla, J. Roman, M. Vallet-Regi, J. Mater. Sci:Mater. Med. 13 (2002) 1193-1197.

[10] C.J. Bae, H.W. Kim, Y.H. Koh, H.E. Kim, J. Mater. Sci:Mater. Med. 17 (2006) 517-521.

[11] W.Y. Zhou, S.H. Lee, M. Wang, W.L. Cheung, W.Y. Ip, J. Mater. Sci:Mater. Med. 19 (2008) 2535-2540.

[12] O.O. Omatete, M.A. Janney, R.A. Strehlow, Am. Ceram. Soc. Bull. 70 (1991) 1641-1649.

[13] O.O. Omatete, M.A. Janney, S.D. Nunn, J. Euro. Ceram. Soc. 17 (1997) 407-413.

[14] A.C. Young, O.O. Omatete, M.A. Janney, P.A. Menchhofer, J. Am. Ceram. Soc. 74 (1991) 612-618.

[15] J. Ma, Z. Xie, H. Miao, Y. Huang, Y. Cheng, W. Yang, J. Euro. Ceram. Soc. 23 (2003) 2273-2279.

[16] R.L. Menchavez, M. Fuji, M. Takahashi, Adv. Mater. 20 (2008) 2345-2351.

[17] O.O. Omatete, J.P. Pollinger, K. O'Young, Ceram. Trans. 56 (1995) 337-343.

[18] L.G. Ma, Y. Huang, J.L. Yang, Z.P. Xie, X.L. Xu, J.S. Zhao, J. Mater. Sci. Lett. 20 (2001) 1285-1288.

[19] M.D. Vlajic, V. D. Krstic, J. Mat. Sci. 37 (2002) 2943-2947.

[20] Z.Z. Yi, Z.P. Xie, Y. Huang, J.T. Ma, Y.B. Cheng, Ceram. Int. 28 (2002) 369-376.

[21] O.O. Omatete, A. Blair, C.G. Westmoreland, A.C. Young, Ceram. Eng. Sci. Proc. 12 (1991) 2084-2094.

[22] X. Liu, Y. Huang, J. Yang, Ceram. Int. 28 (2002) 59-164.

[23] P. Sepulveda, J.G.P. Binner, S.O. Rogero, O.Z. Higa, J.C. Brsessiani, J. Biomed. Mater. Res. 50 (2000) 27-34.

[24] D.J.A. Netz, P. Sepulveda, V.C. Pandolfelli, A.C.C. Spadaro, J.B. Alencastre, M.V.L.B. Bentley, J.M. Marchetti, Inter. J. Pharm. 213 (2001) 117-125.

[25] M. Takahashi, K. Adachi, R.L. Menchavez, M. Fuji, J. Mater. Sci. 41 (2006) 1965-1972.

[26] C. Hai, J. Liu, H. Watanabe, M. Fuji, F. Wang, M. Takahashi, J. Am. Ceram. Soc. 92 (2009) 38-41.

[27] P. Wasserscheid, C.M. Gordon, C. Hilgers, M.J. Muldoon, I.R. Dunkin, Chem. Commun. 111 (2001) 1186-1187.

[28] J.F. Wishart, E.W. Castner, J. Phys. Chem. B 111 (2007) 4639-4640.

[29] F. Golgovici, A. Cojocaru, L. Anicai, T. Visan, Mater. Chem. Phys. 126 (2011) 700-706.

[30] T. Torimoto, K. Okazaki, T. Kiyama, K. Hirahara, N. Tanaka, S. Kuwabata, Appl. Phys. Lett. 89 (2006) 243117.

[31] P. Roy, T. Dey, P. Schmuki, Electrochem. Solid-State. Lett. 13 (2010) E11-E13.

[32] S. Kuwabata, T. Tsuda, T. Torimoto, J. Phys. Chem. Lett. 1 (2010) 3177-3188.

[33] S. Arimoto, M. Sugimura, H. Kageyama, T. Torimoto, S. Kuwabata, Electrochim. Acta 53 (2008) 6228-6234.

[34] K. Kawai, K. Kaneko, H. Kawakami, T. Yonezawa, Langmuir 27 (2011) 9671-9675.

[35] C. Takahashi, T. Shirai, M. Fuji, Adv. In. Tech. Mat. Mat. Proc. J. 13 (2011) 39-47.

[36] C. Takahashi, T. Shirai, M. Fuji, Mater. Chem. Phys. 133 (2012) 565-572.

[37] C. Takahashi, T. Shirai, M. Fuji, Mater. Chem. Phys. (2012) accepted.

[38] L. Cammarata, S.G. Kazarian, P.A. Salter, T. Welton, Phys. Chem. Chem. Phys. 3 (2001) 5192-5200.

[39] Y. Jeon, J. Sung, D. Kim, C. Seo, H. Cheong, Y. Ouchi, R. Ozawa, H. Hamaguchi, J. Phys. Chem. B. 112 (2008) 923-928.

CHAPTER 4

OBSERVATION OF SEAWEED AS BIOMATERIALS USING HYDROPHILIC IONIC LIQUID

4. 1. Introduction

It is well known that room-temperature (RT) ionic liquids (ILs) has been used as solvents in various chemical reactions [1-3], or in dispersion of carbohydrate polymers such as cellulose and starch etc in recent days [4-6]. Further, composite gel mixed with IL is used in drug delivery systems and fabrication of contact lenses [7-10]. In ceramics field, solid electrolytes and electrodes are fabricated using IL [11-13].

Besides these applications, samples such as biological materials mixed with ILs are directly observed in electron microscope due to their negligible vapor pressure and high conductivity [14-17]. Recently, it is reported that IL mixed with water or organic solvent before sample treatment are useful for SEM observation [18-21]. However, some reports suggested that wet materials such as seaweed, chicken tissue etc mixed with typical commercially available IL is not suitable for observation by SEM [22]. Furthermore, excess IL around sample is reported to be a problem for SEM observation. Therefore, modification in sample preparation method is required.

We previously proposed that the exact morphology of wet material such as agar gel or gelcast ceramics could be observed by FE-SEM, and, suggested the observation

mechanism [23,24]. It is due to the specific interaction between water molecules within agar gel or gelcast ceramics and hydrophilic IL and that prevent the gel from drying in vacuum. However, using similar methodology, biological material such as seaweed could not be observed. Therefore, in this study, we proposed a modified method to observe the exact morphology of seaweed using hydrophilic IL; 1-butyl-3-methylimidazolium tetrafluoroborate; (BMIM)(BF_4). Here, IL diluted by water is used as the solvent to maintain the osmotic pressure of seaweed in the solution. Based on optimum concentration of IL solution high magnification image could be successfully obtained by this technique without additional conducting coating.

4. 2. Materials and methods

4. 2. 1. Materials.

The ionic liquid IL; 1-butyl-3-methylimidazolium tetrafluoroborate ((BMIM)(BF_4)) was purchased from Kanto Chemical Co., Japan and dried in a vacuum desiccator at 60 °C for 1 day. Water content of IL was below 128 ppm. A commercially available dried seaweed from Sanriku area (Japan) was used (Yamanaka food Co, Japan) in the present study. Two different methods were followed to swell the seaweed i.e soaking in 3.5 % NaCl solution similar to the concentration of sea water for 10 min or soaking in ultrapure water (ADVANTEC) for 10 min, and then both cases dried under vacuum condition for 1 day.

4. 2. 2. Morphological observation of seaweed by optical microscope and FE-SEM.

Surface morphology of dried seaweed coated by Osmium metal was observed using field emission scanning electron microscope (FE-SEM, JEOL, JEM 7600F, Japan) with accelerating voltage of 5.0 kV. Swelled seaweeds prepared as described in section 2.1 were characterized using optical microscope (KEYENCE, VHX-200, Japan) and also FE-SEM with accelerating voltage of 5.0 kV. First, the seaweed was observed with optical microscope at the atmosphere owing to obtain natural morphology. Subsequently, seaweed was picked up and treated with IL solution. Three different conditions IL solutions mixed with water were prepared where IL:water ratio 1:0, 1:1 and 1:7 designated as [IL/W_{10}], [IL/W_{11}] and [IL/W_{17}], respectively. Then seaweed and IL solutions were mixed in amount ratio of 1:30 for all conditions and then the seaweed sample was kept in dessicator for 2 h, and under vacuum condition for 24 h. Excess IL around sample were removed by using Kim wipe as conventional method or centrifuged in different rotation speed at 500, 5000 and 10000 revolutions per minutes (rpm), respectively to examine the effect of remnant IL solution on surface morphology. The FE-SEM images of seaweed treated with IL solution were compared with optical microscope images.

4. 2. 3. Size measurement of seaweed after IL treatment.

Size retention of the seaweed treated with IL and water mixture ratios described in section 2.2 i.e. [IL/W_{10}], [IL/W_{11}] and [IL/W_{17}] was measured after keeping in a desiccator for 2 h and under vacuum condition for 24 h and removed excess IL using centrifuge at 10000 rpm (as FE-SEM sample preparation). Initially each seaweed was cut into 5.0 × 5.0 ×

5.0 mm^3 in size and the measurement was carried out. The dimensions of seaweed after IL treatment were measured by ruler as shown in Figure 4. 1. Both sides (X and Y) of sample were measured and calculated average as (X+Y)/2. The size retention ratio was calculated as (X+Y/2)/5 × 100.

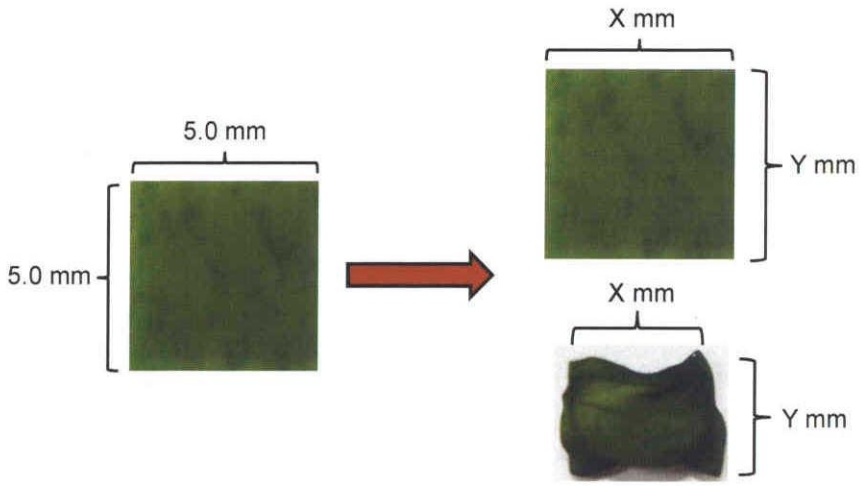

Figure. 4. 1. Size measurement of the seaweed after keeping under a vacuum for 24 h.

4. 3. Results and discussions

4. 3. 1. Morphological observation of dried seaweed using osmium coating.

Figure 4. 2 shows FE-SEM images of osmium coated dried seaweed after soaked in 3.5 % NaCl solution for 10 min and kept in vacuum dryer for 24 h. Fig. 2a shows low magnification image of dried seaweed. Large number of wrinkle structures which were caused by drying could be observed clearly. When focused on wrinkle structure, crushed scale-like structure was observed as shown in Figure 4. 2b. Moreover, high magnification

images showed about 5 μm size dried cells like star fish which were not swelled (Figure 4. 2c). These cells are observed in whole seaweed surface. Focused on substructure without star fish-like cell, many bosses with several nm were observed (Figure 4. 2d and e).

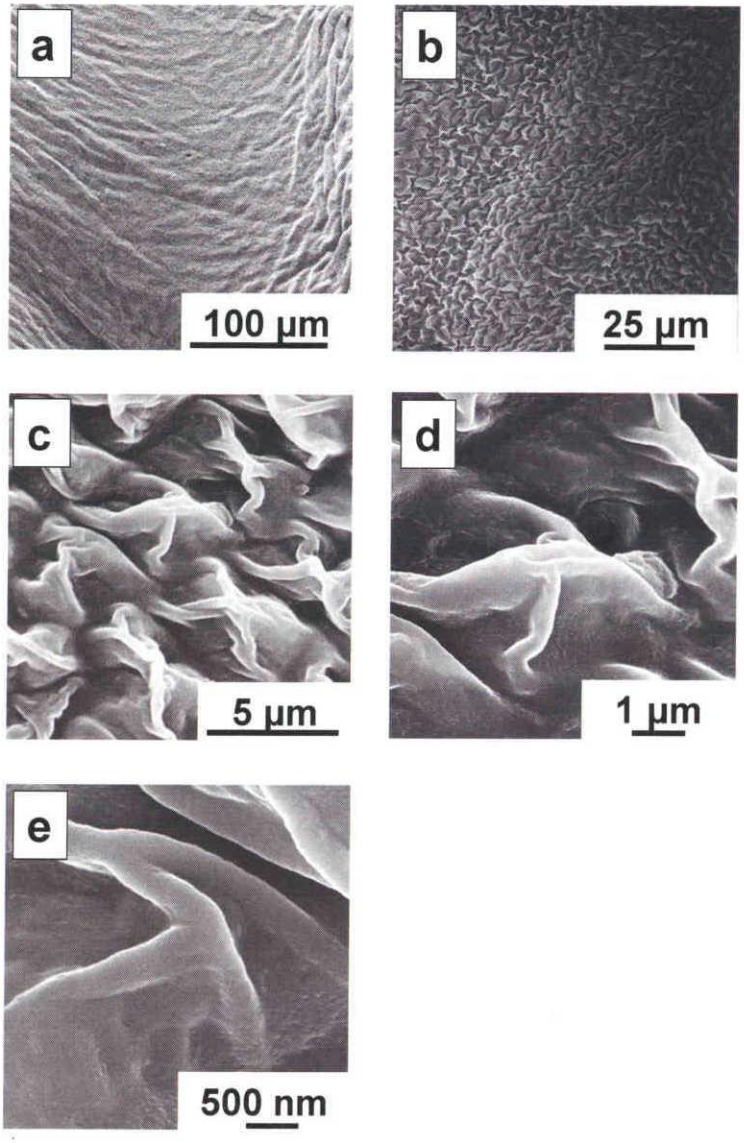

Figure. 4. 2. (a)-(e) FE-SEM images of osmium coated dried seaweed after soaked in 3.5 % NaCl solution for 10 min and kept in vacuum dryer for 24 h.

Figure 4. 3 shows FE-SEM images of osmium coated dried seaweed after soaked in ultrapure water for 10 min and kept in vacuum dryer for 24 h. Most of the parts appeared to be nearly flat morphology although some square structure of about 10μm in size was observed (Figure 4. 3b). However neither crashed scale-like structure nor star fish-like cells at high magnification was observed (Figure 4. 3c-e). This indicates that when dried seaweed was treated with ultrapure water, structures of star fish-like cells were completely destroyed (Figure 4. 3a-e) as compared to seaweed treated with 3.5% NaCl solution (Figure 4. 2a-e).

This indicates that the osmotic pressure of seaweed in water became low, and hence the structures of star fish-like cells were changed drastically. Thus, in order to maintain the osmotic pressure of seaweed in solution which is a key factor for observation of exact morphology, we used 3.5 % NaCl solution similar to the concentration of sea water for soaking of dried seaweed for further studies.

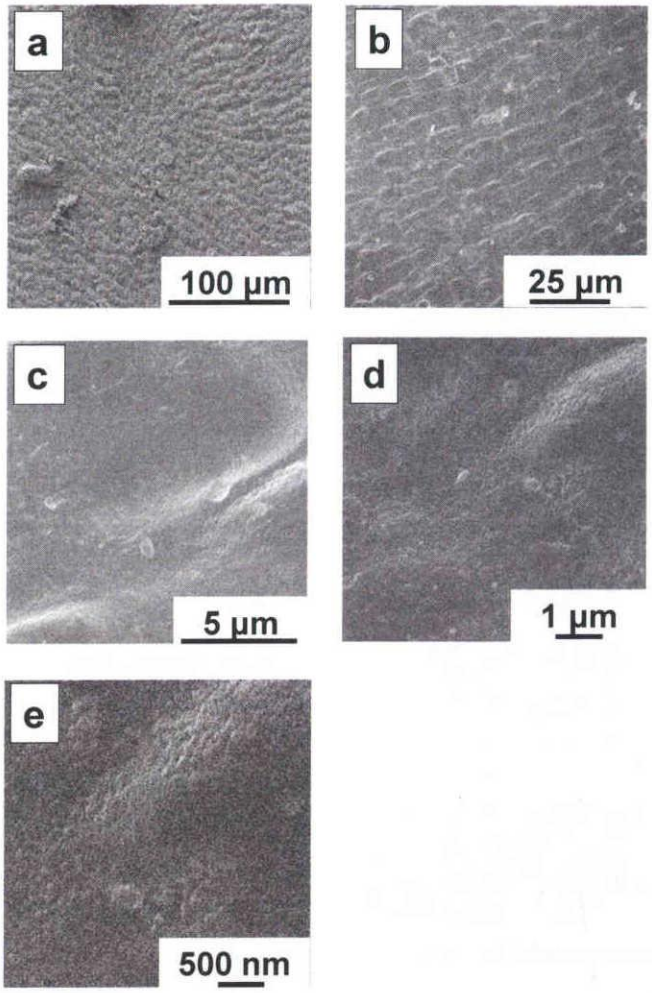

Figure. 4. 3. (a)-(e) FE-SEM images of osmium coated seaweed after soaked in ultrapure water for 10 min and kept in vacuum dryer for 24 h.

4. 3. 2. Morphological observation of wet seaweed in IL solution.

Figure 4. 4 shows the optical microscope and the FE-SEM image of swelled seaweed which was treated with different solutions. Figure 4. 4a and b shows optical microscope image of swelled seaweed after soaked in 3.5 % NaCl solution for 10 min, and then treated with IL solution [IL/W_{17}] and centrifuged at 10000 rpm, respectively. Results

showed that the morphology of swelled seaweed could be maintained despite treated with IL solution. Figure 4. 4c-g shows the FE-SEM images of swelled seaweed of different magnifications after soaked in 3.5 % NaCl solution for 10 min and IL treatment by [IL/W_{17}] and centrifuged at 10000 rpm. Comparing optical photograph in Figure 4. 4a and low magnification FE-SEM image in Figure 4. 4c, more fine morphology could be observed in latter case. Thus using FE-SEM, brain-like swelled morphology with tube structure of 50 μm widths was observed (Figure 4. 4c). Furthermore, when focused on brain-like morphology, scale-like structure could be observed. Swelled morphology was obtained by comparison with Figure 4. 4d. FE-SEM images at high magnification, there are many swelled cell with 5 μm size obviously (Figure 4. 4e). Similar to Figure 4. 2, these cells are spread in whole seaweed surface. In comparison with Figure 4. 2c-e, star fish-like morphology was changed to swelled morphology (Figure 4. 4f and g). Even at substructure, bosses sizes were increased drastically in the range of several dozen to several hundred nm. In addition, bosses could be observed on the cell.

From these results, it is found that FE-SEM is more useful method to observe fine morphology than optical microscopy due to higher focal depth. Thus using FE-SEM, fine morphology with several nm ranges can be clearly observed without any conventional conductive coating. In order to obtain an optimum condition of sample preparation for FE-SEM observation, seaweed morphology in different IL concentrations with respect to different osmotic pressure of seaweed in IL solution using FE-SEM are examined.

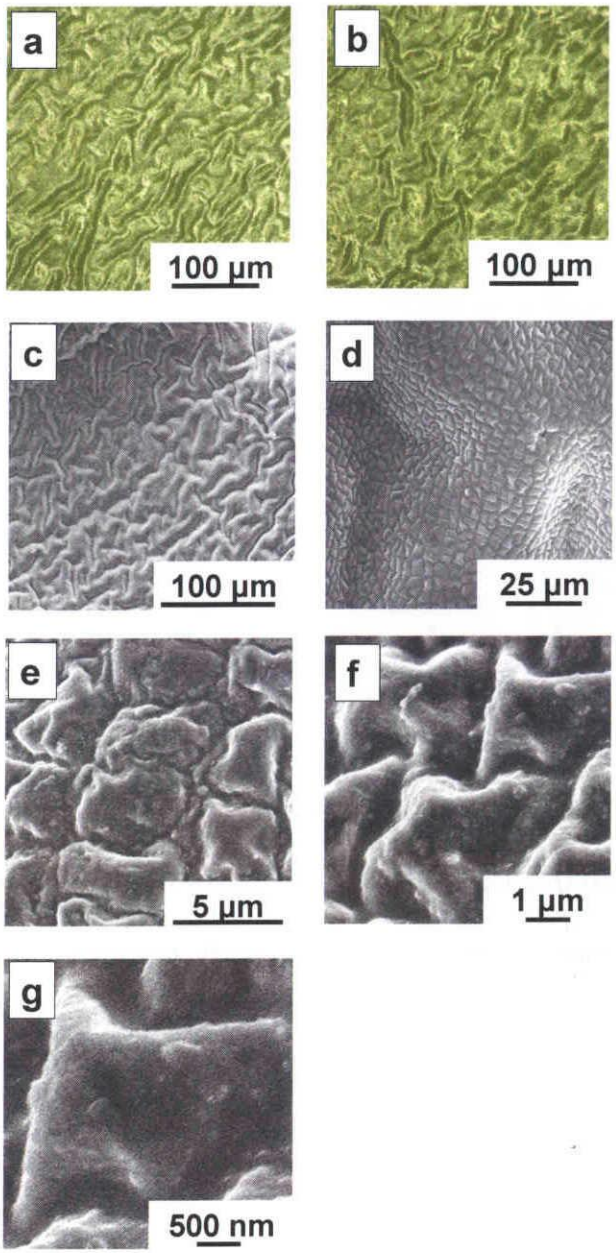

Figure. 4. 4. (a), (b) Optical microscope images of swelled seaweed after soaked in 3.5 % NaCl solution for 10 min and (c), (d) FE-SEM images after soaked by 3.5 % NaCl solution for 10 min and IL treatment by [IL/W_{17}] and kept in desiccators for 2 h and under vacuum condition for 24 h and used centrifuge at 10000 rpm.

4. 3. 3. Morphological observation of seaweed in wet condition by different IL treatment.

Figure 4. 5 shows FE-SEM images of swelled seaweed treated with IL in different concentration. Figure 4. 5a and b shows FE-SEM image of swelled seaweed after soaked in 3.5 % NaCl solution for 10 min and raw IL treatment [IL/W_{10}] and keeping in dessicator for 2 h and dried in vacuum condition for 24 h and centrifuged at 10000 rpm. Figure 4. 5c and d shows swelled seaweed prepared by same method with different IL concentrations [IL/W_{11}]. FE-SEM image of swelled seaweed after raw IL treatment (Figure 4. 5a) was appeared to be different compared to Figure 4. 4c and Figure 4. 5c. Also in high magnification image (Figure 4. 5b), shrinkage of swelled cell was found in comparison with Figure 4. 4f. The cell size was reduced from about 5 to 3 μm and some wrinkles were partially observed (Figure 4. 5b). FE-SEM image of swelled seaweed after IL treatment by [IL/W_{11}], brain-like swelled morphology which has tube structure of 50 μm widths was observed similar to Figure 4. 4c (Figure 4. 5c). In high magnification image, shrinkage of swelled cell was not found and fine morphology could be observed including bosses (Figure 4. 5d).

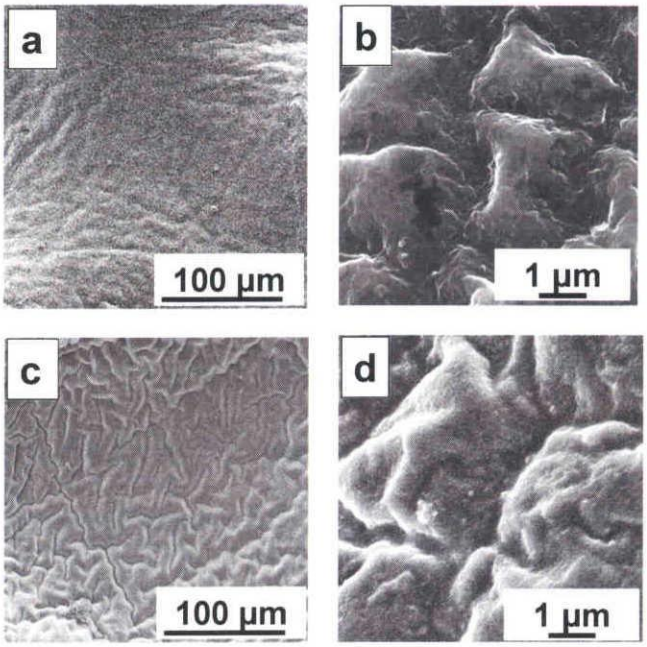

Figure. 4. 5. FE-SEM image of swelled seaweed after soaked by 3.5 % NaCl solution for 10 min and (a), (b) raw IL treatment and (c), (d) IL treatment by [IL/W_{11}] and both of keeping in dessicator for 2 h and under a vacuum for 24 h and used centrifuge at 10000 rpm.

Table 4. 1. Size retention of the seaweed treated with different amount of IL and water ratio after keeping in desiccators for 2 h and dryed in vacuum for 24 h.

Mixing ratio (IL : water)	Size retention (%)
1 : 0	64.1
1 : 1	89.1
1 : 7	97.6

Table 4. 1 shows an examination of size retention of seaweed subjected to IL and water ratio which is gradually changed from [IL/W_{10}] to [IL/W_{17}] through [IL/W_{11}]. Results showed that when IL treatment by [IL/W_{17}], seaweed retained its size above 97 %. IL treatment by [IL/W_{11}], size retention was 89.1 %. Thus, it is considered that morphology of inside of seaweed was partially changed though surface morphology of seaweed was maintained. IL treatment by [IL/W_{10}], size retention was 64.1 %. This indicates that there was significant change in seaweed morphology when the sample was treated with raw IL only i.e. [IL/W_{10}] condition.

From these results, it is clear that IL treatment in the ratio [IL/W_{17}] enable to maintain osmotic pressure of swelled seaweed in IL solution similar to seaweed swelled by 3.5 % NaCl solution. On the other hand, IL affects the morphology of swelled seaweed when IL amount is higher than IL:water=1:7 due to decrease in osmotic pressure of swelled seaweed. Thus IL:water ratio above 1:7 is considered as hypertonicity condition. Hypertonicity is the presence of a solution that causes cells to shrink. The exact morphology of seaweed could not observed when water amount is higher than IL:water=1:8 (result not shown here) and the results are same as seaweed swelled by water (Figure 4. 3).

Owing to understand the effect of change in the osmotic pressure to seaweed morphology, osmotic pressures of seaweed in sea water and seaweed treated with [IL/W_{17}] were calculated using van't Hoff equation.

$$\Pi = MRT \qquad (1)$$

Where, Π is osmotic pressure (atm), M is the Molar concentration (mol/l), R is the gas constant (atm dm^3/K mol) and T is the temperature (K). From calculation using equation (1),

the corresponding osmotic pressure of seaweed in sea water was found to be 14.65 atm and osmotic pressure of seaweed treated with [IL/W_{17}] was found to be 13.52 atm. Although osmotic pressure shows slight difference between osmotic pressures of seaweed in sea water and seaweed treated with [IL/W_{17}] solution, it can be considered that osmotic pressure of seaweed treated with [IL/W_{17}] is isotonic.

From these results, it can be seen that when the osmotic pressure is same as seaweed in sea water, the morphology of seaweed can be maintained using IL solution and observed by FE-SEM. However, it is essential to examine the effect of excess IL around seaweed in order to investigate the optimization method for FE-SEM observation using IL solution. Hence, we need to confirm the seaweed morphology after centrifugation of treated sample at different rotation speed.

4. 3. 4. Morphological observation of seaweed in wet condition by different rotation speed of centrifuge.

Figure 4. 6 shows FE-SEM images of swelled seaweed treated with IL solution and centrifuged in different rotation speed. Figure 4. 6a and b shows FE-SEM images of swelled seaweed after soaked in 3.5 % NaCl solution for 10 min and IL solution treatment by [IL/W_{17}] and keeping in dessicator for 2 h and under a vacuum for 24 h and removed excess IL using Kim wipe. And swelled seaweed prepared by same method and subsequently centrifuged at 500 and 5000 rpm was also observed (Figure 4. 6c-f). In this study, we used IL solution treatment [IL/W_{17}] for different centrifugation speed.

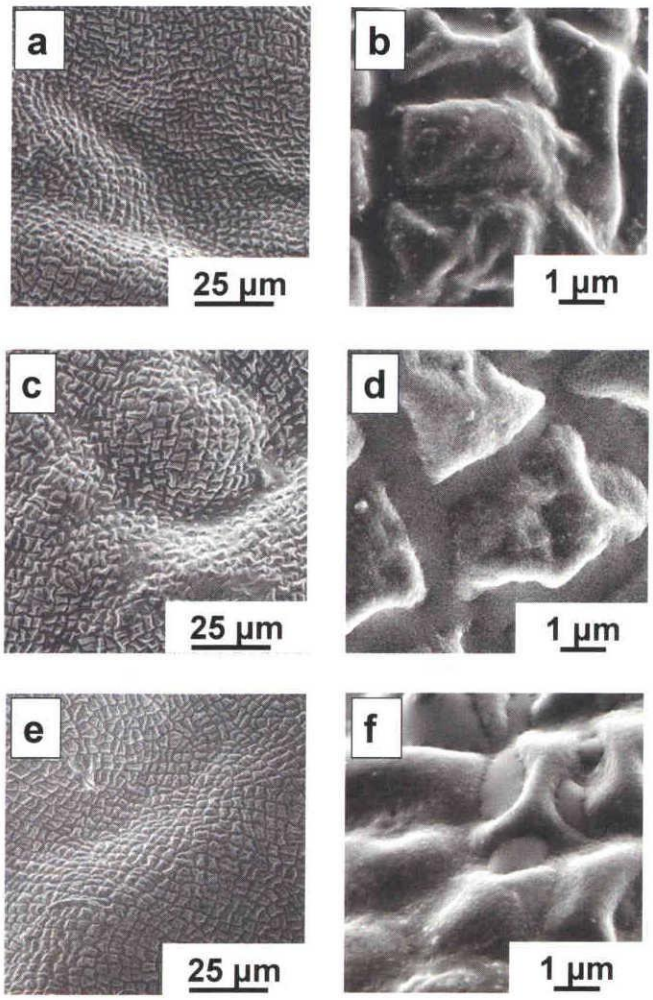

Figure. 4. 6. FE-SEM images of swelled seaweed after soaked by 3.5 % NaCl solution for 10 min and IL treatment by [IL/W_{17}] and keeping in dessicator for 2 h and under a vacuum for 24 h and removed excess IL using Kim wipe (a), (b), and, used centrifuge at (c), (d) 500 rpm, and, (e), (f) 5000 rpm.

Using Kim wipe for removal of excess IL as conventional method, scale-like morphology could be observed at low magnification (Figure 4. 6a). However, the fine morphology in indentation part of swelled seaweed could not be clearly observed (Figure 4.

6b). FE-SEM image of swelled seaweed after centrifuged at 500 rpm, even at low magnification, some parts of swelled seaweed were not observed due to excess IL (Figure 4. 6c). At high magnification, large amount of IL can be seen like pool (Figure 4. 6d). FE-SEM image of swelled seaweed after centrifuged at 5000 rpm, it can be seen the scale-like morphology without excess IL (Figure 4. 6e). However, some IL pools were observed at high magnification (Figure 4. 6f). Moreover, comparing with Figure 4. 4f, bosses were not observed in Figure 4. 6d and f. It is found that excess IL of surface part of swelled seaweed could not be removed at 500 and 5000 rpm.

From these results, using conventional method, fine morphology cannot be observed in indentation part although surface morphology can be observed. Hence, centrifuge at 10000 rpm is very useful to remove excess IL around sample for observation of fine morphology.

A schematic could be proposed for preparation method of seaweed sample for FE-SEM observation and is shown in Figure 4. 7. From our previous study, sample preparation method for agar gel was different with seaweed. Gel sample was observed by setting as 30 mol % H_2O concentration for mixture of IL and water within agar gel. However, biomaterial sample needs to consider the osmotic pressure of sample in IL solution and sample preparation has to be modified.

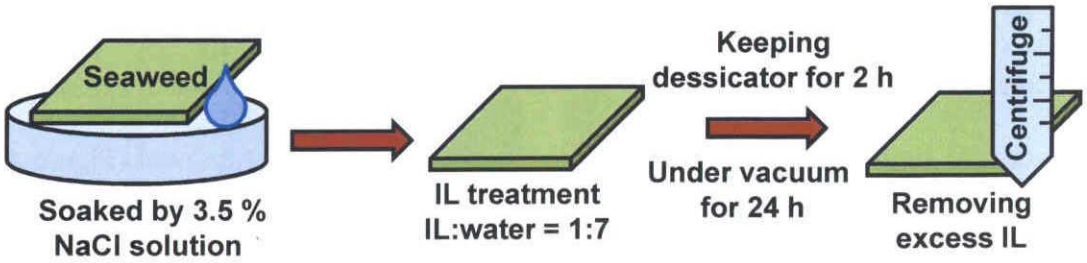

Figure. 4. 7. Sample preparation method for FE-SEM observation using IL.

4. 4. Conclusions

Exact morphology of swelled seaweed could be observed by FE-SEM using hydrophilic IL (BMIM)(BF_4). We suggested the optimization method of seaweed as biological materials for FE-SEM observation and the observation mechanism of biological materials was different compared to gel materials. It is confirmed that osmotic pressure of biomaterials in IL solution affects its configuration. Moreover, excess IL around sample was interrupted to obtain fine morphology image, however centrifuge with optimized rotation speed enable to solve the problem.

To summarize the present method, (1) seaweed was soaked in 3.5 % NaCl solution as same concentration of sea water. (2) IL treatment by [IL/W_{17}] and keeping in dessicator for 2 h and under a vacuum for 24 h. (3) excess IL around sample was removed using centrifuge at 10000 rpm.

Consequently, this electron microscope observation using optimization method of sample preparation will be very useful in understanding the exact morphology of biological materials.

References

[1] CJ. Adams, M.J. Earle, G. Roberts, K.R. Seddon, Chem. Commun. (1998) 2097-2098.

[2] W. Chen, L. Xu, C. Chatterton, J. Xiao, Chem. Commun. (1999) 1247-1248.

[3] C.W. Lee, Tetrahedron. Lett. 40 (1999) 2461-2462.

[4] D.G. Stevenson, A. Biswas, J. Jane, G.E. Inglett, Carbohyd. Polym. 67 (2007) 21-31.

[5] C. Tsioptsias, C. Panayiotou, Carbohyd. Polym. 74 (2008) 99-105.

[6] K. Huang, J. Xia, M. Li, J. Lian, X. Yang, G. Lin, Carbohyd. Polym. 83 (2011) 1631-1635.

[7] O. Aaltonen, O. Jauhiainen, Carbohyd. Polym. 75 (2009) 125-129.

[8] J. Kadokawa, M. Murakami, A. Takegawa, Y. Kaneko, Carbohyd. Polym. 75 (2009) 180-183.

[9] X. Hu, K. Hu, L. Zeng, M. Zhao, H. Huang, Carbohyd. Polym. 82 (2010) 62-68.

[10] L. Viau, C. Tourné-Péteilh, K. M. Devoisselle, A. Vioux, Chem. Commun. 46 (2010) 228-230.

[11] E. Rozniecka, G. Shul, J.S. Plenet, L. Gaillon, M. Opallo, Electrochem. Commun. 7 (2005) 299-304.

[12] P. Barpanda, J. N. Chotard, C. Delacourt, M. Reynaud, Y. Filinchuk, M. Armand, M. Deschamps, J.M. Tarascon, P. Barpanda, Angew. Chem. Int. Edit. 50 (2011) 2526-2531.

[13] P. Barpanda, R. Dedryvère, M. Deschamps, C. Delacourt, M. Reynaud, A. Yamada, J.M. Tarascon, J. Solid. State. Electr. 16 (2012) 1743-1751.

[14] S. Kuwabata, A. Kongkanand, D. Oyamatsu, T. Torimoto, Chem. Lett. 35 (2006) 600-601.

[15] T. Torimoto, K. Okazaki, T. Kiyama, K. Hirahara, N. Tanaka, S. Kuwabata, Appl. Phys. Lett. 89 (2006) 243117.

[16] S. Arimoto, M. Sugimura, H. Kageyama, T. Torimoto, S. Kuwabata, Electrochim. Acta. 53 (2008) 6228-6234.

[17] S. Kuwabata, T. Tsuda, T. Torimoto, J. Phys. Chem. Lett. 1 (2010) 3177-3188.

[18] Y. Ishigaki, Y. Nakamura, T. Takehara, T. Shimasaki, T. Tatsuno, F. Takano, Y. Ueda, Y. Motoo, T. Takegami, H. Nakagawa, S. Kuwabata, N. Nemoto, N. Tomosugi, S. Miyazawa, Microsc. Res. Tech. 74 (2011) 1024-1031.

[19] Y. Ishigaki, Y. Nakamura, T. Takehara, N. Nemoto, T. Kurihara, H. Koga, H. Nakagawa, T. Takegami, N. Tomosugi, S. Miyazawa, S. Kuwabata. Microsc. Res. Tech. 74 (2011) 415-420.

[20] K. Yanaga, N. Maekawa, N. Shimomura, Y. Ishigaki, Y. Nakamura, T. Takegami, N. Tomosugi, S. Miyazawa, S. Kuwabata, Micol. Progress. 11 (2011) 343-347.

[21] A. Dwiranti, L. Lin, E. Mochizuki, S. Kuwabata, A. Takaoka, S. Uchiyama, K. Fukui. Microsc. Res. Tech. (2012) accepted.

[22] K. Kawai, K. Kaneko, H. Kawakami, T. Yonezawa, Langmuir 27 (2011) 9671-9675.

[23] C. Takahashi, T. Shirai, M. Fuji, Mater Chem Phys. 135 (2012) 681-686.

[24] C. Takahashi, T. Shirai, M. Fuji, Sol. Sta. Ionics. (2012) submitted.

CHAPTER 5

MICROSCOPIC OBSERVATION OF MONTMORILLONITE SWELLED BY WATER WITH THE AID OF HYDROPHILIC IONIC LIQUID

5. 1. Introduction

The present author earlier reported that the exact morphology of wet agar gel and hydrated porous hydroxyapatite (HAp) green body can be observed using FE-SEM with the aid of hydrophilic IL, and, proposed an observation mechanism for water containing materials in vacuum condition. It was reported that for optimum water concentration, IL and water molecules within these samples form weak hydrogen bond such as BF_4^- $\cdots HOH \cdots BF_4^-$ which helps to retain the morphology in wet condition even under vacuum condition. In addition, we reported that observation mechanism of biomaterials was different from above materials and we optimized the observation method using seaweed with the aid of hydrophilic IL [1].

Clay minerals are widely used in daily life due to their abundant resources, easy availability, high sorption, ion exchange properties and low cost. Generally, clays exist as layer structures and used as host materials for fabricating hybrid composites [2]. There are many kinds of clays such as smectites, kaolinite, mica, vermiculite, pylophyllite and

sepiolite etc. Among them, montmorillonite is popularly known clay of several applications due to its large surface area and high cation exchange capacity [3]. Layer structures of montmorillonite assists water to easily draw into the interlayer space between the sheets and cause the clay to swell dramatically [4, 5]. Because of this unique behavior, inorganic clay - organic intercalation compounds have been widely researched for past several decades [6-8]. In order to examine the intercalation behavior, recently, swelling structure of aqueous montmorillonite are reported to be observed using cryo TEM [9]. However, this observation method takes longer time for sample preparation. Therefore, new method for observation of hydrous montmorillonite needs to be developed.

In the present work, the morphology of hydrous montmorillonite in different swelling conditions with the aid of hydrophilic IL is reported using FE-SEM and TEM. The behavior of IL and water within hydrated montmorillonite is studied by XRD and the results are compared with the TEM-SAED to confirm the displacement of IL and water molecules within the hydrous montmorillonite.

5. 2. Materials and methods

5. 2. 1. Materials

Na-montmorillonite (Kunipia-F®, Kunimine Industries Co., Japan) was prepared after dried in an oven at 130 °C for 3 days. Density, CEC and electric conductivity of the montmorillonite are 2.65 g / cm^3 (Ultrapicnometer1000, Qurntachrome Instruments Co., Japan), 119 meq / 100 g clay and 3.43 mS / cm, respectively [10, 11]. Structural formula of purified montmorillonite can be written as: $Na_{2/3}Si_8(Al_{10/3}Mg_{2/3})O_{20}(OH)_4$.

The ionic liquid 1-butyl-3-methylimidazolium tetrafluoroborate (BMIM)(BF_4) (Kanto Chemical Co., Japan) was used after drying in a vacuum desiccators at 60 °C for 1 day; Water content was less than 128 ppm. Two types of hydrous montmorillonite in different swelling conditions were prepared. In first type, dried montmorillonite powder was kept in a humid chamber with 50 % humidity at 25 °C for 6 hrs and is described as *AM*. In second type, dried montmorillonite powder was mixed with ultrapure water (amount weight ratio; montmorillonite : water = 1 : 1.5) and is described as *BM*. It is noted that *AM* is powder-like condition and *BM* is paste-like condition.

5. 2. 2. Methods

The samples prepared in two different conditions as described in section 2.1 were characterized using optical microscope (KEYENCE, VHX-200, Japan) and field emission scanning electron microscope (FE-SEM, JEOL, JEM 7600F, Japan) with accelerating voltage of 5.0 kV. First, the *AM* and *BM* samples were observed with optical microscope at the atmosphere owing to obtain natural morphology. Subsequently, sample of *AM* and *BM* were treated with IL solution in the amount ratio of 1:30 and first kept in dessicator for 2 h, and then under vacuum condition for 24 h. Excess IL around sample was removed by centrifuged in rotation speed of 10000 revolutions per minutes (rpm). Now these two types of hydrous montmorillonite treated with IL solution are designated as AM_{IL} and BM_{IL}, respectively. The FE-SEM images of montmorillonite treated with IL were compared with optical microscope images. The morphologies of the montmorillonite powder were observed as a reference using optical microscope and FE-SEM. When using FE-SEM,

montmorillonite powder was coated by osmium metal while no coating was used for optical observation.

The size retention of the *BM* was measured both before and after the IL treatment. The dimensions of the samples were measured using a ruler as shown in Figure 5. 1. The size retention ratios were calculated (X × Y × Z / 125 × 100). In this study, size retention of *AM* could not be measured due to its powder form.

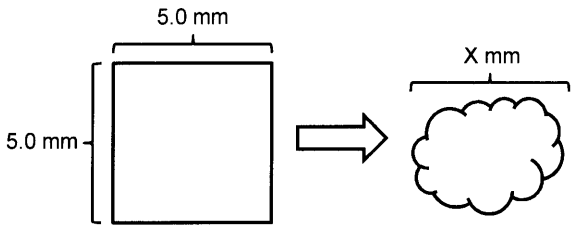

Figure. 5. 1. Size measurement of the *BM* after the IL treatment.

Mineralogical data of montmorillonite was observed by X-ray diffraction (XRD) (Ultima 5, Rigaku Co., Japan). XRD patterns of the powders were recorded in the 2θ range of 5 to 60° with a scan speed of 2° / min using Cu Kα radiation (λ = 0.1542 nm, 40 kV, 40 mA) and a proportional counter detector. XRD pattern of *BM* was recorded in the 2θ range of 2 to 60° due to its swelling behavior. For XRD observation, both *BM* and BM_{IL} samples were crushed and excess IL was removed.

Thus prepared AM_{IL} and BM_{IL} samples were observed using a TEM (JEM2010, JEOL Co., Japan) operated at 120 kV. For comparison, dried montmorillonite was also observed in a similar condition under TEM. The montmorillonite powder for TEM observation was dispersed in ethanol and skimmed off by a copper mesh with carbon-

coated plastic microholes, while the samples of AM_{IL} and BM_{IL} were also dispersed in ethanol (amount weight ratio; AM_{IL} or BM_{IL}: ethanol = 1 : 50).

5. 3. Results and discussions

5. 3. 1. Morphological observation of dried montmorillonite powder by optical microscope and FE-SEM.

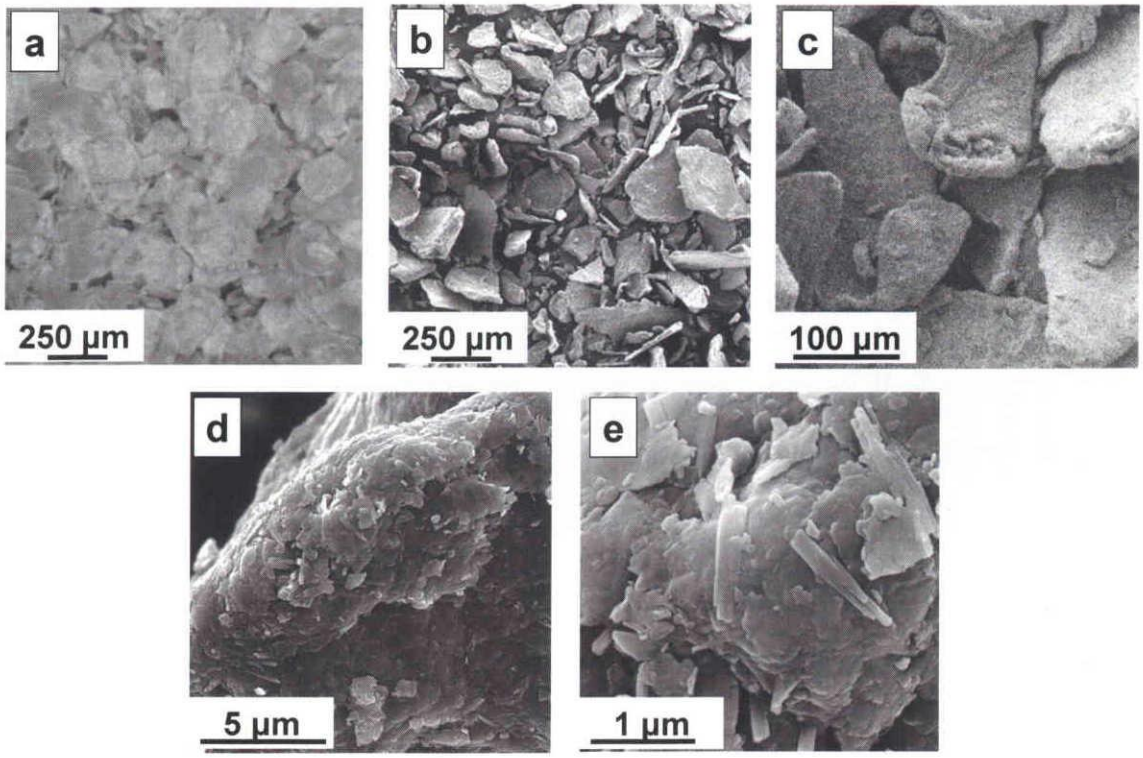

Figure. 5. 2. Optical microscope image of dried montmorillonite powder (a), FE-SEM images of dried montmorillonite powder coated by Osmium metal (b)- (e). The accelerating voltage for FE-SEM observation was 5.0 kV.

In order to compare the change in morphology of hydrous montmoriilonite in different swelling conditions, first the morphology of dried montmorillonite powder was observed as a reference. Figure 5. 2a shows optical microscope and Figure 5. 2b-e shows FE-SEM images of dried montmorillonite powder. From optical microscope and FE-SEM image in Figure 5. 2a and b, there was no significant difference although focus depth are different. We could observe montmorillonite powders below 300 μm in size. Figure 5. 2b-e shows FE-SEM images of dried montmorillonite powder in different magnification. Although it is difficult to observe fine structure at low magnification, the layer structure of montmorillonite was observed at high magnifications.

5. 3. 2. Morphological observation of *AM* by optical microscope and FE-SEM.

Figure 5. 3 shows optical microscope and FE-SEM images of *AM* sample in powder-like condition. Figure 5. 3a and b shows comparison of optical microscope images of *AM* before and after IL treatment. Results showed that the morphology of *AM* could be observed without any change even after subjected to IL treatment. Powders below 300 μm in size could be observed similar to dried montmorillonite powder (Figure 5. 2b). *AM* sample could be observed without any change even in FE-SEM chamber under vacuum condition (Figure 5. 2c-f). Although particle morphology in Figure 5. 3d appeared similar to Figure 2c, we can find significant difference between dried montmorillonite powder and *AM* at high magnification (Figure 5. 3e-f and Figure 5. 2d-e). In comparison with that of the dried montmorillonite powder, small layers were drastically decreased and edge of the layers were scaled after keeping in a humid chamber (50 % humidity) at 25°C for 6hrs

(Figure 5. 3e). Moreover, at high magnification expanded interlayer could be clearly observed (Figure 5. 3f) though there is no significant difference between dried montmorillonite powder and *AM* at low magnification.

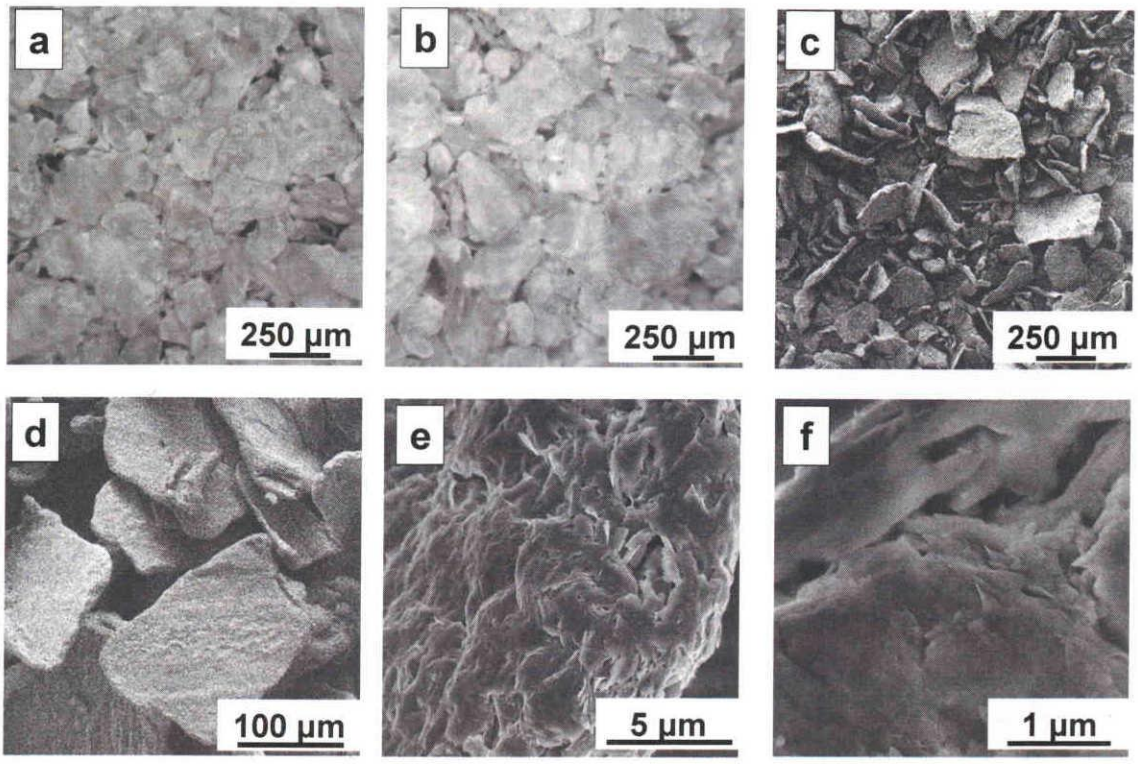

Figure. 5. 3. Optical microscope images of *AM* (a) and AM_{IL} (b), FE-SEM images of AM_{IL} (c)-(f). The accelerating voltage for FE-SEM observation was 5.0 kV.

Thus, the morphology of *AM* (powder-like condition) showed little change as compared to as-received montmorillonite powder due to the sample kept in humid chamber. Interestingly, the sample could be observed by FE-SEM under high vacuum subjected to IL treatment. However, it is important to compare the morphological change when the

montmorillonite powder is prepared in paste-like condition (BM) where water content is large.

5. 3. 3. Morphological observation of *BM* by optical microscope and FE-SEM.

Figure 5. 4a-f shows optical microscope and FE-SEM images of *BM* which is hydrous montmorillonite in paste-like condition.

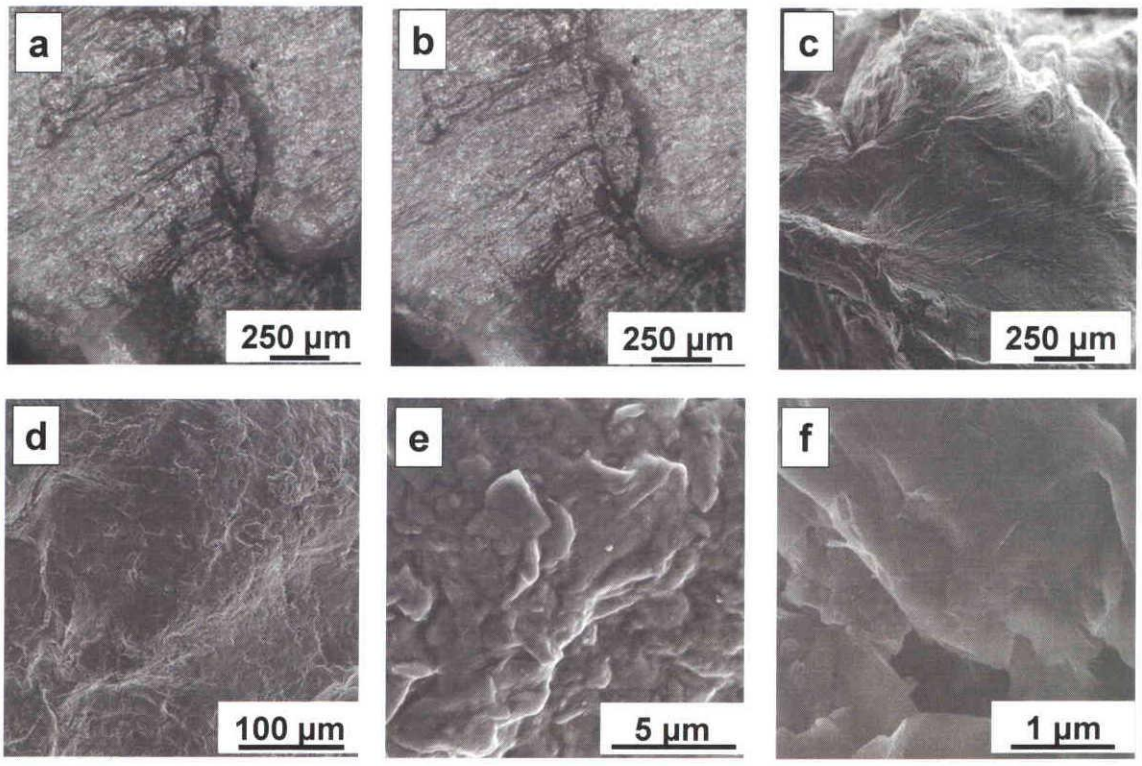

Figure. 5. 4. Optical microscope images of *BM* (a) and BM_{IL} (b), FE-SEM images of BM_{IL} (c)- (f). The accelerating voltage for FE-SEM observation was 5.0 kV.

Figure 5. 4a and b shows optical microscope image of *BM* at the same position before and after IL treatment. Results showed that the morphology of *BM* was not changed even after

subjected to IL treatment. Figure 5. 4c shows FE-SEM image of *BM* after IL treatment. Although there is difference of focus depth, surface morphology of *BM* after IL treatment (Figure 5. 4c) was very similar to *BM* before IL treatment (Figure 5. 4a). We can observe the surface morphology of kneaded mixture of montmorillonite and water. This paste-like morphology (*BM*) is significantly different as-compared to that of powder-like morphology (*AM*). From high magnification images, we can see swelling morphology with large number of agglomerate and appeared to be thick layer structure compared to *AM* sample.

Table 5. 1. Size retention of BM_{IL} hydrous montmorillonite before and after IL treatment.

Condition	Size retention (%)
Before IL treatment	100.0
After IL treatment	98.5

Table 5. 1 shows an examination of size retention of *BM* before and after IL treatment. Results showed that *BM* retained its size above 98 %. This indicates that the morphology of *BM* could be maintained despite of IL treatment.

Thus, from Figure 5. 2-4 we could see the gradual change in morphologies of montmorillonite powder from its dry condition to paste-like condition. Surface morphology of hydrous montmorillonite could be clearly observed when the sample is subjected to IL treatment without any charging. This indicates that the IL used in the present study serve as a conductive surface similar to osmium or carbon coating. However, it is essential to further

investigate the swelling behavior of montmorillonite powder (*AM* and *BM*) subsequently treated with IL solution.

5. 3. 4. Swelling behavior of hydrous montmorillonite treated with IL.

Figure 5. 5 shows the comparison of XRD patterns of dried montmorillonite (as a reference) and montmorillonite in two different conditions i.e. powder-like *(AM)* and paste-like *(BM)* and subsequently subjected to IL treatment (AM_{IL} and BM_{IL}). It can be seen in Figure 5. 5a that a (001) reflection (9.62 Å), (002) reflection (4.79 Å) and (020) reflection (4.44 Å) of the montmorillonite constituent and a little sharp reflection at 2θ values 26.77 (3.33 Å) correspond to the quartz that was used as an external component [12]. It has been reported that the interlayer distance at (001) reflection of montmorillonite is around 9.6 Å when no water molecules are intercalated between the unit layers [13] and the result is in good agreement with the present XRD data. Figure 5. 5b shows XRD patterns of *AM* and AM_{IL} for comparing the swelling behavior of montmorillonite swelled by small amount of water in humid chamber and subjected to IL treatment. It can be seen in *AM* that a (001) reflection (12.58 Å), (002) reflection (6.25 Å) and (020) reflection (4.26 Å) of the montmorillonite constituent and a little sharp reflection at 2θ values 26.68 (3.35 Å) correspond to the quartz. From XRD patterns of AM_{IL}, we can see that (001) reflection (13.97 Å), (002) reflection (6.99 Å) and (020) reflection (4.69 Å) were shifted. As-compared with *AM*, the (001) d-spacing values of intercalation compound showed a remarkable increase from 12.58 Å to 13.97 Å. These d-spacing values of AM_{IL} is in good agreement with the value of M_{IL} intercalated compound prepared by simple mixing of both

montmorillonite and IL [(BMIM)(BF_4)] in our work (See in chapter 6). This indicates that IL was displaced with water molecules within *AM*, hence $(BMIM)^+$ cation part of IL was inserted into interlayer space of montmorillonite.

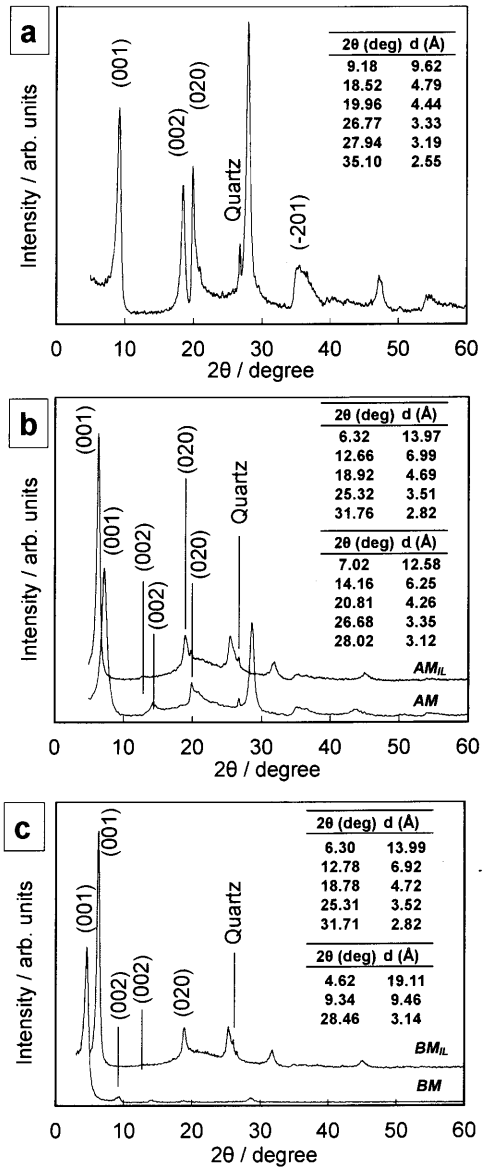

Figure. 5. 5. XRD patterns of (a) dried montmorillonite powder, (b) *AM*, AM_{IL} and (c) *BM*, BM_{IL}. The list shows d-spacing of each XRD peaks.

Figure 5. 5c shows the XRD patterns of *BM*, BM_{IL} for comparing the swelling behavior of montmorillonite swelled by large amount of water before and after IL treatment. It can be seen in *BM* that a (001) reflection (19.11 Å) and (002) reflection (9.46 Å) of the montmorillonite constituent. In the XRD patterns of *BM*, (001) reflection is quite strong, hence other reflections became weak. From XRD patterns of BM_{IL}, we can see that (001) reflection (13.99 Å), (002) reflection (6.92 Å) and (020) reflection (4.72 Å) were shifted. As-compared with *BM*, the (001) d-spacing values of intercalation compound showed a remarkable change from 19.11 to 13.99 Å. Interestingly, d-spacing values of BM_{IL} are very similar to AM_{IL} although both of them were in different hydrous condition. From these results, it is considered that displacement of IL and water molecules took place when hydrous montmorillonite was treated with IL solution.

Therefore, d-spacing of hydrous montmorillonite treated with IL was changed due to the size of $(BMIM)^+$ cation part of IL. Even BM_{IL} in hydrous montmorillonite swelled by large amount of water + IL treatment, displacement of IL and water molecules has also occurred. Moreover, it is expected that $(BMIM)^+$ cation exist in the montmorillonite interlayer as one layer from XRD results. However, the morphology of *BM* was not drastically changed (see in Figure 5. 4). Therefore, we need to confirm the hydrous montmorillonite morphology using TEM including SAED.

5. 3. 5. Swelling structure of hydrous montmorillonite treated with IL.

Figure 5. 6 shows TEM image and its corresponding SAED pattern of the dried montmorillonite powder. Thin layer structure can be observed in low magnification image

(Figure 5. 6a-b). Figure 5. 6c shows the layer structures consisting of fine strips, and it is well known that the layer spacing change significantly when intercalate with the organic or inorganic molecules. The d-spacing of the montmorillonite and quartz is indexed in the Debye ring (Figure 5. 6d).

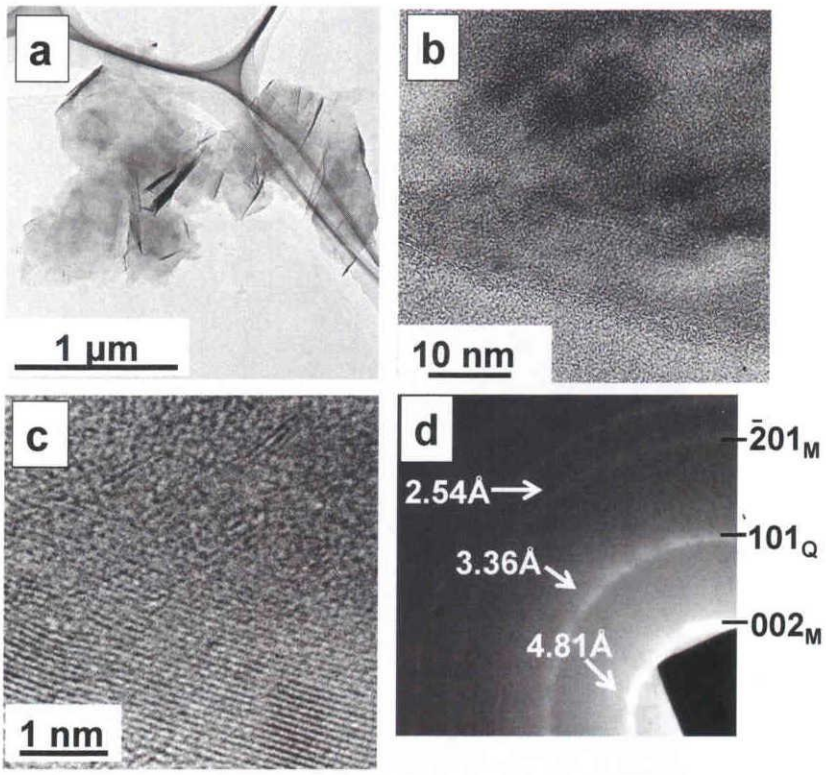

Figure. 5. 6. TEM images of dried montmorillonite powder (a), (b) bright-field image, (c) SAED pattern in which the Debye rings are indexed (d). The subscript M is derived from montmorillonite and Q from quartz.

Figure 5. 7 shows the TEM images and its SAED pattern of the AM_{IL} sample. Figure 5. 7a shows the structure consists of the swelled-like area. From the contrast it can be easily

visualize the thickness of the sample. Figure 5. 7b shows that interlayer space of AM_{IL} was increased remarkably when the montmorillonite powder was kept in humid chamber for 6h.

From high-resolution observation, we can confirm that the d-spacing of crystal in this area is 3.5 Å. It is considered that AM_{IL} maintained the crystal structure despite montmorillonite was swelled by small amount of water + treated with IL (Figure 5. 7c). From the Debye ring which indicates randomly oriented crystallites, the each d-spacing from montmorillonite was calculated and is shown in Figure 5. 7d.

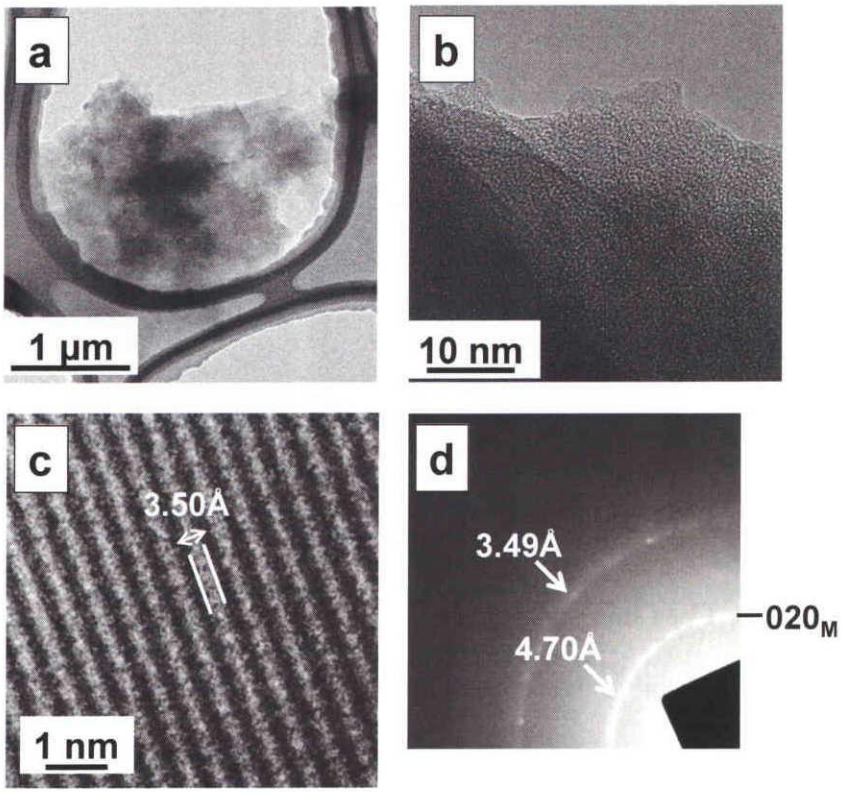

Figure. 5. 7. TEM images of AM_{IL} bright-field image (a), (b), high-resolution image (c), and SAED pattern in which the Debye rings are measured (d). The subscript M is derived from montmorillonite.

Figure 5. 8 shows the TEM images and its SAED patterns of the BM_{IL} sample. It can be seen in Figure 5. 8a that the structure consists of the swelled-like area. We can observe the swelled structure with black contrast.

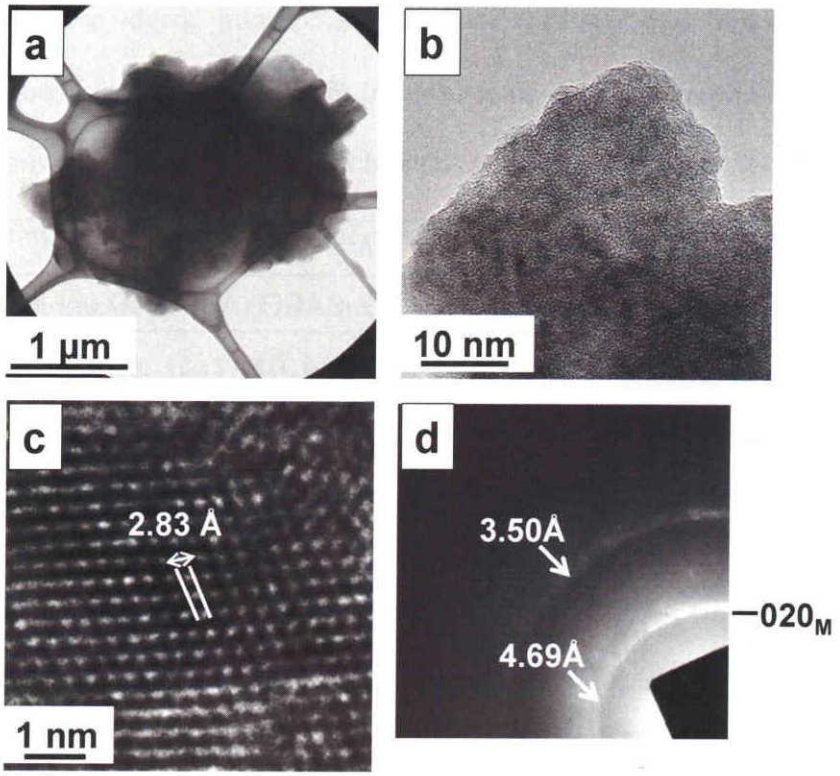

Figure. 5. 8. TEM images of BM_{IL} bright-field image (a), (b), high-resolution image (c), and SAED pattern in which the Debye rings are measured (d). The subscript M is derived from montmorillonite.

Figure 5. 8b shows the morphology which has large interlayer due to swell by large amount of water. High-resolution observation confirmed that the d-spacing of crystal in this area is 2.83 Å. The crystal structure of BM_{IL} could be successfully observed despite montmorillonite was swelled by large amount of water + treated with IL (Figure 5. 8c).

From the Debye ring, the each d-spacing of montmorillonite was calculated and is shown in Figure 5. 8d. Thus comparing BM_{IL} and AM_{IL}, we can see that TEM images were largely different although SAED results were very similar.

Table 5. 2. Comparison of d-space of dried montmorillonite, hydrous montmorillonite AM_{IL} and BM_{IL} as obtained from XRD and SAED results.

Dried Montmorillonite		AM_{IL}		BM_{IL}	
XRD (Å)	SAED (Å)	XRD (Å)	SAED (Å)	XRD (Å)	SAED (Å)
4.79	4.81	4.69	4.70	4.72	4.69
3.33	3.36	3.51	3.49	3.52	3.50
2.55	2.54	2.82	2.80	2.82	2.83

Comparing the SAED and XRD results (see Table 5. 2), the d-spacing did not show any significant difference. Therefore, the correct morphology and structure of AM_{IL} and BM_{IL} could be observed using FE-SEM and TEM. However, main purpose of the present study is to visualize the correct morphology and structure of *AM* and *BM* as hydrous montmorillonite with the aid of IL. Therefore, we need to further investigate the behavior of IL and hydrous montmorillonite for both the conditions. From d-spacing values, it is expected that cation part of IL is arranged within the interlayer space with fixed displacement when hydrous montmorillonite was treated by IL. Thereby, it is considered that observation of the exact morphology of hydrous montmorillonite is difficult. However, FE-SEM results and size retention showed that the morphology was not drastically changed after IL treatment.

Legaly et al reported that the edge charge density of montmorillonite is low and negative when pH of mixture is above 6.0 [14]. On the other hands, the basal surface charge density remained positive. It is well known that cardhouse-like structure is formed by interaction between edge as minus charge and face as plus charge. In our present study, we used water (pH=7.0) and IL (pH=9.02). Therefore, the cardhouse-like structure was formed within hydrous montmorillonite, and, the cardhouse-like structure further remained even in hydrous montmorillonite subjected to IL treatment. This cardhouse-like structure enables to maintain the morphology of hydrous montmorillonite after IL treatment. Although ultrafine structure may have a little different d-spacing values, skeleton structure of hydrous montmorillonite is considered to be maintained.

5. 3. 4. Conclusions

The morphology and structure of swelled montmorillonite by water in different swelling condition could be observed with the aid of hydrophilic IL using FE-SEM and TEM. From XRD and TEM-SAED results, it was concluded that IL was intercalated into the montmorillonite's interlayer by displacement of water molecules within montmorillonite. Despite the different swelling condition of hydrous montmorillonite, IL was intercalated within montmorillonite interlayer as fixed arrangement. In the case of montmorillonite which is swelled by small amount of water such as *AM*, it is consider that morphology and structure can be almost observe using IL although there is a little change of d-spacing by cation size of IL. On the other hands, in the case of montmorillonite which is swelled by large amount of water such as *BM*, it is consider that morphology and structure

can be almost observe using IL due to the card-like structure although the d-spacing was significantly changed. It is expected that such a technique would be useful in characterizing the morphology and structure of hydrous intercalated compounds by water in various swelling conditions.

References

[1] C. Takahashi, T. Shirai, M. Fuji, Micros. Res. Tech. (2012) accepted.

[2] F. Bergaya, B. K. G. Theng, G. Lagaly, Handbook of Clay Science, first ed., Elsevier, Amsterdam, 2006.

[3] M. Alkan, O. Demirbas, S. Celiks, M. Dogan, J. Hazardous. Mater. 116 (2004) 135-145.

[4] K. Norrish, Discuss. Faraday. Soc. 18 (1954) 120-134.

[5] H.A. Alawaji, Appl. Clay Sci. 15 (1999) 411-430.

[6] M. Ogawa, Langmuir. 11 (1995) 4639-4641.

[7] S. Letaief, C. Detellier, J. Mater. Chem. 17 (2007) 1476-1484.

[8] E. Ruiz-Hitzky, P. Aranda, J. M. Serratosa, M. Auerbach, K. Carrado, P. K. Dutta (Eds.), Handbook of Layered Materials, Marcel Dekker, Inc. New York, 2004, pp. 91-154.

[9] M. Segad, S. Hanski, U. Plsson, J. Ruokolainen, T. Akesson, B. G. Jonsson, J. Phys. Chem. C. 116 (2012) 7596-7601.

[10] M. Ogawa, T. Aono, K. Kuroda, C. Kato, Langmuir. 9 (1993) 1529-1533.

[11] T. Okada, Y. Ehara, M. Ogawa, Clays. Clay. Miner. 55 (2007) 348-353.

[12] R. Miyawaki, T. Sano, F. Ohashi, M. Suzuki, T. Kogure, T. Okumura, J. Kameda, T. Umezome, T. Sato, D. Chino, K. Hiroyama, H. Yamada, K. Tamura, K. Morimoto, S. Uehara, T. Hatta, Nendo Kagaku. 48 (2010) 158-198.

[13] R. E. Grim, Clay mineralogy, McGraw-Hill, New York, 1953.

[14] G. Legaly, Appl. Clay. Sci. 4 (1989) 105-123.

CHAPTER 6

APPLICATION OF INTERCALATED COMPOUNDS OF MONTMORILLONITE AND VARIOUS IONIC LIQUID

6. 1. Introduction

In Chapter 4, fine structure of the hydrous montmorillonite in different swelling conditions was successfully observed with the aid of hydrophilic IL [1]. From these studies, it was concluded that IL was intercalated into montmorillonite's interlayer by displacement of water molecules within montmorillonite. The high selectivity of IL with montmorillonite's interlayer was revealed and which is attractive for extending to a fabrication of organic-inorganic electrically conductive materials.

Clay minerals are very often used in our daily life due to their abundant resources, high sorption, ion exchange properties and low cost. These clays exist as layer structures and used as host materials for fabricating hybrid composites [2]. Layer structures of montmorillonite helps water to easily draw into the interlayer space between sheets and causes the clay to swell dramatically. Because of this unique behavior, inorganic clay - organic intercalation compounds have been widely researched for past several decades. The intercalation mechanisms are explained through electrostatic interactions, secondary bonding or covalent bonding. Based on these concepts, many researchers fabricated inorganic clay-organic intercalated compounds that could have specific properties such as

mechanical strength, thermal stability, photoluminescence and catalysis [3-9]. In these methods, organic molecules containing cations can easily infiltrate into the interlayer of inorganic clays [10, 11]. Among various applications, thermal stability of clay – organic compound have been provided by improving physical properties and reducing flammability [12-14]. Ionic liquid (IL) modified clays are recently paid attention due to ILs unique properties such as negligible vapor pressure, nonflammabilities and electrical conductivity for fabricating inorganic clay - organic intercalation compounds with high thermal stability and composite materials with improved flame retardant property. Some reports were focused on the applications of ILs intercalated clay, such as catalysis [15], nano composites [16-18]. However, most of the cases intercalation was carried out using polymer and IL together. In addition, some reports were focused on the intercalation of clay by various ILs [19-22]. However, organic compound or solvent such as water and ethanol were used for preparation for IL intercalation. In this study, we focused on IL intercalation into clay without any compound and solvent due to discover more convenient and eco-friendly method.

ILs are molten salts, remain liquid at room temperature and frequently used as solvent in various chemical reactions [23-25], electrolyte in batteries [26] and dispersant [27, 28] etc. They contain cations and anions and exist as colorless fluid and show high electric conductivity [29-32]. IL composite materials could be observed under an electron microscope without any conducting coating due to their transparency, electric conductivity and negligible vapor pressure [33, 34]. It was also reported that wet materials with hydrophilic IL could be observed in SEM [35]. Especially, we have successfully observed

the morphology and structure with nano scale of hydrated montmorillonite using IL without cryo TEM [1].

In recent years, transparent electrically conducting thin films such as Indium tin oxide (ITO) and Antimony tin oxide (ATO) are useful for a solar battery, liquid crystal and organic electroluminescence (EL) display [36-38]. However, other possible materials for transparent electrically conducting thin films are still being researched.

In this study, direct intercalation of IL into montmorillonite (*M*) is attempted and fabricated M_{IL} intercalated compounds using four kinds of ILs. Thus fabricated solid-liquid state M_{IL} intercalated compound is observed by TEM to understand the crystal swelling structure in liquid state. In addition, XRD results are compared with the TEM-SAED owing to confirm the structures of M_{IL} intercalated compounds. From cation exchange capacity, arrangement of cations in the interlayers of montmorillonite clay was proposed. Besides, sheet resistivity of M_{BMIMB} intercalated compound is examined in order to fabricate conducting thin film using IL and montmorillonite. Thermal stability of three kinds of M_{IL} intercalated compounds (M_{EMIO}, M_{TMPAT} and M_{DEMET}) was examined by TG-DTA.

6. 2. Materials and methods

6. 2. 1. Methodology of fabricating and characterization of M_{BMIMB} intercalated compound.

Na-montmorillonite (Kunipia-F®, Kunimine Industries Co., Japan) was dried in an oven at 130 °C for 3 days. Density and CEC of the montmorillonite are 2.65 g / cm^3 (Ultrapicnometer1000, Qurntachrome Instruments Co., Japan), 119 meq / 100 g clay,

respectively [3,39]. Structural formula of purified montmorillonite can be written as: $Na_{2/3}Si_8(Al_{10/3}Mg_{2/3})O_{20}(OH)_4$

The ionic liquid 1-butyl-3-methylimidazolium tetrafluoroborate ((BMIM)(BF_4)) (Kanto Chemical Co., Japan) was used after drying in a vacuum desiccators at 60 °C for 1 day; Water content < 128 ppm. M_{IL} intercalated compound was prepared by mixing the montmorillonite and IL in the weight ratio; 1:10, respectively.

The montmorillonite powder for TEM observation was dispersed in ethanol and skimmed off by a copper mesh with carbon-coated plastic microholes, while the sample of M_{IL} intercalated compound was also dispersed and removed excess IL around M_{IL} intercalated compound using ethanol (amount weight ratio; M_{IL}:ethanol = 1:50). In this study, we abbreviate the intercalated compounds montmorillonite-(BMIM)(BF_4) as M_{BMIMB}.

In order to measure the sheet resistivity of M_{BMIMB} intercalated compound, both montmorillonite and IL were first mixed in the same weight ratio; 1:10, respectively. The resultant M_{BMIMB} intercalated compound was subsequently dispersed in ethanol (amount weight ratio; M_{IL}:ethanol = 1:50), and, coated uniformly in the form of a thin sheet on quartz glass substrate using a spin coater (1H-D7, MIKASA Co., Japan) at a constant speed of 1000 rpm for 10 seconds and repeated for 10 times.

Mineralogical data of montmorillonite was observed by X-ray diffraction (XRD) (Ultima 5, Rigaku Co., Japan). XRD patterns of the powders were recorded in the 2θ range of 5 to 60° with a scan speed of 2° / min using Cu Kα radiation (λ = 0.1542 nm, 40 kV, 40 mA) and a proportional counter detector. For XRD observation, M_{BMIMB} intercalated

compound was prepared by putting in the desiccators for 1 min, 1, 2, 4, 6 h and subsequently excess IL was removed.

The CEC measurement of M_{BMIMB} intercalated compound was followed by Schollenberger [40]. The exchanged cations such as Na, K, Ca and Mg were leached by filtration using 1-N ammonium acetate solution, and measured by inductively coupled plasma (ICP) (SPS-7800, SII Co., Japan).

The prepared M_{BMIMB} intercalated compound was observed using a TEM (JEM2010, JEOL Co., Japan) operated at 120 kV equipped with an EDS. For comparison, dried montmorillonite was also observed in a similar condition.

The sheet resistivity of M_{BMIMB} intercalated compound prepared in the form of a thin sheet was measured on direct current source using four point probe method as shown in Figure 6. 1. Two of the four electrodes were connected to a current source (R6243, ADVANTEST Co., Japan) with 0.1, 0.5 and 1.0 mA, respectively. The other two electrodes were connected to a digital voltmeter (R6551, ADVANTEST Co., Japan) so that the voltage was measured manually. In this method, two consecutive measurements were performed by applying the current to two adjacent sides of the sample and the voltage was measured at each opposite side of the current contacts. Sheet resistivity (Ω / square) of the sample was calculated by the following equation,

$$\Omega / \text{square} = (\pi / \ln (2)) (V / I)$$

Where, $\pi / \ln (2)$; resistivity correction factor = 4.532. The current and voltage plot (I-V plot) was measured in order to observe the ohmic behavior of sample.

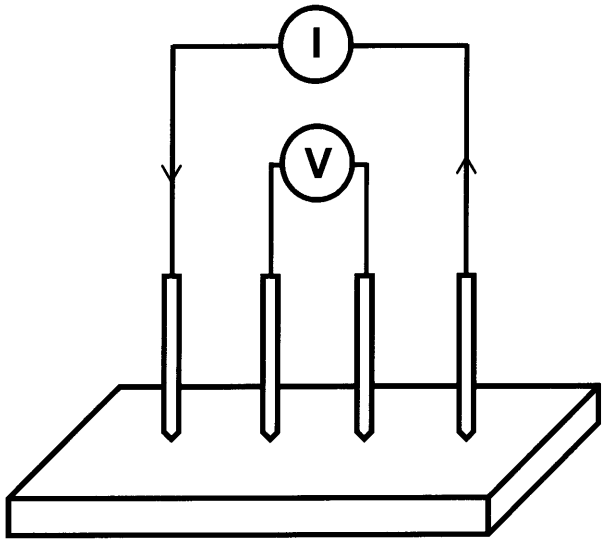

Figure. 6. 1. Schematic representation of measurement of sheet resistivity of M_{BMIMB} intercalated compound using four point probe method.

6. 2. 2. Methodology of fabricating and characterization of M_{EMIO}, M_{TMPAT} and M_{DEMET} intercalated compound.

Montmorillonite powder used as section 6. 2. 1. Three kinds of ionic liquids (ILs) 1-Ethyl-3-methylimidazolium octylsulfate (EMI)($OcSO_4$), N,N,N-Trimethyl-N-propylammonium bis (trifluoromethanesulfonyl) imide (TMPA)(TFSI) and N,N-Diethyl-N-methyl-N- (2-methoxyethyl) ammonium bis (trifluoromethanesulfonyl) imide (DEME)(TFSI) (Kanto Chemical Co., Japan) designated as EMIO, TMPAT and DEMET, respectively were used after drying in a vacuum desiccators at 60 °C for 3 days. Water content of all the three kinds of ILs is below 128 ppm. Montmorillonite and ILs intercalated compounds (M_{IL}) were prepared by mixing both of them in the amount weight ratio 1 : 2, respectively. In this study, we abbreviate three kinds of intercalated compounds

montmorillonite-(EMI)($OcSO_4$), montmorillonite-(TMPA)(TFSI) and montmorillonite-(DEME)(TFSI) as M_{EMIO}, M_{TMPAT} and M_{DEMET}, respectively.

Phase composition of montmorillonite and M_{IL} intercalated compound was observed by X-ray diffraction (XRD) (Ultima 5, Rigaku Co., Japan) in the 2θ range of 5 to 60° with a scan speed of 2° / min using Cu Kα radiation (λ = 0.1542 nm, 40 kV, 40 mA) and a proportional counter detector. Three kinds of M_{IL} compounds were prepared by mixing IL and montmorillonite and putting in the desiccators for 1 min and subsequently excess IL was removed. XRD of three kinds of remnant M_{IL} samples after TG-DTA measurement at 1000 °C were observed in the same 2θ range to examine the interaction of IL and montmorillonite.

The CEC measurement of three kinds of M_{IL} was followed by section 6. 2. 1. Thus, prepared three kinds of M_{IL} compound were observed using a TEM (JEM2010, JEOL Co., Japan) operated at 120 kV equipped with an EDS. For comparison, dried montmorillonite was also observed in a similar condition under TEM. The montmorillonite powder for TEM observation was dispersed in ethanol and skimmed off by a copper mesh with carbon-coated plastic microholes, while the sample of three kinds of M_{IL} was mixed with ethanol (amount weight ratio; M_{IL} : ethanol = 1 : 50) and taken out only supernatant and repeated for 5 times and skimmed off by a copper mesh for organic samples.

Thermo gravimetric - differential thermal analysis (TG-DTA) (Rigaku Co., Japan) of three kinds of M_{IL} intercalated compounds were carried out by putting the samples in an alumina pan and heated from RT to 1000 °C at a rate of 10 ° C / min under Ar gas flow.

6. 3. 1. Results and discussions

6. 3. 1. 1. Intercalation behavior of IL into the montmorillonite.

Figure 6. 2 shows the XRD patterns of dried montmorillonite (as a reference) and M_{BMIMB} intercalated compound. It can be seen in Figure 6. 2a that a (001) reflection (9.73 Å), (002) reflection (4.81 Å) and (020) reflection (4.49 Å) of the montmorillonite constituent and a little sharp reflection at 2θ values 26.59 (3.35 Å) correspond to the quartz that was used as an external component [41]. It has been reported that the interlayer distance at (001) reflection of montmorillonite is around 9.6 Å when no water molecules are intercalated between the unit layers [42] and the result is in good agreement with the present XRD data.

From Figure 6. 2b, (001) reflection (13.93 Å), (002) reflection (6.99 Å) and (020) reflection (4.67 Å) was clearly observed in the intercalation of IL into the montmorillonite layer. The un-indexed XRD peaks were not clearly identified because of impure substance and shift by swelling. Although many papers discuss about mainly small angle peaks such as basal plane peaks without high angle peaks, we measured high angle peaks for comparison with selected area electron diffraction (SAED) data in the present study. It should be noted here that the IL does not show any peak in XRD due to its liquid structure.

Compared to the intensity of (001) reflection of dried montmorillonite, intensity of (001) reflection of M_{BMIMB} intercalated compound was appeared to be stronger than the other reflection peaks. This reflects that IL enables to work for high orientation. As-compared with dried montmorillonite, we can see that the basal plane (001) has changed from 2θ value 9.08 to 6.34.This indicates that $(BMIM)^+$ ions (from IL) are successfully

intercalated into the interlayer of montmorillonite by a cation exchange process. This type of swelling, which shows limited d-spacing increase, has been called crystalline swelling.

Furthermore, XRD results with respect to time interval showed that IL is already intercalated into interlayer of montmorillonite within 1 min of mixing of the two and attained the saturation level, and, the same is indicated in Figure 6. 2c. From Table 1 we can see that d-spacing as well as peak shift of M_{BMIMB} intercalated compound was changed rapidly i.e. within 1 min and did not change regardless of time.

Table 6. 1. Comparison of d-spacing of the M_{BMIMB} intercalated compound at different time as measured by XRD.

M_{BMIMB}									
1 min		1 h		2 h		4 h		6 h	
2θ (deg)	d (Å)	2θ (deg)	d (Å)	2θ (deg)	d (Å)	2θ (deg)	d (Å)	2θ (deg)	d (Å)
6.34	13.93	6.39	13.82	6.37	13.86	6.36	13.88	6.32	13.97
12.66	6.99	12.74	6.95	12.64	6.98	12.78	6.89	12.98	6.92
18.99	4.67	18.90	4.69	18.91	4.69	18.91	4.69	18.94	4.68
25.41	3.50	25.35	3.51	25.34	3.51	25.32	3.51	25.29	3.52
31.82	2.81	31.79	2.81	31.70	2.82	31.76	2.82	31.82	2.81
35.08	2.56	35.28	2.55	35.32	2.54	35.07	2.56	35.06	2.56
45.22	2.00	45.22	2.00	44.96	2.02	44.98	2.01	45.01	2.01
53.86	1.70	53.87	1.70	53.96	1.70	54.05	1.70	54.29	1.69

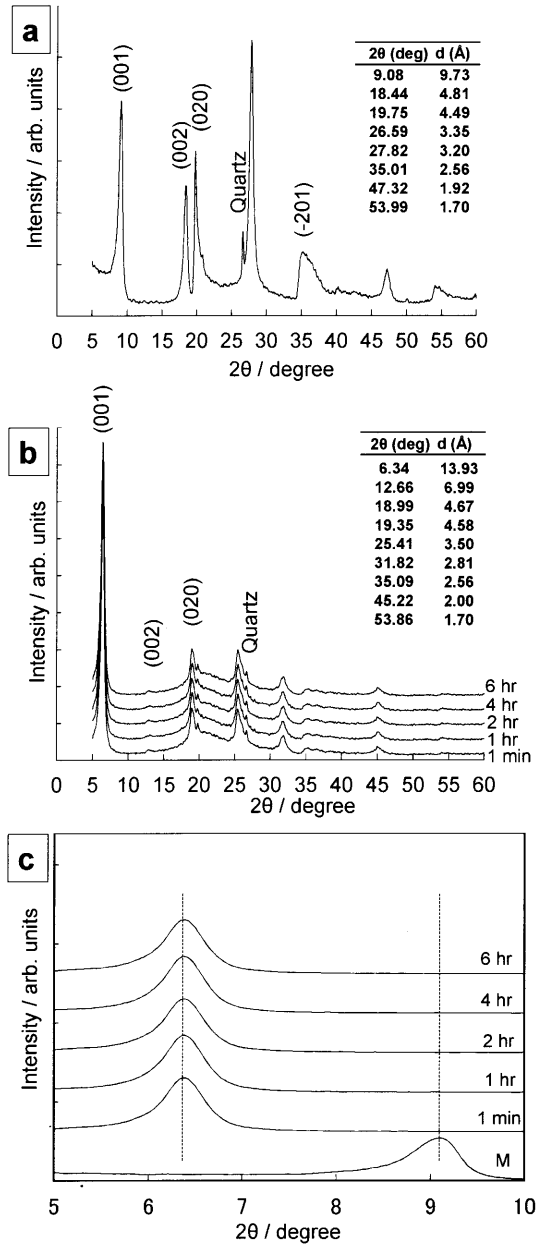

Figure. 6. 2. XRD patterns of dried montmorillonite (a) M_{BMIMB} intercalated compound (b) and basal plane (001) of dried montmorillonite and M_{BMIMB} intercalated compound in the range of 2θ from 5-10 (c) at different time. The list shows d-spacing of each XRD peaks. M indicates dried montmorillonite.

6. 3. 1. 2. Atomic arrangement of IL into the silicate layer of montmorillonite.

Table 6. 2. CEC of M_{BMIMB} intercalated compound with different mixing time.

Cations	M_{BMIMB}				
	1 min	1 h	2 h	4 h	6 h
Na^+	72.92	73.15	72.33	71.11	73.61
Mg^{2+}	2.71	2.68	2.83	2.76	2.82
K^+	0.93	0.92	0.97	0.93	0.97
Ca^{2+}	14.71	14.25	15.39	12.86	13.43
Total (meq / 100 g)	91.27	91.00	91.52	87.66	90.83

Table 6. 2 shows amounts of exchangeable cations in M_{BMIMB} intercalated compound with different mixing time. It can be seen that there was no significant differences in cation exchange between 1 min to 6 h of treatment. This indicates that exchange of the cation occurred very fast i.e. within 1 min. The total amounts of exchangeable cations were about 90.5 meq / 100g clay. This shows that the CEC of M_{BMIMB} intercalated compound was lower compared to the CEC of dried montmorillonite (CEC; 119 meq / 100g clay).

This indicates that the $(BMIM)^+$ ions of IL did not substitute whole amount of the interlayer exchangeable cations. From CEC and Avogadro number, the exchangeable cations and $(BMIM)^+$ ions are calculated to be 7.16×10^{22} / 100 g and 5.45×10^{22} / 100 g,

respectively. In other words, 23.88 % cations were remained un-exchanged. From literature we can see that the ionic radius of $(BMIM)^+$ is 3.30 Å [43-46]. The interlayer distance (4.33 Å) could be obtained by subtracting the thickness of silicate layer (9.6 Å) [39] from the observed basal spacing of M_{BMIMB} intercalated compound (13.93 Å). XRD results from the interlayer distance and the $(BMIM)^+$ diameter, the tilt angle (θ) of $(BMIM)^+$ ions into the interlayer of montmorillonite could be calculated using Wan et.al formula [5].

$$\Delta d = d_{001} - 0.96 = (\text{ionic length}) \sin\theta \quad (1)$$

where, ionic length is the diameter of $(BMIM)^+$ ion. From calculation using formula (1), the corresponding tilt angle of $(BMIM)^+$ was 41.0°. It is expected that the substituted $(BMIM)^+$ are arranged as a single ion which exist incline to the silicate layer.

Furthermore, the occupation of surface area of $(BMIM)^+$ toward silicate layer was also analyzed using CEC of M_{BMIMB} intercalated compound and montmorillonite in order to understand the arrangement of $(BMIM)^+$ ions into the layer. The surface area of silicate layer was calculated by Olphen method [47] and it was found to be 37446 m^2 / 100 g clay.

On the other hand, the area of $(BMIM)^+$ ions calculated using $(BMIM)^+$ area (0.342 nm^2) and numbers of $(BMIM)^+$ ions (5.45×10^{22} / 100 g). If all of the exchangeable cations are substituted by the $(BMIM)^+$ ions, the surface area of $(BMIM)^+$ ions would be 24500 m^2 / 100 g clay. Based on this calculation, it is concluded that the space of atomic arrangement is not narrow even though completely exchangeable cations substituted by the $(BMIM)^+$ ions. From these calculations, a schematic structure could be proposed for the present M_{BMIMB} intercalated compound and is shown in Figure 6. 3.

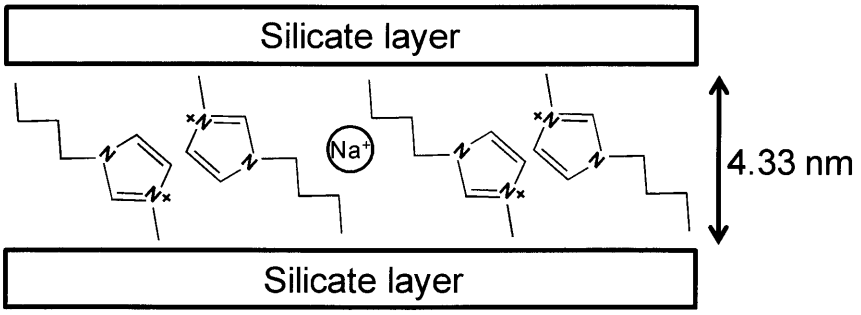

Figure. 6. 3. A proposed schematic structure of the M_{BMIMB} intercalated compound.

6. 3. 1. 3. Crystal swelling structure of M_{BMIMB} intercalated compound

Figure 6. 4 shows TEM image and its corresponding electron diffraction pattern of the dried montmorillonite. The layer structures of fine strips are seen in the high-magnification image (Figure 6. 4b), and it is well known that the layer spacing could change significantly when intercalated with an organic molecule. The d-spacing of the montmorillonite and quartz is obtained from the Debye ring and is shown Figure 6. 4c. Furthermore, mainly d-spacing was indexed.

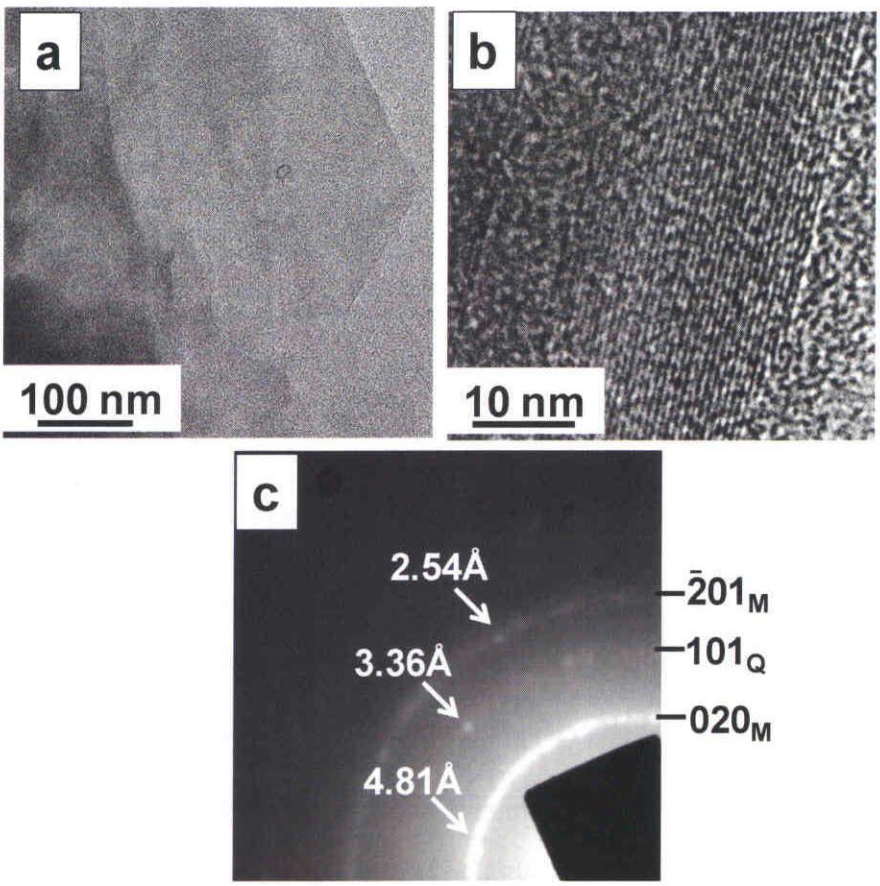

Figure. 6. 4. TEM images of dried montmorillonite bright-field image (a), (b) and SAED pattern (c) in which the Debye rings are indexed. The subscript M is derived from montmorillonite and Q from quartz.

Figure 6. 5 shows the TEM image and its SAED pattern of the M_{BMIMB} intercalated compound. It can be seen in Figure 6. 5a and b that the structure consists of the swelled-like area and maintains the crystal structure. High-resolution observation confirmed that the d-spacing of crystal in this area is 2.5 Å (Figure 6. 5c). Basically, lattice plane of crystalline M_{BMIMB} intercalated compound in Figure 6. 5c could be observed with 2.5 Å interstices. The

diffraction pattern can be interpreted as a mixture of randomly oriented crystallites of montmorillonite. From the Debye ring, each d-spacing of montmorillonite was calculated and is shown in Figure 6. 5d. SAED result corresponding to 2.56 Å d-spacing of Debye ring is in good agreement with analysis of lattice image. Thus, d-spacing analysis from lattice image and SAED patterns are very useful to confirm the correct morphology and intercalation of IL.

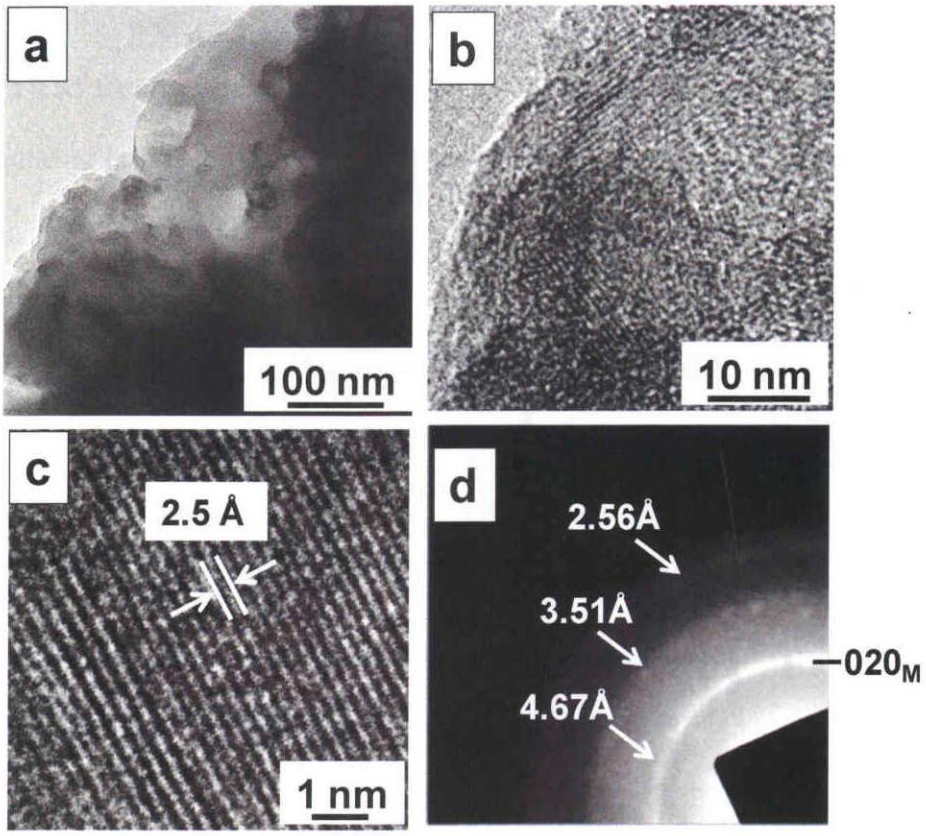

Figure. 6. 5. TEM images of M_{BMIMB} intercalated compound bright-field image (a), (b), high-resolution image (c), and SAED pattern (d) in which the Debye rings are measured. The subscript M is derived from montmorillonite.

TEM-EDS spectra of dried montmorillonite (as a reference) and M_{BMIMB} intercalated compound are shown in Figure 6. 6. It can be seen that the dried montmorillonite had well-known peaks such as Al, Si, Na, Mg, Ca etc (Figure 6. 6a). On the other hand, M_{BMIMB} intercalated compound showed strong C peak derived from cation part of IL and F peak derived from anion part of IL (Figure 6. 6b). Therefore, it can be further confirmed that IL was intercalated into the montmorillonite. From the XRD and SAED results (see Table 6. 3), the d-spacing did not show any significant difference, although diffraction patterns of (001) reflection were not observed for the reason of close to direct beam. These results suggest that we could successfully observe the nano-scaled crystal swelling structure of montmorillonite-ionic liquid intercalated compound using TEM.

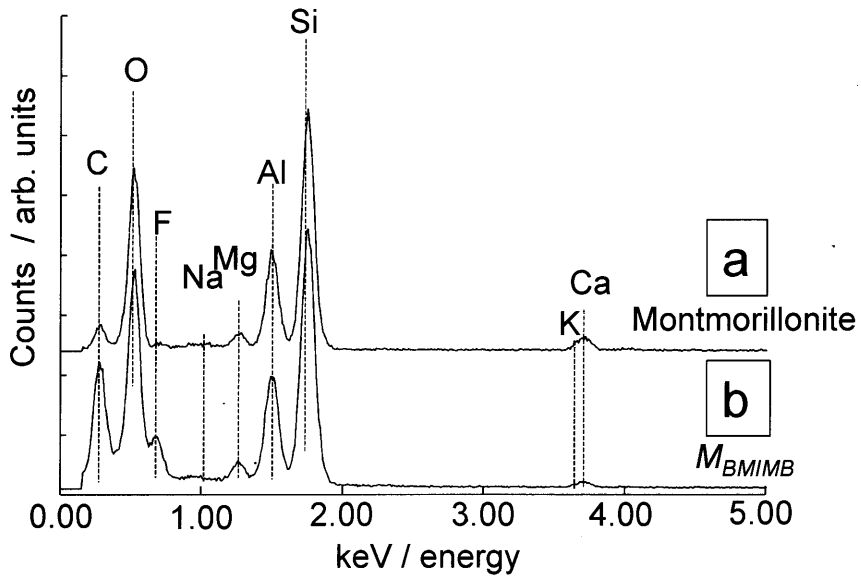

Figure. 6. 6. TEM-EDS spectra of dried montmorillonite (a) and M_{BMIMB} intercalated compound (b).

Table 6. 3. Comparison of d-spacing of dried montmorillonite and M_{BMIMB} intercalated compound as obtained from XRD and SAED.

Dried Montmorillonite		M_{BMIMB}	
XRD (Å)	SAED (Å)	XRD (Å)	SAED (Å)
4.808	4.813	4.670	4.667
3.35	3.362	3.502	3.509
2.561	2.542	2.556	2.56
1.922	1.912	2.004	2.031
1.697	1.701	1.701	1.705

6. 3. 1. 4. Sheet resistivity of M_{BMIMB} intercalated compound.

Figure 6. 7 shows the I-V plot with respect to different applied current (0.1, 0.5 and 1mA). It can be calculated from Figure 6. 7 that the sheet resistivity of raw IL to be 320.16 Ω / square, while M_{BMIMB} intercalated compound was 417.95 Ω / square. From the measurement we could see that montmorillonite-ionic liquid intercalated compound has about 70 % of sheet conductivity as compared to raw IL.

This result indicates the possibility of such an inexpensive material for its suitable application as a transparent electrically conducting thin film.

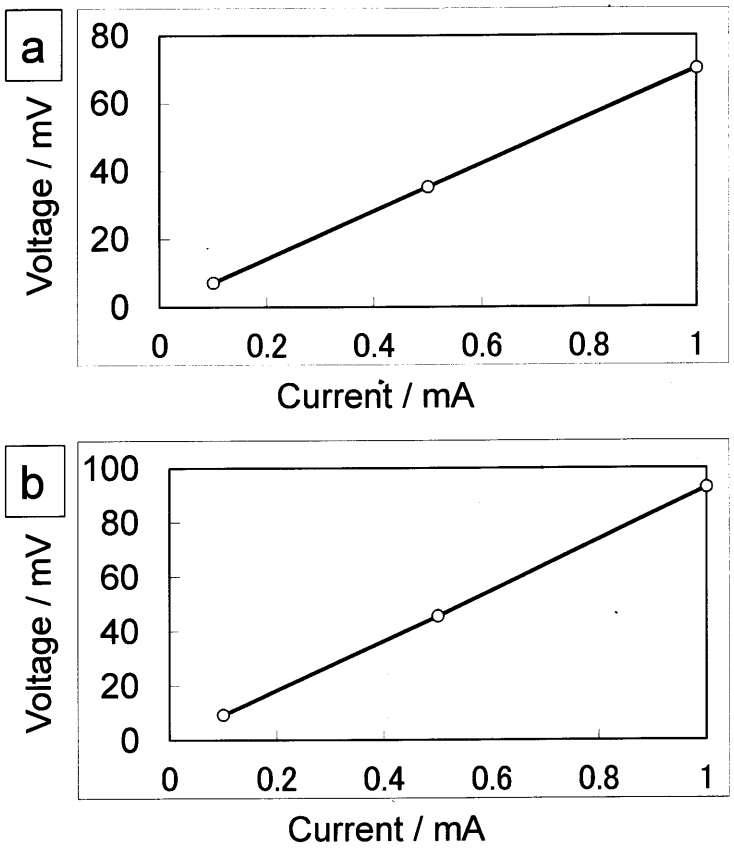

Figure. 6. 7. Measurement of voltage with respect to applied current (0.1, 0.5 and 1 mA) for IL (a) and M_{BMIMB} intercalated compound in the weight ratio 1:10 (b).

6. 3. 2. Results and discussions

6. 3. 2. 1. Intercalation behavior of ILs into the montmorillonite.

Figure 6. 8a-d shows the XRD patterns of dried montmorillonite powder (as a reference) and IL intercalated montmorillonite compounds M_{EMIO}, M_{TMPAT} and M_{DEMET}, respectively. It can be seen in Figure 6. 8a that (001), (002) and (020) reflection at 9.68 Å, 4.74 Å and 4.46 Å, respectively constituent of the montmorillonite powder and a sharp reflection at 2θ values 26.77 (3.33 Å) correspond to the quartz that was used as an external

component. It has been reported that the interlayer distance at (001) reflection of montmorillonite is around 9.60 Å when no water molecules are intercalated between the unit layers and the result is in good agreement with the present XRD data.

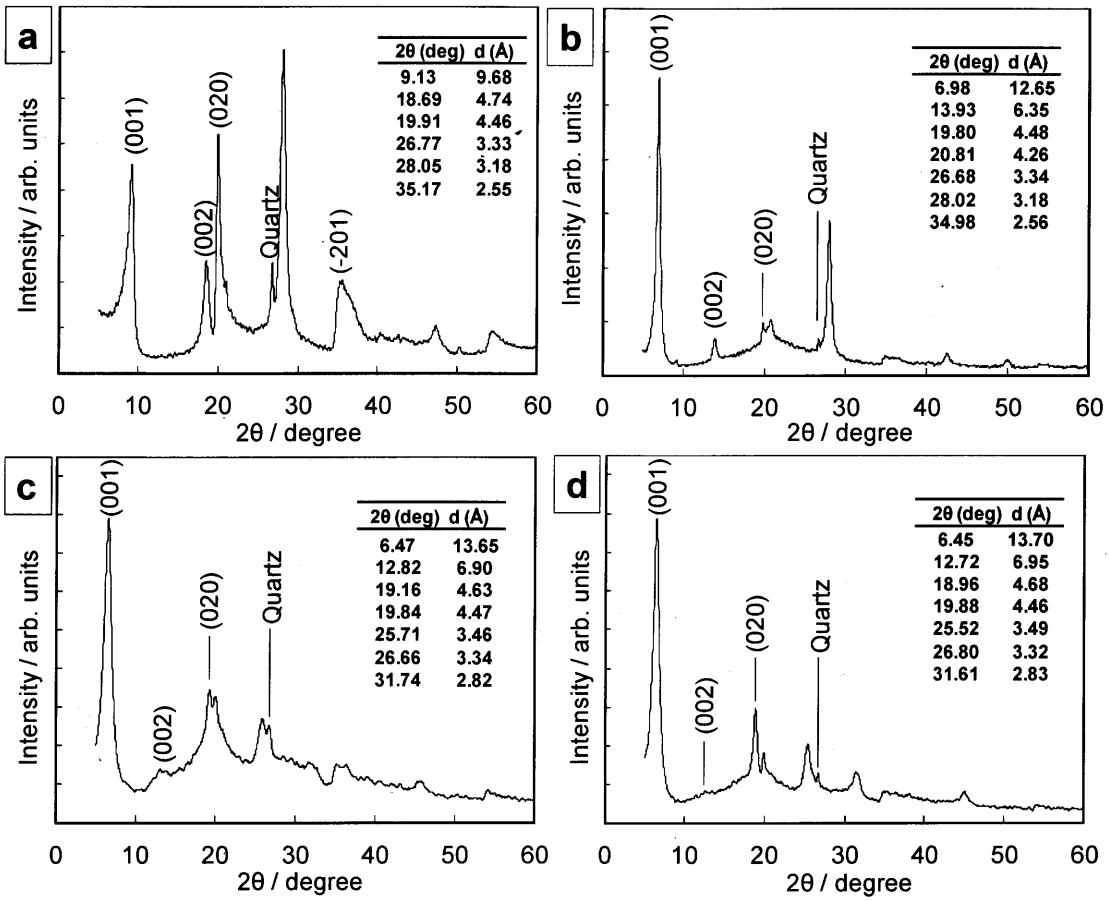

Figure. 6. 8. XRD patterns of (a) dried montmorillonite powder, (b) M_{EMIO}, (c) M_{TMPAT} and (d) M_{DEMET}. The list shows d-spacing of each XRD peaks.

Compared to montmorillonite powder (Figure 6. 8a), we can see that (001) and (020) reflection were shifted to 12.65 Å and 4.48 Å, respectively due to the intercalation of EMIO. Similarly (001) and (020) reflection were shifted to 13.65 Å and 4.63 Å,

respectively due to the intercalation of TMPAT and also (001) and (020) reflection were shifted to 13.70 Å and 4.68 Å, respectively due to the intercalation of DEMET.

The un-indexed XRD peaks were not clearly identified because of impure substance and shift by swelling. We measured both basal plane (001) and high angle peak such as (020) for comparison with selected area electron diffraction (SAED) data. It should be noted here that the IL does not show any XRD peak due to its liquid structure. Thus, as-compared to dried montmorillonite powder, the (001) d-spacing values of three kinds of intercalation compounds showed a remarkable increase from 9.68 Å. This type of swelling, which shows limited d-spacing increase, has been called crystalline swelling. This indicates that cations ($(EMI)^+$, $(TMPA)^+$ and $(DEME)^+$) are successfully intercalated into the interlayer of montmorillonite by a cation exchange process. Interestingly, d-spacing values (001) among M_{EMIO}, M_{TMPAT} and M_{DEMET} intercalated compounds were different compared to dried montmorillonite powder although values of M_{TMPAT} and M_{DEMET} intercalated compounds are almost similar. This indicates that extent of intercalation behavior of alkyl imidazolium IL and ammonium IL into montmorillonite was different. This is because cations of different kinds of ILs are arranged in the interlayer space according to their cation sizes and other properties. Therefore, in order to understand the atomic arrangement of three kinds of ILs into the silicate layer of montmorillonite, CEC of three kinds of intercalated compounds are measured.

6. 3. 2. 2. Atomic arrangement of ILs into the silicate layer of montmorillonite.

Table 6. 4 shows amounts of exchangeable cations in montmorillonite with three kinds of M_{IL} intercalated compounds. It can be seen from Table 6. 4 that total amounts of exchangeable cations for M_{EMIO}, M_{TMPAT} and M_{DEMET} compounds are 116.25, 97.94 and 87.19 meq / 100 g clay, respectively. It should be here noted that CEC value of dried montmorillonite is 119 meq / 100g clay. This indicates that different amount of exchangeable cations for three types of ILs used in the present study.

Table 6. 4. CEC of montmorillonite with different ILs.

Cations	Ionic liquids		
	EMI $OcSO_4$	TMPA TFSI	DEME TFSI
Na^+	96.15	78.62	69.53
Mg^{2+}	3.39	3.19	2.51
K^+	1.35	1.21	0.86
Ca^{2+}	15.36	14.92	14.29
Total (meq / 100 g)	116.25	97.94	87.19

From CEC and Avogadro number, amount of exchangeable cations for montmorillonite, $(EMI)^+$, $(TMPA)^+$ and $(DEME)^+$ are 7.16×10^{22} / 100 g, 7.00×10^{22} / 100

g, 5.90×10^{22} / 100 g and 5.25×10^{22} / 100 g, respectively. In other words, 97.8 %, 82.4 % and 73.3 % cations were exchanged from three kinds of ILs intercalated compounds i.e. M_{EMIO}, M_{TMPAT} and M_{DEMET}, respectively. From the CEC results of M_{EMIO} intercalated compound, we could understand that almost all interlayer exchangeable cations were substituted by $(EMI)^+$ cations. However, in the case of M_{TMPAT} and M_{DEMET} intercalated compounds, some of the exchangeable cations were remained un-exchanged. From literature, we can see that the ionic radius of $(EMI)^+$, $(TMPA)^+$ and $(DEME)^+$ are 3.03, 3.12 and 3.77 Å, respectively [43-46]. The interlayer distance could be obtained by subtracting the thickness of silicate layer (9.6 Å) from the observed basal spacing of M_{IL}. Thus, the interlayer distance of M_{EMIO}, M_{TMPAT} and M_{DEMET} compound were found to be 3.05, 4.05 and 4.12 Å, respectively. XRD results from the interlayer distance and the $(EMI)^+$, $(TMPA)^+$ and $(DEME)^+$ diameter, the tilt angle (θ) of each ions into the interlayer of montmorillonite could be calculated using Wan et.al formula [5].

$$\Delta d = d_{001} - 0.96 = (ionic\ length)\ sin\ \theta \qquad (1)$$

where, ionic length is the diameter of each $(EMI)^+$, $(TMPA)^+$ and $(DEME)^+$ ion. From calculation using formula (1), the corresponding tilt angle of $(EMI)^+$, $(TMPA)^+$ and $(DEME)^+$ were found to be 30.22, 40.47 and 33.12 °, respectively. It is expected that the substituted ions of ILs are arranged as a single ion which exist incline to the silicate layer. Furthermore, the occupation of surface area of each ions toward silicate layer was also analyzed using CEC of M_{IL} and montmorillonite in order to understand the arrangement of these ions into the layer. The surface area of silicate layer was calculated by Olphen method [47] and it was found to be 37446 m^2 / 100 g clay. On the other hand, the surface area of

$(EMI)^+$ ions calculated from $(EMI)^+$ area (0.288 nm^2) and numbers of $(EMI)^+$ ions (7.00 × 10^{22} / 100 g) and was found to be 20160 m^2 / 100 g. Similarly the surface area of $(TMPA)^+$ ions calculated using $(TMPA)^+$ area (0.306 nm^2) and numbers of $(TMPA)^+$ ions (5.90 × 10^{22} / 100 g) and was found to be 18054 m^2 / 100 g. The area of $(DEME)^+$ ions calculated using $(DEME)^+$ area (0.446 nm^2) and numbers of $(DEME)^+$ ions (5.25 × 10^{22} / 100 g) and was found to be 23430 m^2 / 100 g. From these calculations, a schematic structure could be proposed for the three kinds of M_{IL} compounds and is shown in Figure 6. 9.

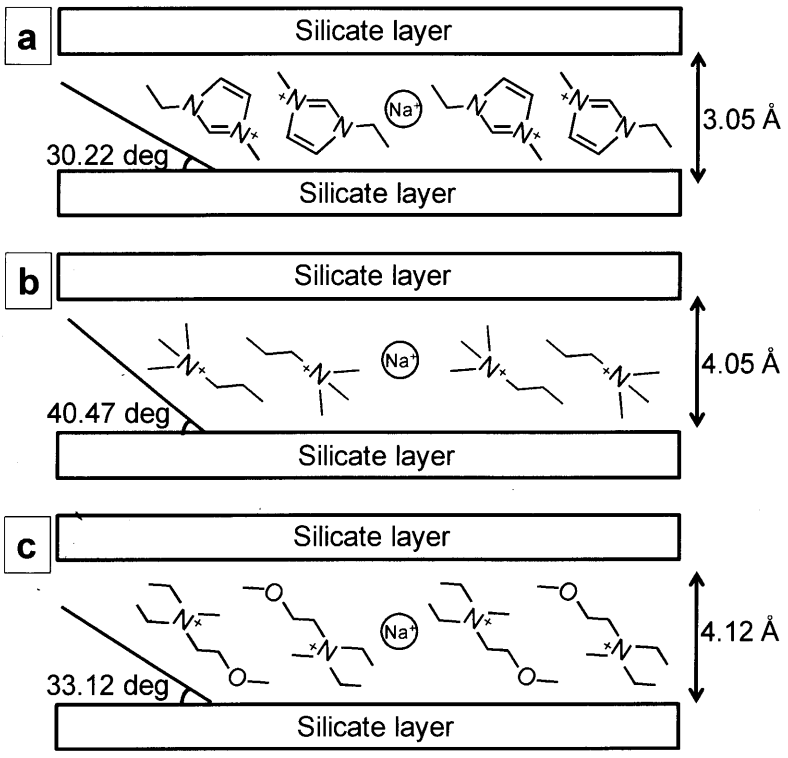

Figure. 6. 9. A proposed schematic structure of the (a) M_{EMIO}, (b) M_{TMPAT} and M_{DEMET} intercalated compounds.

6. 3. 2. 3. Crystal swelling structure of M_{IL} intercalated compounds.

Figure 6. 10 shows TEM images and its corresponding electron diffraction pattern of the dried montmorillonite powder. The layer structures with fine strips of montmorillonite are seen in the high-magnification image (Figure 6. 10c), and the layer spacing is expected to change significantly when montmorillonite is intercalated with the organic or inorganic molecules. The d-spacing of the montmorillonite and quartz is obtained from the Debye ring and is shown in Figure 3d. Here, mainly d-spacing was indexed.

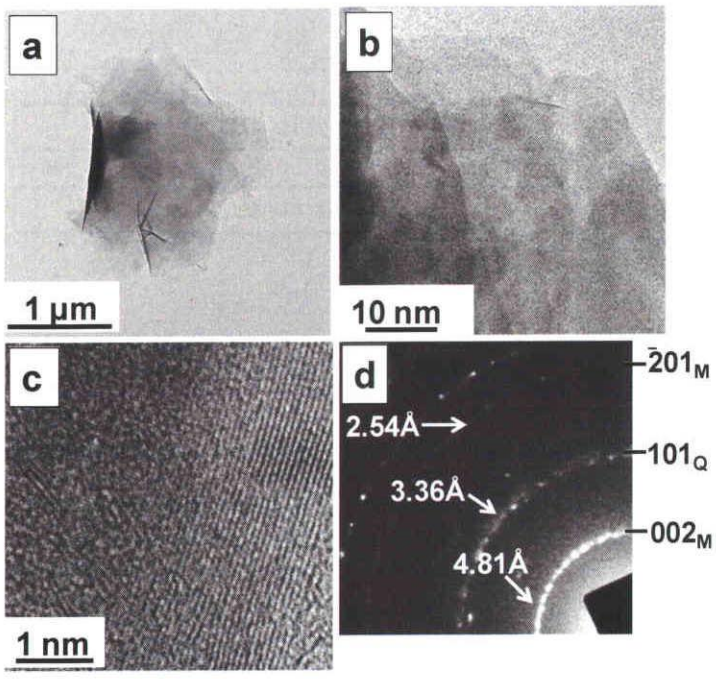

Figure. 6. 10. TEM images of dried montmorillonite powder in bright-field images (a), (b), high resolution image (c) and SAED pattern in which the Debye rings are indexed (d). The subscript M is derived from montmorillonite and Q from quartz.

Figure 6. 11 shows the TEM images and its SAED pattern of the M_{EMIO} intercalated compound. It can be seen in Figure 6. 11a that the structure consists of swelled-like area and maintains the crystal structure. Figure 6. 11b shows magnified image of layer structure of M_{EMIO} intercalated compound. Compared with dried montmorillonite (Figure 6. 10), the interlayer space of M_{EMIO} was increased remarkably. High-resolution observation confirmed that the d-spacing of crystal in this area is 3.18 Å (Figure 6. 11c). The diffraction pattern can be interpreted as a mixture of randomly oriented crystallites of montmorillonite. From the Debye ring, each d-spacing from montmorillonite was calculated and is shown in Figure 6. 11d.

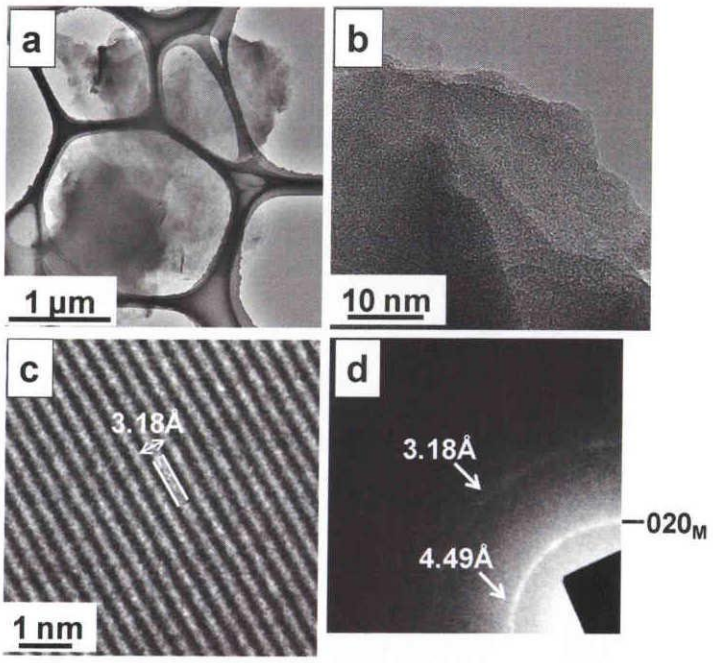

Figure. 6. 11. TEM images of M_{EMIO} intercalated compound in bright-field images (a)(b), high-resolution image (c), and SAED pattern in which the Debye rings are measured (d). The subscript M is derived from montmorillonite.

Similarly, Figure 6. 12 shows the TEM image and its SAED pattern of the M_{TMPAT} intercalated compound. It can be seen in Figure 6. 12a that the structure consists of the swelled-like area and maintains the crystal structure. Figure 6. 12b shows magnified image of layer structure of M_{TMPAT} intercalated compound. Compared with dried montmorillonite, it is clear that the interlayer space of M_{TMPAT} was increased drastically. High-resolution observation confirmed that the d-spacing of crystal in this area is 3.48 Å (Figure 6. 12c). The diffraction pattern can be interpreted as a mixture of randomly oriented crystallites of montmorillonite. From the Debye ring, the each d-spacing from montmorillonite was calculated and is shown in Figure 6. 12d.

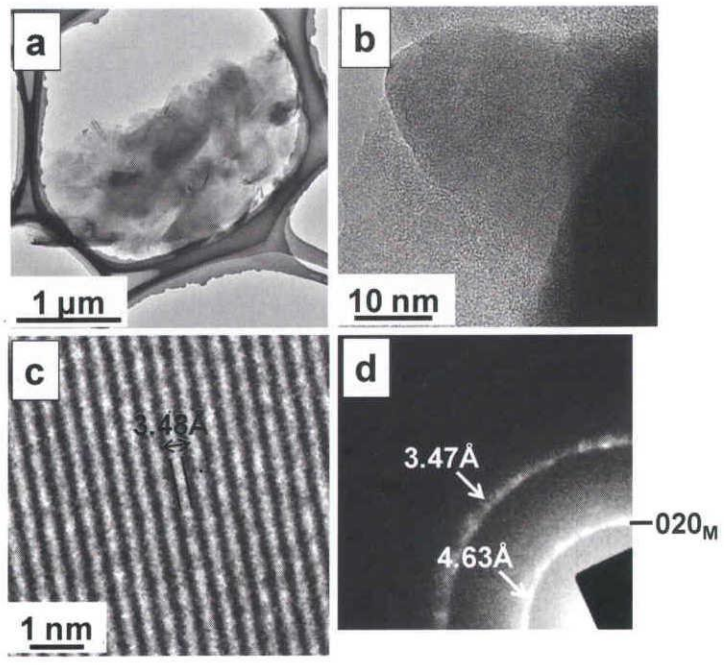

Figure. 6. 12. TEM images of M_{TMPAT} intercalated compound in bright-field images (a), (b), high-resolution image (c), and SAED pattern in which the Debye rings are measured (d). The subscript M is derived from montmorillonite.

Figure 6. 13 shows the TEM image and its SAED pattern of the M_{DEMET} intercalated compound. It can be seen in Figure 6. 13a that the structure consists of the swelled-like area and maintains the crystal structure. Figure 6. 13b shows magnified image of layer structure of M_{DEMET} intercalated compound. Compared with dried montmorillonite, it is clear that the interlayer space of M_{DEMET} was increased drastically. High-resolution observation confirmed that the d-spacing of crystal in this area is 3.50 Å (Figure 6. 13c).

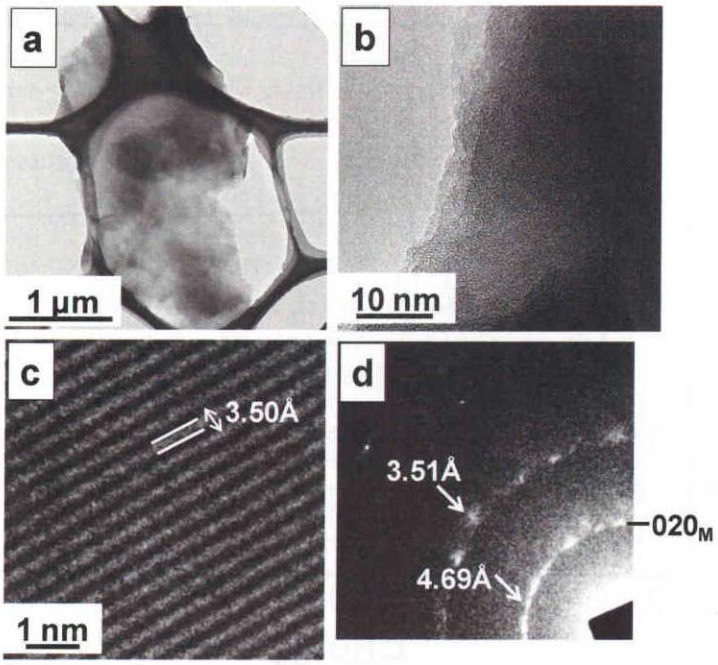

Figure. 6. 13. TEM images of M_{DEMET} intercalated compound in bright-field images (a), (b), high-resolution image (c), and SAED pattern in which the Debye rings are measured (d). The subscript M is derived from montmorillonite.

The diffraction pattern can be interpreted as a mixture of randomly oriented crystallites of montmorillonite. From the Debye ring, the each d-spacing from

montmorillonite was calculated and is shown in Figure 6. 13d. Thus comparing Figure 6. 10 to 6. 13, we could see that the layer spacing changed significantly when montmorillonite was separately treated with three kinds of ILs. This TEM result reconfirmed the intercalation of ILs directly into the montmorillonite inter layers and the extent of intercalation was different for different kinds of IL due to variable cation sizes.

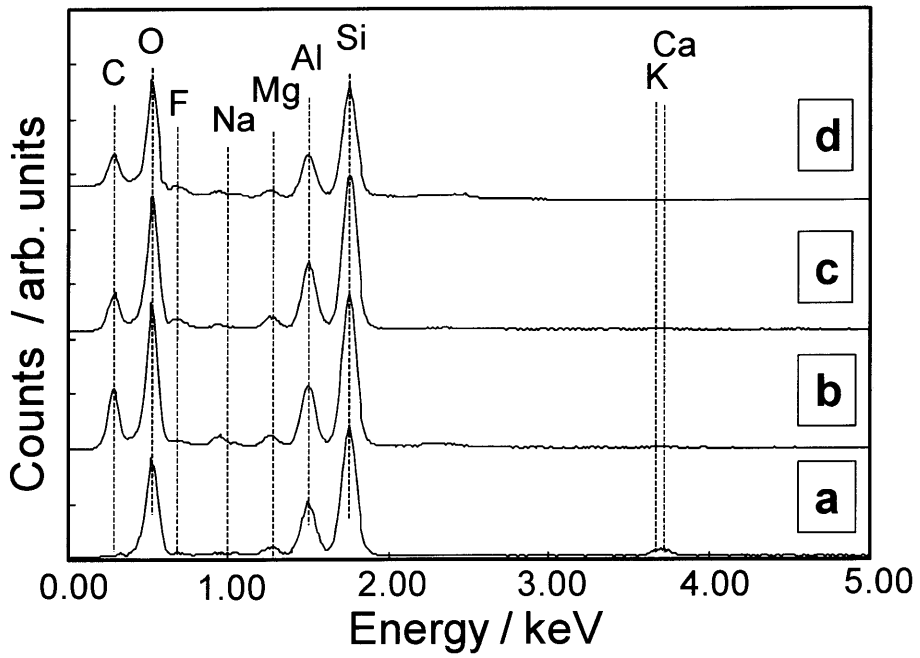

Figure. 6. 14. TEM-EDS spectra of dried montmorillonite powder (a), M_{EMIO} (b), M_{TMPAT} (c) and M_{DEMET} intercalated compound (d).

Figure 6. 14a-d show EDS spectra of dried montmorillonite powder (as a reference), M_{EMIO}, M_{TMPAT} and M_{DEMET} intercalated compounds, respectively. It can be seen that the dried montmorillonite had well-known peaks such as Al, Si, Na, Mg, Ca etc (Figure 6. 14a).

On the other hand, in the case of M_{EMIO}, M_{TMPAT} and M_{DEMET} the strong C peak derived from EMI^+, $TMPA^+$ and $DEME^+$ were obtained, respectively (Figure 6. 14b-d). F peak derived from anion part of IL were almost not detected. Therefore, it can be further confirmed that cation parts of ILs were intercalated to montmorillonite, respectively. Comparing the XRD and SAED results (see Table 6. 5), we can see that the d-spacing had no significant difference, although diffraction patterns of (001) reflection were not observed for the reason of close to direct beam. These results suggest that we could successfully observe the nano-scaled crystal swelling structure of montmorillonite-ionic liquid intercalated compound using TEM.

Table 6. 5. Comparison of d-space of dried montmorillonite powder and three kinds of M_{IL} intercalated compounds obtained from XRD and SAED.

Dried Montmorillonite		M_{EMIO}		M_{TMPAT}		M_{DEMET}	
XRD (Å)	SAED (Å)	XRD (Å)	SAED (Å)	XRD (Å)	SAED (Å)	XRD (Å)	SAED (Å)
4.74	4.81	4.48	4.49	4.63	4.63	4.68	4.69
3.33	3.36	3.18	3.18	3.46	3.47	3.49	3.51
2.55	2.54	2.56	2.58	2.82	2.83	2.83	2.85

6. 3. 2. 4. Thermal stability of M_{IL} intercalated compounds.

Figure 6. 15a-g shows TG-DTA spectra of dried montmorillonite powder, EMIO, M_{EMIO}, TMPAT, M_{TMPAT}, DEMET and M_{DEMET}, respectively. Typically, the endothermic peak around 700 °C is observed corresponding to the decomposition of structural hydroxyl

groups in the aluminosilicate (Figure 6. 15a) [48]. In this study, the loss attributed to the removal of externally absorbed water is not observed around 100 °C owing to removal of the interlayer water during preparation. Decomposition of IL (EMIO) was observed in the range of 350 to 500 °C. However, in the case of M_{EMIO} intercalated compound, the decomposition of $(EMI)^+$ was shifted and observed in the range of 450 to 550 °C. Comparing EMIO and M_{EMIO} results, the endothermic peak top was shifted from 477.7 to 566.0 °C, respectively (Figure 6. 15b and c). Decomposition of IL (TMPAT) was observed in the range of 350 to 500 °C, while in the case of M_{TMPAT} intercalated compound, the decomposition of $(TMPA)^+$ was observed in the range of 400 to 550 °C. Comparing TMPAT and M_{TMPAT} results, the endothermic peak top was shifted from 459.1 to 478.3 °C, respectively (Figure 6. 15d and e). Furthermore, decomposition of IL (DEMET) was observed in the range of 350 to 450 °C, while in the case of M_{DEMET} intercalated compound, the decomposition of $(DEME)^+$ was observed in the range of 400 to 550 °C. Comparing DEMET and M_{DEMET} results, the endothermic peak top was shifted from 443.1 to 454.4 °C, respectively (Figure 6. 15f and g). The raw montmorillonite accounts for 6.76 % weight loss, while three kinds of ILs (EMIO, TMPAT and DEMET) showed 100 % weight loss in TG curve, respectively (Figure 6. 15a, b, d, f). However, in the case of M_{EMIO}, weight loss which is attributed to the decomposition of the IL was observed by 6.98 % and total weight loss of M_{EMIO} was 13.12 %. In the case of M_{TMPAT}, weight loss which is attributed to the decomposition of the IL was observed by 6.65 % and total weight loss of M_{EMIO} was 12.75 %. Similarly, the case of M_{DEMET}, weight loss which is attributed to the decomposition of the IL was observed by 9.71 % and total weight loss of M_{EMIO} was 15.8 %.

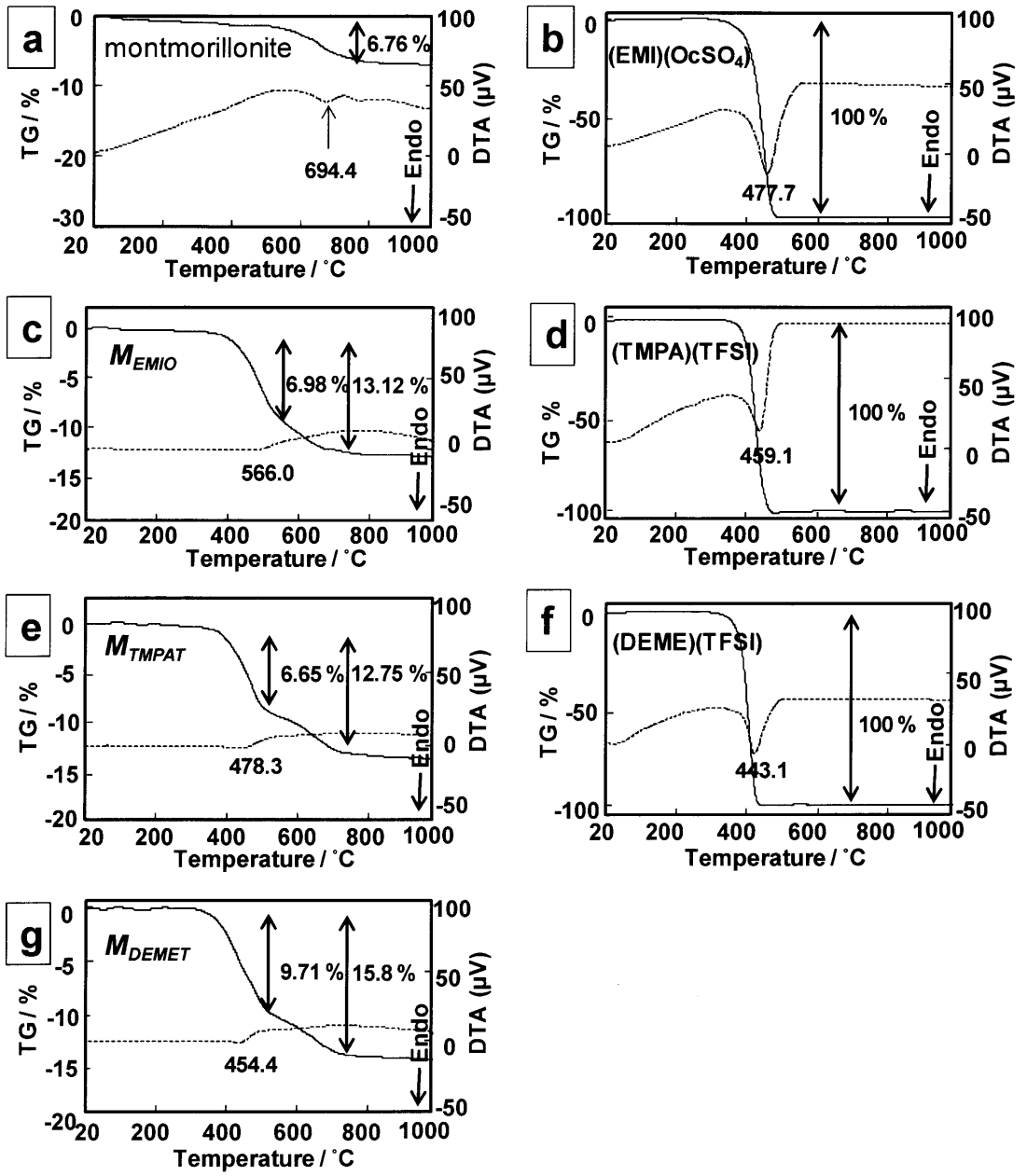

Figure. 6. 15. TG-DTA analysis of dried montmorillonite powder (a), raw IL (EMIO) (b), M_{EMIO} intercalated compound (c), raw IL (TMPAT) (d), M_{TMPAT} intercalated compound (e), raw IL (DEMET) (f) and M_{DEMET} intercalated compound (g). Black and dashed line indicates TG and DTA peak, respectively.

In this study, IL (cation) weight within montmorillonite could be calculated using cation molecular weight and cation exchange number. Molecular weight of $(EMI)^+$, $(TMPA)^+$ and $(DEME)^+$ are 111.3, 102.18 and 146.24, and cation exchange number was obtained by CEC values taken from Table 6. 4. CEC values are 116.25, 97.94 and 87.19 g / 100 g, respectively. At first, cation exchange number was calculated using CEC values according to each cation valence, and, was multiplied by Avogadro number. The values of IL (cation) weight within montmorillonite are 11.90 g / 100 g $(EMI)^+$, 9.08 g / 100 g $(TMPA)^+$ and 11.52 g / 100 g $(DEME)^+$, respectively.

Thus comparing TG and the calculated data, it can be seen that IL still remained intercalated in the montmorillonite layer irrespective of kinds of ILs. Results showed that in the case of M_{EMIO}, M_{TMPAT} and M_{DEMEI} compounds 41.3, 26.8 and 15.7 % of IL remained undecomposed, respectively. However, the exothermic peak of M_{IL} intercalated compounds were obtained just after endothermic peak. On the other hand, the decomposition of structural hydroxyl groups in the aluminosilicate could also be observed. Decomposition weight of montmorillonite within M_{IL} intercalated compounds was obtained by subtracting weight loss of M_{IL} intercalated compounds to IL within M_{IL} intercalated compounds. For comparison with weight loss of raw montmorillonite, IL (cation) weight within montmorillonite was removed to calculate the decomposition weight of montmorillonite. The weight loss of montmorillonite within M_{EMIO}, M_{TMPAT} and M_{DEMEI} was 6.97, 6.71 and 6.88 %, respectively although raw montmorillonite was 6.76 %. There is no significant difference of weight loss of montmorillonite in dried montmorillonite powder and M_{IL} intercalated compounds.

These results showed that all M_{IL} intercalated compounds have thermal stability. Especially, thermal stability of imidazolium IL in clay increased about 90 °C compared with only IL. It is reported that thermal decomposition change depending on the salt structure of IL [12,49]. Imidazolium IL in clay has higher thermal stability than ammonium IL in clay [13]. Our TG-DTA results are in good agreement with the early reports. It is expected that these thermal stability were caused by the strong interaction between the cationic parts of ILs and the surface Al-OH groups.

Compared to montmorillonite powder, we noticed that M_{IL} intercalated compounds after heated 1000 °C under Ar gas became black in color. Therefore, it can be expected that carbonization of M_{IL} intercalated compounds was occurred through the carbothermal reduction. Due to understand the behavior of remained IL in montmorillonite of M_{IL} intercalated compounds after heated at 1000 °C under Ar gas, d-spacing of M_{IL} intercalated compounds was measured by XRD.

Figure 6. 16a-d shows XRD patterns of dried montmorillonite powder and three kinds of M_{IL} intercalated compounds after heated 1000 °C under Ar gas. In the case of dried montmorillonite powder, it can be seen that high intensity peak correspond to mullite and small peaks correspond to cristbalite and quartz in Figure 6. 16a. On the other hand, in the case of three kinds of M_{IL} intercalated compounds, broad peak containing only small quartz and graphite peak can be seen in the spectra (Figure 6. 16b-d). Compared with montmorillonite powder, we can see amorphous phases along with small peaks. Although M_{IL} intercalated compound has thermal stability corresponding to IL salt structure, there are

no difference of carbonization behavior among M_{EMIO}, M_{TMPAT} and M_{DEMET} intercalated compounds after heated 1000 °C under Ar gas.

From previous studies, structure of dried montmorillonite powder after heated 1000 °C under Ar gas was broken, and, cristobalite and mullite have appeared after separation. Furthermore, carbide can be fabricated using inorganic clay - organic (such as polyacrylonitrile (PAN), polyfurfuryl alcohol (PFA) and polyvinyl acetate (PVAC)) intercalation compounds by heating under Ar gas through the carbothermal reduction [50-52]. SiC formed from inorganic clay - organic intercalation compounds by combining carbon from organic compounds and aluminosilicate layer from montmorillonite after heated at 1300 °C under Ar gas. Furthermore, Mg-Al-O compound with spinel structure formed from Al_2O_3 of aluminosilicate layer. Bastow et al. reported that amorphous peak including quartz and graphite was obtained from montmorillonite – polyacrylonitrile (PAN) intercalated compounds after heated at 1000 °C under N_2 gas [48]. Present XRD results are in good agreement with earlier reports.

It can be expected that carbide started to form in M_{IL} intercalated compounds when the mixture was heated at 1000 °C under Ar gas although SiC did not appear clearly. Therefore, it can be considered that remaining IL after heated at 1000 °C under Ar gas exists as carbon which is connected with aluminosilicate layers.

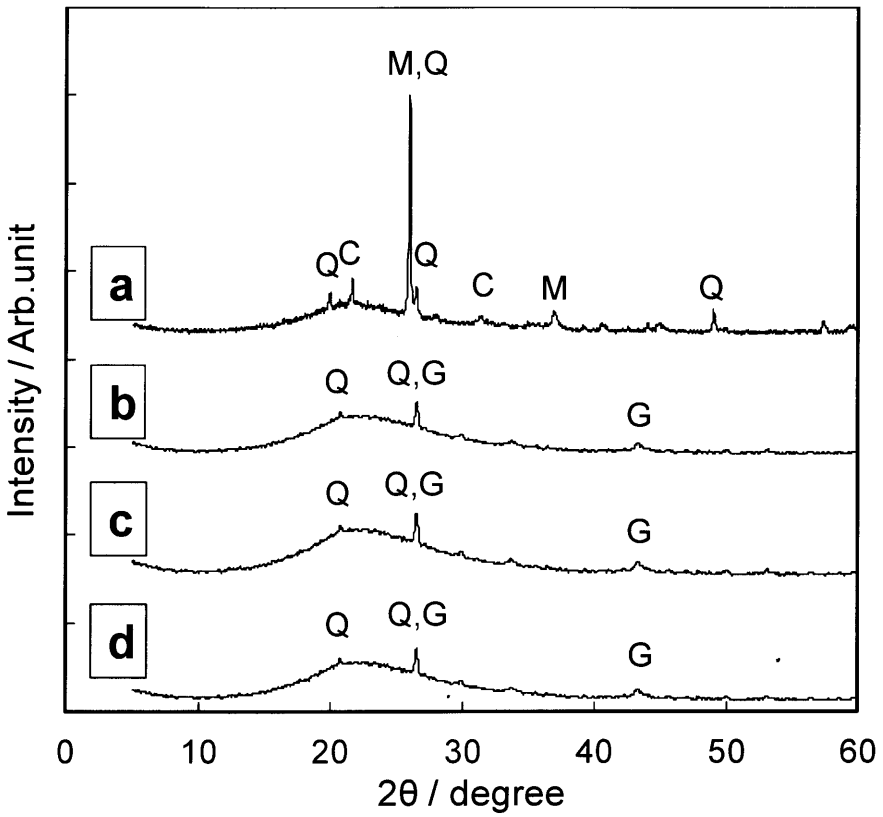

Figure. 6. 16. XRD patterns of (a) dried montmorillonite powder, (b) M_{EMIO}, (c) M_{TMPAT} and (d) M_{DEMET} intercalated compound after heated at 1000 °C under Ar gas. The subscript C, M, Q, and G are derived from cristobalite, mullite, quartz and graphite, respectively.

6. 4. Conclusions

From the present study following conclusions could be drawn. (1) Four kinds of IL and montmorillonite intercalated compounds could be directly fabricated by mixing IL of different salts (imidazolium and ammonium) and cation size and montmorillonite clay. (2)

XRD results showed that the cation size of the ILs affect the extent of crystal swelling and TEM-EDS further confirmed the intercalation of each IL into montmorillonite interlayer. (3) Crystal swelling behavior as observed by XRD was further verified by TEM-SAED. (4) From CEC results and mathematical calculations, extent of intercalation and arrangement of cations in the interlayers of montmorrilonite clay is proposed. In addition, XRD and CEC results confirmed that IL intercalated into the montmorillonite's interlayer within 1 min of mixing and attained a saturation level very rapidly. (5) TG-DTA measurement of three kinds of M_{IL} intercalated compounds (M_{EMIO} , M_{TMPAT} and M_{DEMET}) showed improved thermal stability as compared to IL. (6) XRD indicates that remaining IL in the three kinds of M_{IL} intercalated compounds (M_{EMIO}, M_{TMPAT} and M_{DEMET}) initiates carbonization process above 1000 °C under Ar gas.

This observation technique is useful to understand the intercalated behavior and swelling structure of layered materials with liquid phase. In addition, low sheet resistivity of montmorillonite - IL composite indicates a possibility of such a better thermally stable material as transparent electrically conducting thin film.

Acknowledgements

The authors are grateful to Dr. T. Okada, of Shinshu University, Japan for useful discussions.

References

[1] C. Takahashi, T. Shirai, M. Fuji, Mater. Chem. Phys. (2012) under review.

[2] F. Bergaya, B. K. G. Theng, G. Lagaly, Handbook of Clay Science, first ed., Elsevier, Amsterdam, 2006.

[3] M. Ogawa, T. Aono, K. Kuroda, C. Kato, Langmuir. 9 (1993) 1529-1533.

[4] M. Ogawa, Langmuir. 11 (1995) 4639-4641.

[5] T. Wan, H. Xu, Y. Yuan, W. He, J. Wuhan. Uni. Tech. Mater. Sci. Ed. 22 (2007) 466-469.

[6] S. Letaief, C. Detellier, J. Mater. Chem. 17 (2007) 1476-1484.

[7] H. Tetsuka, T. Ebina, H. Nanjyo, F. Mizukami, J. Mater. Chem. 17 (2007) 3345-3350.

[8] C. H. Lee, M. Kato, A. Utsuki, J. Mater. Chem. 21 (2011) 6844-6847.

[9] E. Ruiz-Hitzky, P. Aranda, J. M. Serratosa, M. Auerbach, K. Carrado, P. K. Dutta (Eds.), Handbook of Layered Materials, Marcel Dekker, Inc. New York, 2004, pp. 91-154.

[10] G. Zhang, T. Shichi, K. Takagi, Mater. Lett. 57 (2003) 1858-1862.

[11] J. F. Martucci, A. Vazquez, R. A. Ruseckaite, J. Therm. Anal. Cal. 89 (2007) 117-122.

[12] J. W. Gilman, W. H. Awad, R. D. Davis, J. Shields, R. H. Harris, C. Davis, A. B. Morgan, T. E. Sutto, J. Callahan, P. C. Trulove, H. C. DeLong, Chem. Mater. 14 (2002) 3776.

[13] N. H. Kim, S. V. Malhotra, M. Xanthos, Micropor. Mesopor. Mat. 96 (2006) 29.

[14] M. Segad, S. Hanski, U. Plsson, J. Ruokolainen, T. Akesson, B. G. Jonsson, J. Phys. Chem. C. 116 (2012) 7596.

[15] T. Mitsudome, K. Nose, T. Mizugaki, K. Jitsukawa, K. Kaneda, Tetrahedoron. lett. 49 (2008) 5464.

[16] Y. Ding, R. Xiong, S. Wang, X. Zhang, J. Polym. Sci. Pol. Phys. 45 (2007) 1252.

[17] Y. Ding, X. Zhang , R. Xiong, S. Wu, M. Zha, H. Tang, Eur. Polym. J. 44 (2008) 24.

[18] Y. P. Wang, X. H. Gao, R. M. Wang, H. G. Liu, C. Yang, Y. B. Xiong, React. Funct. Polym. 68 (2008) 1170.

[19] S, Letaief, C. Detellier, Clay. Clay. Miner. 57 (2009) 638.

[20] W. F. Cui, X. H. Gao, Y. P. Wang, Asian. J. Chem. 22 (2010) 911.

[21] J. U. Ha, and M. Xanthos, Green. Chem. Let. Rev. 4 (2011) 103.

[22] S. Livi, J. Duchet-Rumeau, T. N. Pham, J. F. Gerard, J. Colloid Interf. Sci. 354 (2011) 555.

[23] P. Wasserscheid, C. M. Gordon, C. Hilgers, M. J. Muldoon, I. R. Dunkin, Chem. Commun. 111 (2001) 1186-1187.

[24] J. F. Wishart, E. W. Castner, J. Phys. Chem. B. 111 (2007) 4639-4640.

[25] S. Seki, Y. Ohno, Y. Kobayashi, H. Miyashiro, A. Usami, Y. Mita, H. Tokuda, M. Watanabe, K. Hayamizu, S. Tsuzuki, M. Hattori, N. Terada, J. Electrochem. Soc. 154 (2007) A173-A177.

[26] T. Kakibe, J. Hishii, N. Yoshimoto, M. Egashira, M. Morita, J. Power. Sources. 203 (2012) 195-200.

[27] T. Torimoto, K. Okazaki, T. Kiyama, K. Hirahara, N. Tanaka, S. Kuwabata, Appl. Phys. Lett. 89 (2006) 243117.

[28] D. Oyamatsu, T. Fujita, S. Arimoto, H. Munakata, H. Matsumoto, S. Kuwabata, J. Electroanal. Chem. 615 (2008) 110-116.

[29] F. H. Hurley, T. P. Wier, J. Electrochem. Soc. 98 (1951) 203-206.

[30] J. S. Wilkes, M. J. Zaworotko, J. Chem. Soc., Chem. Commun. 13 (1992) 965-967.

[31] T. Welton, Chem. Rev. 99 (1999) 2071-2083.

[32] K. R. Seddon, Nat. Mater. 2 (2003) 363-365.

[33] S. Kuwabata, A. Kongkanand, D. Oyamatsu, T. Torimoto, Chem. Lett. 35 (2006) 600-601.

[34] T. Torimoto, K. Okazaki, T. Kiyama, K. Hirahara, N. Tanaka, S. Kuwabata, Appl. Phys. Lett. 89 (2006) 243117.

[35] S. Arimoto, M. Sugimura, H. Kageyama, T. Torimoto, S. Kuwabata, Electrochim. Acta. 53 (2008) 6228-6234.

[36] S. Ishibashi, Y. Higuchi, Y. Ota, K. Nakmura, J. Vac. Sci. Technol. A. 8 (1990) 1403-1406.

[37] C. Guillen, J. Herrero, J. Appl. Phys. 101 (2007) 073514.

[38] M. E. White, O. Bierwagen, M. Y. Tsai, J. S. Speck, J. Appl. Phys. 106 (2009) 093704.

[39] T. Okada, Y. Ehara, M. Ogawa, Clays. Clay. Miner. 55 (2007) 348-353.

[40] C. J. Schollenberger, R. N. Simon, Soil. Sci. 59 (1945) 13-24.

[41] R. Miyawaki, T. Sano, F. Ohashi, M. Suzuki, T. Kogure, T. Okumura, J. Kameda, T. Umezome, T. Sato, D. Chino, K. Hiroyama, H. Yamada, K. Tamura, K. Morimoto, S. Uehara, T. Hatta, Nendo Kagaku. The Clay Science Society of Japan, 48 (2010) 158-198.

[42] R. E. Grim (Eds.), Clay mineralogy, McGraw-Hill, Inc. New York, 1953, pp. 55-57.

[43] M. Ue, J. Electrochem. Soc. 141 (1994) 3336-3342.

[44] M. Ue, A. Murakami, S. Nakamura, J. Electrochem. Soc. 149 (2002) A1385-1388.

[45] H. Tokuda, K. Hayamizu, K. Ishii, M. A. B. H. Susan, M. Watanabe, J. Electrochem. Soc. 108 (2004) 16593-16600.

[46] R. Kawano, H. Tokuda, J. Electrochem. Soc. 141 (1994) 3336-3342.

[47] H. V. Olphen, An Introduction to Clay Colloid Chemistry, second ed., Wiley, New York, 1977.

[48] T. Bastow, S. G. Hardin, and T. W. Turney, J. Mater. Sci. **26**, 1443 (1991).

[49] H. L. Ngo, K. LeCompte, L. Hargens and A.B. McEwen, Thermochim. Acta. **357**, 97 (2000).

[50] Y. Sugahara, K. Sugimoto, K. Kuroda, and C. Kato, J. Am. Ceram. Soc. **71**, C-325 (1988).

[51] N. Sonobe, T. Kyotani, and A. Tomita, Carbon. **28**, 483 (1990).

[52] T. Kyotani, K. Suzuki, N. Sonobe, and A. Tomita, Carbon. **31**, 149 (1993).

CHAPTER 7

CONCLUDING REMARKS AND POTENTIAL DIRECTIONS FOR FUTURE RESEARCH

7. 1. Concluding remarks

Electron microscopic techniques have been developed and very often used to characterize micro- and nano-structured materials. Most of the cases of solid materials, such as ceramics, metals, polymers and composites in their dry conditions, are observed. However, the observation methods for hydrous materials are still been developed because the wettability of a sample is not suitable for electron microscopy under high vacuum conditions. This difficulty in the characterization of hydrous materials is a barrier to the research progress related to wet materials processing.

This dissertation study successfully developed an observation method with the aid of a hydrophilic IL for various kinds of hydrated materials useful for various functional applications. By development of the observation method for seaweed, agar gel, a HAp green body and hydrous montmorillonite, the characterization of hydrous materials in an entire range of fields could be found. Based on the interaction between the water molecules and hydrophilic IL, the mechanism for the observation of wet materials using the hydrophilic IL could be revealed and the molecular dynamics of the IL and solvents was studied. In addition, an IL-inorganic composite material was also successfully fabricated by mixing of the IL and montmorillonite clay in the proper ratio to determine the possibility of electron conductive transparent thin films.

The summary and conclusions of the thesis work are itemized as the followings.

In chapter 1, a brief description of the recent trends in the characterization of hydrous materials using an electron microscope in the material research field was presented. At present, new methodologies for the observation of hydrous materials are still being developed because of their difficult characterization by electron microscopy under vacuum conditions. The hydrophilic ionic liquids (ILs) were used as the solvent for visualizing the hydrated materials due to their advantageous properties such as non-flammable, high electron conductivity and negligible vapor pressure. Based on the interaction of hydrophilic ILs and water molecules, the optimized conditions for observation of hydrous materials with the aid of hydrophilic ILs were studied.

In chapter 2, the surface morphology of agar gel under various swelling conditions could be observed using an electron microscope with the optimum conditions using the hydrophilic IL. Agar gel is a commonly used material which has wide applications in biology, medicine, food industries and ceramics industries such as a culturing medium of microbes and a gelling agent for ceramic forming processes. Also, the visualization mechanism of the agar gel with the aid of an IL was examined by Raman spectroscopy. We found that the exact morphology of the agar gel could be obtained by adjusting the water concentrations in the range of 15-30 mol % in the samples. In such cases, the anion part of the IL and water formed weak hydrogen bonds such as $BF_4^-\cdots H\text{-}O\text{-}H\cdots BF_4^-$, and this bonding was stable even at 200 °C. IL first takes a water molecule within the agar gel due to its strong binding ability with water when samples were stored in a desiccator for 3 h as the sample preparation condition for the FE-SEM observations. Subsequently, the bonded IL and water molecules coexist in the

agar gel instead of free water within the agar gel, thus the wet gel morphology is maintained even under vacuum conditions. The optimization method for the microscopic observation of the polymer gel using the hydrophilic IL was investigated.

In Chapter 3, to establish the enhanced processing conditions for ceramics, the complex structure of HAp green bodies in the hydrated form was determined using FE-SEM by the developed observation method. The FE-SEM observations of the HAp green bodies during drying in a humidity chamber from 90 to 50 % relative humidity revealed the solidification process of the ceramic gel casting method which has never been reported. Using this method, we could observe the shrinkage in the pore diameter of a HAp green body during its drying process in the humidity chamber. Moreover, the observation of the hydrated porous HAp green body by micro-focused X-ray CT was compared to the present observation method, and the limitations of the X-ray CT were investigated. From the Raman spectra, the IL and water molecules were found to form weak hydrogen bonds in the hydrated porous HAp body similar to the agar gel when the water concentration of the sample after the IL treatment is 30 mol %.

In chapter 4, the observation mechanism of seaweed as a biological material was reported using a commercially available hydrophilic IL by FE-SEM. Results showed that the visualization mechanism of the seaweed using IL was different from inorganic hydrated materials and a biological polymer gel which could be observed using the developed method as described in chapters 2 and 3. It was confirmed that the osmotic pressure of biomaterials in the IL solution affects the morphology. Therefore, the IL diluted by water was used as a solvent to maintain the osmotic pressure of the seaweed in the solution. Moreover, centrifuging enables one to observe the fine morphology of seaweed by removing the excess IL around the sample. The observation methodology

for biological materials using a commercially available IL could be successfully developed.

In chapter 5, to observe the swelling behavior and fine structure of the hydrous clay, the montmorillonite swelled by water was determined. The IL was intercalated into the montmorillonite interlayer by displacement of the water molecules within the montmorillonite as a fixed arrangement even in the case of montmorillonite swelled by a large amount of water. The exact morphology and structure of the swelled montmorillonite might be maintained because of the card house-like structure. Thereby, montmorillonite with an intercalated ability have been successfully observed using the IL.

In chapter 6, the direct intercalation of an IL into the montmorillonite was attempted, and fabricated intercalated compounds using four kinds of ILs, which consisted of different salts (imidazolium and ammonium) and cation sizes. These intercalated compounds could be fabricated by mixing of the IL and montmorillonite. The crystal swelling structure of the hydrous clay was characterized by TEM and the swelling behavior was verified by XRD, TEM-SAED and CEC. It was confirmed that the IL intercalated into the montmorillonite's interlayer within 1 min of mixing and attained a very rapid saturation level. Arrangement of the cations in the interlayer of the montmorillonite was proposed from the CEC experimental results and mathematical calculations. In addition, the TG-DTA measurement of the intercalated compounds showed an improved thermal stability as compared to the IL and an XRD measurement showed that the remaining IL in the intercalated compounds initiates the carbonization process above 1000 °C under Ar gas. A simple fabrication method of intercalated compounds using the IL was successfully developed, which could be characterized.

Based on these findings, it was concluded that the developed methodology using an IL helps to observe the hydrated materials in various fields by electron microscopy. The materials can be classified for observation as follows:

A. Hydrated insulating materials, such as an agar gel, a HAp green body and montmorillonite swelled by water, and

B. Biological materials, such as seaweed, which were maintained by osmotic pressure.

Each optimization method is described and shown in Figure 7. 1.

A: (1) Sample is treated by IL and adjusted by 30 mol % water concentrations. (2) Sample is kept in a desiccator for 2 h + under vacuum for 24 h. (3) To remove the excess IL from around the sample, the sample is centrifuged.

B: (1) Sample is preserved by each sampling method for adjusting the osmotic pressure as a natural environment. (2) Sample is treated by IL diluted in water to maintain its osmotic pressure, and adjusted using a 30 mol % water concentration. (3) Sample is kept in a desiccator for 2 h + under vacuum for 24 h. (4) To remove the excess IL from around sample, the sample was centrifuged.

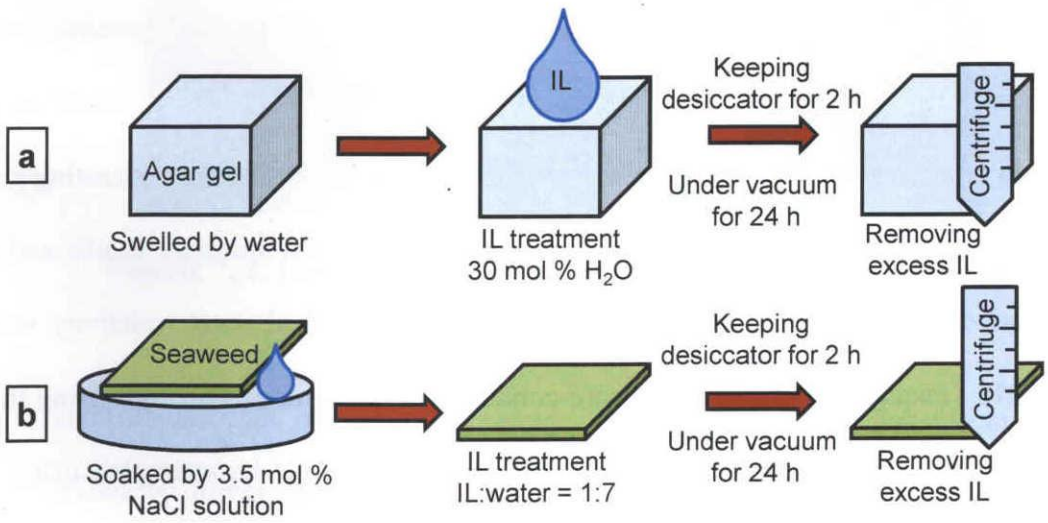

Figure. 7. 1. Observation method for (a) hydrated insulating materials and (b) biomaterials.

These observation techniques are useful for understanding the exact morphology and behavior of any kind of hydrated material including biological materials and inorganic materials. The understanding of a visualization mechanism using a hydrophilic IL can also contribute to studying the molecular dynamics of the IL and solvents, such as water and ethanol. In addition, fabricating the montmorillonite - IL composite materials can possibility produce a better thermally stable material as a transparent electrically conducting thin film.

7. 2. Potential directions for future research

In the present study, only seaweed as the case study of biological materials was investugated to observe its fine morphology. Further studies of biological materials, such as microbes including culture media, human cells, plant cell, etc., should be observed and the visualization mechanism using the hydrophilic IL evaluated. Particularly, in the plant pathology field, mechanisms of some plant diseases still need to be studied due to the difficulty of direct observations by electron microscopy. The origin of diseases of plants is needed in order to investigate the mechanism of plant diseases. Also, hydrated ceramic gels of various kinds of ceramics should be observed in order to consider a better way of fabricating ceramics using the gel casting process.

Conductive materials were fabricated using IL and montmorillonite and obtained good electrical sheet resistibility. The measured electrical sheet resistivity was around 418 Ω/square. To fabricate a more conductivity transparent thin film using the IL and montmorillonite, combinations of the IL and clay should be attempted using different kinds of ILs and clays, such as smectites, kaolinite, mica, vermiculite, pylophyllite, sepiolite, etc. The development of the film formation also has an important role for

obtaining a high electron conductivity.

The lithium ion battery as a renewable energy source is the center of attention because of its eco-friendly, clean and non-expensive properties. The lithium ion battery has a high energy density despite its small size and light weight. Therefore, the lithium ion cell has an important role as an energy device for mobile electronic devices and electric cars. To improve the high output ability and safety of the lithium ion cell, the ionic behavior and reaction on the surface and inside the electrolyte and interface between the electrode and electrolyte in an electric field should be understood. Although the interface between an electrode and electrolyte has been observed using in-situ TEM by some researchers, the surface and inside the electrolyte have not been reported. Using the agar gel-IL composite material, which could be observed using an electron microscope, as the electrolyte, it is expected that the ionic behavior and reaction on the surface and inside of the electrolyte could be observed using in-situ TEM with a specific holder which has a super-imposed voltage ability (see Figure 7. 2).

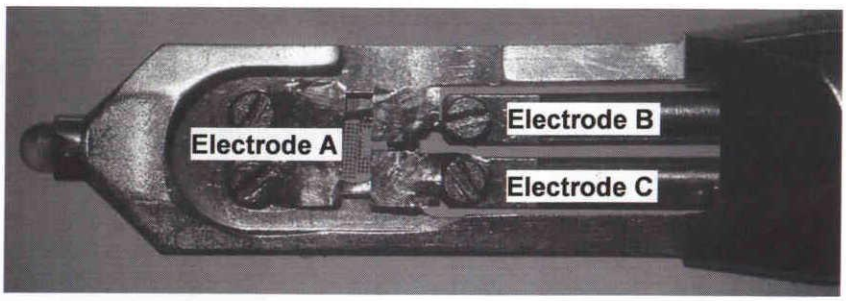

Figure. 7. 2. Designed specific holder for in-situ TEM measurement.

Accordingly, the molecular dynamics of the IL, which has never been characterized by direct visualization on a nano-scale, might be observed using this developed method.

LIST OF PUBLICATIONS

PUBLICATIONS IN JOURNALS

Chapter 2

1. **Electron microscopic observation of fine morphology of wet agar gel using a typical hydrophilic ionic liquid; 1-butyl-3-methylimidazolium tetrafluoroborate.**

   Chisato Takahashi, Takashi Shirai, Masayoshi Fuji.

   Advances in Technology of Materials Processing Journal, 13 (2011), pp. 39-47.

2. **Observation of interactions between hydrophilic ionic liquid and water on wet agar gels by FE-SEM and its mechanism.**

   Chisato Takahashi, Takashi Shirai, Masayoshi Fuji.

   Materials Chemistry and Physics, 133 (2012), pp. 565-572.

3. **FE-SEM observation, and, mechanism of interaction of wet agar gel in various swelling conditions using hydrophilic ionic liquid.**

   Chisato Takahashi, Takashi Shirai, Masayoshi Fuji.

   Materials Chemistry and Physics, 136 (2012) 816-822.

Chapter 3

4. **Application of hydrophilic ionic liquid treatment to the morphological observations of hydrated porous ceramic green bodies.**

   Chisato Takahashi, Deepak K. Pattanayak, Takashi Shirai, Masayoshi Fuji.

   Ceramics International, 39 (2013) 1065-1073.

5. **A simple approach to observe non-conductive hydrated materials with FE-SEM: case study on porous hydroxyapatite green bodies.**

   Chisato Takahashi, Deepak K. Pattanayak, Takashi Shirai, Masayoshi Fuji.

   Journal of European Ceramics Society, (2012) in press

Chapter 4

6. **FE-SEM observation of swelled seaweed using hydrophilic ionic liquid; 1-butyl-3-methylimidazolium tetrafluoroborate.**

   Chisato Takahashi, Takashi Shirai, Masayoshi Fuji.

   Microscopy Research and Technique, (2012) in press

Chapter 5

7. **Electron microscopic observation of montmorillonite swelled by water with the aid of hydrophilic ionic liquid.**

   Chisato Takahashi, Takashi Shirai, Masayoshi Fuji.

   Materials Chemistry and Physics, (2012) under review

Chapter 6

8. **Study on intercalation of ionic liquid into montmorillonite and its property evaluation.**

   Chisato Takahashi, Takashi Shirai, Masayoshi Fuji.

   Materials Chemistry and Physics, 135 (2012), pp. 681-686

9. **Study of intercalation compounds using ionic liquids into montmorillonite and their thermal stability.**

Chisato Takahashi, Takashi Shirai, Masayoshi Fuji.

Solid State Ionics, (2012) under review

NOTE: **APPLIED FOR PATENT**

CONFERENCE AND PROCEEDINGS

1. **C. Takahashi,** T. Shirai, M. Fuji, "Development of electron microscopic observation for the gel using ionic liquid", Proceeding of the 67th Annual Meeting of The Japanese Society of Microscopy (JSM 2010), Nagoya, Japan, (16-18th May 2011) pp.162. **Oral.**

2. **C. Takahashi,** T. Shirai, M. Fuji, "The electron microscopic observation for the swellheaded gel using hydrophilic imidazolium ionic liquid and its mechanism", Proceeding of the 24th Fall Meeting of The Ceramics Society of Japan, Hokkaido, Japan, (7-9th Sep 2011) pp.213. **Oral.**

3. **C. Takahashi,** T. Shirai, M. Fuji, "Development of structural evaluation method using hydrophilic ionic liquid", 24th Fall Meeting of The Ceramics Society of Japan, Hokkaido, Japan, (7-9th Sep 2011) pp.222. **Poster.**

4. **C. Takahashi,** T. Shirai, M. Fuji, "Observation of agar gel in various wet conditions with hydrophilic ionic liquid; 1-butyl-3-methylimidazolium tetrafluoroborate using electron microscope and its mechanism", International symposium on role of electron microscopy in industry, Toward genuine collaboration between academia and industry 2012, Nagoya, Japan, (19-20th Jan 2012). **Poster.**

5. **C. Takahashi,** T. Shirai, M. Fuji, "Observation of agar gel with hydrophilic ionic liquid using electron microscope and its behavior" 2012年度　セラミック

ス基盤工学研究センター研究成果報告会, Toki, Japan, (8th Mar 2012). **Poster.**

ACKNOWLEDGEMENTS

It would not have been possible to complete my doctoral thesis in this present form without the help and support of numerous people who were really kind to me. I owe to all of them. Firstly, I wish to express my utmost gratitude to my supervisor, **Professor Masayoshi Fuji** for his constant inspiration, enthusiasm and invaluable suggestions during my PhD program. Prof. Fuji gave me a great opportunity to work in his laboratory and helped me to complete my doctoral degree. I deeply felt his personal warmth and leadership which helped me to maintain the high motivation in this research work. His valuable discussions and critiques made by him were essential to my work.

I would also wish to express my thanks to **Professor Masaki Tanemura** from Nagoya Institute of Technology who support and provided the environment for continuing this work in his laboratory, **Professor Shunsuke Muto** from Nagoya University who provided valuable suggestions, encouragements and constructive comments on my work to make it more scientifically relevant and **Assistant professor Nobuyasu Adachi** from Nagoya Institute of Technology who helped me to complete doctoral thesis and gave encouragements.

My deepest appreciation goes to **Dr. Minoru Takahashi**, president of Nagoya Institute of Technology, for his kind and continuous support during this study.

I am really grateful to **Professor Hiroyasu Saka** from Nagoya University who taught me knowledge of electron microscope and gave constant support. I have investigated lots of important things under the guidance of Prof. Saka when I was in Nagoya University. I would also like to thank **Professor Nobuo Tanaka** who made enormous contribution to my PhD work. **Professor Kotaro Kuroda** from Meijo University has also been tolerant and very much supportive to me. My sincere thanks go to **Assistant professor Tomoharu Tokunaga** from Nagoya University for his valuable comments and support.

I am deeply grateful to **Associate professor Yasuhiko Hayashi** and **Assistant professor Toru Asaka** from Nagoya Institute of Technology for their constant

motivation and impression. Furthermore, I am deeply indebted to **Professor Emiko Hamada**, **Visiting professor Keiko Kondo**, **Visiting professor Katsuyoshi Naganuma** and **Ms. Seiko Ueno** from Nagoya Institute of Technology for their kind support and encouragements.

I would specially like to thank all the members of Advanced Ceramics Research Center (ACRC) for their encouragements and continuous help during my research work. **Dr. Shirai** gave me a great opportunity to work in new and advanced topic and his valuable discussions helped me to improve my work. I received generous support and encouragement from **Dr. Tatsuya Tomioka**, **Dr. Chika Takai, Dr. Tran Thi Thu Hien, Mr. Mitsuo Utsuno** and **Mr. Jyunzou Tsuchimoto** who helped to improve my work. I am also thankful to **Mrs. Shiho Yoshinaga** for her warm support for various official works and encouragement. My special thanks to **Dr. Tomoaki Kato**, **Mr. Seiji Yamashita** and **Mr. Fumikazu Kawajiri** for their help for some experiments and discussions.

I am indebted to **Dr. Deepak Kumar Pattanayak**, of Central Electrochemical Research Institute, India, for his constant supports and warm encouragements during this work. My study would not have been much improved without his efforts.

Dr. Yasushi Kaneko and **Mr. Toshiyuki Suzuki** gave insightful comments and suggestions helped to me improve my research quality.

I would like to express my gratitude to **Dr. Akihiro Matsumoto**, **Dr. Kimiyasu Sato Dr. Hiroyuki Hosokawa** and **Mr. Noriyuki Saito** from National Institute of Advanced Industrial Science and Technology (AIST) for their kind support and encouragement. Their guidance enabled me to work in the field of materials science.

I am deeply grateful to **Japan government** for providing me an excellent opportunity to carry out a successful research work at Nagoya Institute of Technology.

Finally, I would like to express my deepest gratitude and sincere thanks to my mother Kaoru Takahashi for her love and for providing me a warm environment for me. I cannot express my gratitude in word. She is always energetic and kept me cheered up during my PhD program even in hard situation. I would also like to thank my relatives and friends for being so polite for all the time and give me kind supports, cooperation and warm encouragement.

Chisato Takahashi